类号______ 密级______

UDC ______ 编号______

华中师范大学

博士学位论文

RHIC-STAR上椭球流的研究

学位申请人姓名：施梳苏

申请学位专业方向：粒子物理与原子核物理

指导教师姓名：刘峰教授 许怒教授

博士学位论文

RHIC-STAR上椭球流的研究

论文作者：施梳苏

指导教师：刘峰， 许怒

专业名称：粒子物理与原子核物理

研究方向：相对论重离子碰撞

华中师范大学物理学院

2010年5月

Dissertation

Event anisotropy v_2 at STAR

By

Shusu Shi

Supervisor: Feng Liu and Nu Xu

Specialty: Particle Physics and Nuclear Physics

Research Area: Relativistic heavy ion collisions

College of Physical Science and Technology

Central China Normal University

May 2010

华中师范大学学位论文原创性声明和使用授权说明

原创性声明

本人郑重声明： 所呈交的学位论文，是本人在导师的指导下，独立进行研究工作所取得的成果。除文中已经注明引用的内容外，本论文不含任何其他个人或集体已经发表或撰写过的作品或成果。对本文的研究做出重要贡献的个人和集体，均已在文中以明确方式标明。本声明的法律结果由本人承担。

论文作者签名：　　　　　　　　　　　　日期：　　　年　　月　　日

学位论文版权使用授权说明

本人完全了解华中师范大学关于收集、保存、使用学位论文的规定，即：学校有权保留并向国家有关部门或机构送交论文的复印件和电子版，允许论文被查阅和借阅。本人授权华中师范大学可以将本学位论文的全部或部分内容编入有关数据库进行检索，可以采用影印、缩印或扫描等复制手段保存和汇编本学位论文。

保密论文在解密后遵守此规定。

论文作者签名：　　　　　　　　　　　　导师签名：

日期：　　　年　　月　　日　　　　　　日期：　　　年　　月　　日

……………………………………………………………………………………………………

本人已经认真阅读“CALIS 高校学位论文全文数据库发布章程”，同意将本人的学位论文提交“CALIS 高校学位论文全文数据库”中全文发布，并可按“章程”中规定享受相关权益。同意论文提交后滞后：□半年；□一年；□二年发布。

论文作者签名：　　　　　　　　　　　　导师签名：

日期：　　　年　　月　　日　　　　　　日期：　　　年　　月　　日

摘要

在相对论重离子碰撞的早期，产生出了一种高温高密的强相互作用的新物质形态。随后系统的演化则由新物质的性质决定。在本篇论文中，我们通过测量重离子碰撞中产生的粒子相对于反应平面（由碰撞参量和束流所在的方向决定）的方位角各向异性来研究系统演化的动力学。在非对心碰撞中（碰撞参数不为零），参加碰撞的区域成一个椭球状，因而在空间坐标中是各向异性的。这种初始的空间坐标中的各向异性会通过相互作用而转化为末态动量空间的各向异性。本文中所讨论的椭球流，v_2, 是末态动量空间粒子方位角分布傅里叶展开式的第二项。由于初始的空间各向异性所产生的压力梯度随时间演化迅速消失（自猝灭效应），椭球流直接于碰撞早期的动力学相联系。椭球流的大小强烈依赖于碰撞过程中相互作用的强弱，因此它可以提供早期重离子碰撞中压力梯度，有效自由度，热化以及碰撞早期新物质形态状态方程的信息。进一步，学习椭圆流在不同对撞能量下对中心度和系统大小的依赖性是研究高能重离子碰撞产生的新物质形态性质的有效途径。

在这篇论文中，我们系统分析了由STAR探测器在2005年RHIC运行中所采集的质心系能量为62.4 GeV和200 GeV的铜铜碰撞数据和在2007年所采集的9.2 GeV和200 GeV金金碰撞事件。我们测量了金金200 GeV碰撞事件中奇异粒子的椭球流。借助于2007年采集的金金200 GeV大统计量数据，我们可以精确的测量到多重奇异粒子ϕ介子和Ω重子的椭球流。由于多重奇异粒子产生于高能重离子碰撞的早期，而且它们具有较小的强子强子相互作用截面，因此多重奇异粒子被认为是能够反映碰撞早期物理的探针。ϕ介子和Ω重子显著的椭球流为部分子层次的集体运动在RHIC的形成提供了强有力的证据。其中在中横动量区（$2 < p_T < 5$ GeV/c）观察到的组分夸克标度性说明夸克层次的自由度已经达到，即在强子化过程之前存在一个解禁闭的状态。我们利用STAR采集的不同系统和不同碰撞能量的数据，系统的研究了组分夸克的标度性，发现在62.4 GeV和200 GeV的金金与铜铜碰撞事件中，都能清楚的观察到这一标度性。实验结果表明，在质心系能量为62.4 GeV和200 GeV的重离子碰撞中所产生的物质达到了解禁闭状态。

我们测量了铜铜200 GeV碰撞事件中带电粒子和奇异粒子的椭球流。由于铜铜碰撞系统相比较于金金系统小的多，因此具有较小的末态多重数。在这种情况下，如

果我们用中间快度区（$|\eta| < 1.0$）所确定的反应平面测量椭球流则会包含较大的非流效应。我们首次采用了用前端快度区的粒子确定反应平面测量椭球流的方法，使得非流效应在铜铜碰撞系统中所带来的系统误差大大降低。利用相同能量下p+p 碰撞数据，我们分析了椭球流测量中的剩余非流效应。通过对带电强子以及奇异粒子（K_S^0, $\Lambda + \bar{\Lambda}$ and $\Xi^- + \bar{\Xi}^+$）在不同对心度的椭球流测量并于金金碰撞中的数据相比较,我们研究了椭球流对碰撞系统和对心度的依赖性。我们发现奇异粒子的椭球流相对于横动量的依赖性与金金碰撞中所表现出来的标度性十分相似：（i）在低横动量区，$p_T < 2$ GeV/c, 椭球流具有横能量，$m_T - m$，的标度性；（ii）在中横动量区，$2 < p_T < 4$ GeV/c, 椭球流具有组分夸克的标度性。碰撞系统的初始条件可以由碰撞区域的偏心率（ε）来表示，我们发现不同对心度的椭球流除以其对应的初始几何条件之后，在越接近对心的碰撞中可观察到较大的椭球流，这表明集体运动的强弱依赖于对心度。通过对不同对心度及不同碰撞系统的比较，我们发现椭球流的强弱依赖于一个共同的量，参加反应的核子数（N_{part}）。在理想流体力学极限下，由于系统充分热化，椭球流由初始几何形状完全决定。因此这一实验结果表明理想流体极限在铜铜碰撞中没有达到，可能是因为完全热化这一假设并不成立。

由于理想流体力学的基本假设是系统完全热化，因此比较椭球流的实验结果与理想流体的计算结果有助于我们研究RHIC能量下重离子碰撞早期所形成的物质是否完全热化。我们的研究表明，理想流体力学的椭球流对横动量的依赖性的计算结果在不同对心度中与实验结果不吻合。迄今为止，用于理想流体计算的模型仍有一些因素没有考虑，诸如初始几何形状的逐事件涨落（这一效应尤其对中心碰撞的结果影响较大），有限的粘滞系数等。因此，进一步的理论研究需要考量这些因素是否导致了我们所观察到的实验数据与理论计算的不一致。

利用输运模型，我们分析了v_2/ε对末态粒子密度的$1/S\ dN/dy$依赖性。我们的结果表明，在接近中心的金金200 GeV碰撞中，系统只达到了$0.46^{+0.24}_{-0.07}$ 或者$0.75^{+0.14}_{-0.10}$ 理想流体力学极限，不同的计算结果分别基于确定碰撞初始条件的模型Glauber与CGC。进一步，通过输运模型所提取的Knudsen参数使得我们可以估算有效的部分子散射截面以及剪切粘滞系数相对于熵密度的比值。

在2008年的测试运行中，STAR探测器成功的采集了三千个金金9.2 GeV碰撞事件。利用这些事件，我们测量了带电强子，π介子和p重子的椭球流。我们的结果与相同碰撞能量相似碰撞系统NA49实验组的发表结果吻合。这表明，STAR探测器在较低

能量下运行良好，具有进行束流能量扫描的能力。在即将进行的RHIC能量扫描的运行计划中，通过对椭球流组分夸克标度性的碰撞能量依赖性的研究，我们可以确定形成解禁闭物质系统的碰撞能量，这对寻找QCD预言的临界点和相边界有重要的意义。

关键词: 相对论重离子碰撞 集体运动 椭圆流 奇异粒子 组分夸克标度性 热化 粘滞系数

Abstract

At the early stages of relativistic heavy ion collisions, a hot and dense, strongly interacting medium is created. The subsequent system evolution is determined by the nature of the medium. Experimentally, the dynamics of the system evolution has been studied by measuring the azimuthal anisotropy of the particle production relative to the reaction plane. The centrality of the collision, defined by the transverse distance between the centers of the colliding nuclei called the impact parameter, results in an "almond-shaped" overlap region that is spatially azimuthal anisotropic. It is generally assumed that the initial spatial anisotropy in the system is converted into momentum-space anisotropy through re-scatterings. The elliptic flow, v_2, is the second harmonic coefficient of a Fourier expansion of the final momentum-space azimuthal anisotropy. Due to the self-quenching effect, it provides information about the dynamics at the early stage of the collisions. Elliptic flow can provide information about the pressure gradients, the effective degrees of freedom, the degree of thermalization, and equation of state of the matter created at the early stage. Thus, the centrality and system-size dependence of elliptic flow at different beam energies can be used to study the properties of the matter created in heavy ion collisions.

In this thesis, we analyze the data collected with the STAR detector from $\sqrt{s_{NN}} =$ 62.4 and 200 GeV Cu+Cu collisions during the fifth RHIC run in 2005 and $\sqrt{s_{NN}} = 9.2$ and 200 GeV Au+Au collisions during the seventh run in 2007. We present results on elliptic flow v_2 of identified particles in Au+Au collisions at $\sqrt{s_{NN}} = 200$ GeV. With the large statistics of the RHIC seventh run in 2007, we measured multi-strange hadrons, ϕ and Ω v_2 in high precision. We find they flow almost as strong as pion and proton. As multi-strange hadrons are created at the early stage of the collisions, and they are less sensitive to the late hadronic process with their smaller hadronic cross section, thus, the significant v_2 of multi-strange hadrons indicates the partonic collectivity has been built up in the heavy ion collisions at RHIC. The Number of Quark (NQ) scaling reflects constituent quark is the most effect degree of freedom in determining hadron flow at intermediate p_T. This suggests that the system has been in the deconfined state prior

to hadronization. We systematically discuss the NQ scaling at RHIC and find it holds in the intermediate p_T region, $2 < p_T < 5$ GeV/c, for all systems (Au+Au and Cu+Cu) and beam energies (62.4 GeV and 200 GeV). It suggests the deconfinement has been reached at RHIC.

We present the results of an elliptic flow analysis of Cu+Cu collisions at $\sqrt{s_{NN}} = 62.4$ and 200 GeV. Elliptic flow as a function of transverse momentum, $v_2(p_T)$, is reported for different collision centralities for charged hadrons $h^{\pm}$, and strangeness containing hadrons K_S^0, $\Lambda + \bar{\Lambda}$ and $\Xi^- + \overline{\Xi}^+$ in the midrapidity region $|\eta| < 1.0$. Significant reduction in systematic uncertainty of the measurement due to non-flow effects has been achieved by correlating particles at midrapidity, $|\eta| < 1.0$, with those at forward rapidity, $2.5 < |\eta| < 4.0$. We also present azimuthal correlations in p+p collisions at $\sqrt{s} =$ 200 GeV to help estimating non-flow effects. To study the system-size dependence of elliptic flow, we present a detailed comparison with the results from Au+Au collisions at $\sqrt{s_{NN}} =$ 200 GeV. We observe that $v_2(p_T)$ of strange hadrons has similar scaling properties as were first observed in Au+Au collisions, i.e.: (i) at low transverse momenta, $p_T < 2$ GeV/c, v_2 scales with transverse kinetic energy, $m_T - m$, and (ii) at intermediate p_T, $2 < p_T < 4$ GeV/c, it scales with the number of constituent quarks, n_q. Eccentricity scaled v_2 values, v_2/ε, are larger in more central collisions, suggesting stronger collective flow develops in more central collisions. The comparison with Au+Au collisions which go further in density shows v_2/ε depend on the system size, number of participants N_{part}. This indicates that the ideal hydrodynamic limit is not reached in Cu+Cu collisions, presumably because the assumption of thermalization is not attained.

The comparison of the data to the ideal hydrodynamic calculations may shed light on the thermalization issue at RHIC. We find that ideal hydrodynamic calculations fail to reproduce the centrality dependence of $v_2(p_T)$ in both Au+Au and Cu+Cu collisions at $\sqrt{s_{NN}} =$ 200 GeV collisions. To date, there are serval effects not included in the model, such as geometrical fluctuations in the initial conditions (particularly important in central collisions), finite viscosity effects. It remains to be seen if these effects can account for the difference between the models and data.

With a transport model, we study the $1/S\ dN/dy$ dependence of v_2/ε. The extracted

Knudsen numbers show finite values, even for central collisions. It indicates that the system has reached $0.46^{+0.24}_{-0.07}$ and $0.75^{+0.14}_{-0.10}$ of ideal hydrodynamic limits, using Glauber and Color Glass Condensate (CGC) initial condition, respectively. The lack of perfect equilibration allows for estimates of the effective parton cross section in the quark-gluon plasma and of the shear viscosity to entropy density.

With 3 k events collected using STAR detector from a test run of the collider in the year 2008, we present the results of an elliptic flow analysis of Au+Au collisions at $\sqrt{s_{NN}}$ = 9.2 GeV. Our results are consistent with the corresponding previous results from NA49 at similar $\sqrt{s_{NN}}$. It demonstrates the capabilities of the STAR detector to pursue the proposed beam energy scan. The beam energy dependence of NQ scaling in v_2 should be a powerful tool for searching for the possible QCD phase boundary.

Table of Contents

List of Figures

List of Tables

CHAPTER 1

Introduction

1.1 Quantum ChromoDynamics

1.1.1 Confinement and Asymptotic Freedom

Quantum ChromoDynamics [Dks03a], QCD, is regarded as a right theory for the strong nuclear force, one of the four fundamental forces of nature (the strong force, the electromagnetic force, the weak force and the gravity force). The strong interactions among quarks, which are thought to be fundamental constituents of matter via their color quantum numbers, can be described by QCD. In the QCD theory, a set of force particles called gluons mediate the strong interactions among quarks. It is quiet different from Quantum ElectroDynamics (QED): the electromagnetic interaction is described by the gauge theory, where QCD is based on the non-Abelian gauge group $SU(3)$ with gauge bosons (color octet gluons). Therefore the gluons could have self-interacting. This results in a negative β function and asymptotic freedom at high energy and strong interactions at low energy.

Because the self-coupled gluons restrain the isolation of the quarks strongly at large distance, these strong interactions are confining. To date, no single quark as a color-triplet state is observed in experiment. Based on the QCD theory, only color-singlet bound state propagates over macroscopic distances. The known color-singlets with the size of order of 1 fm are two-quark pairs, mesons, and three-quark states, baryons. In reactions with high energy, for example, deep inelastic scattering, the quarks and gluons in the hadron act as quasi-free particles which are usually called partons. Such reactions can be factorized into the convolution of non-perturbative parton distribution

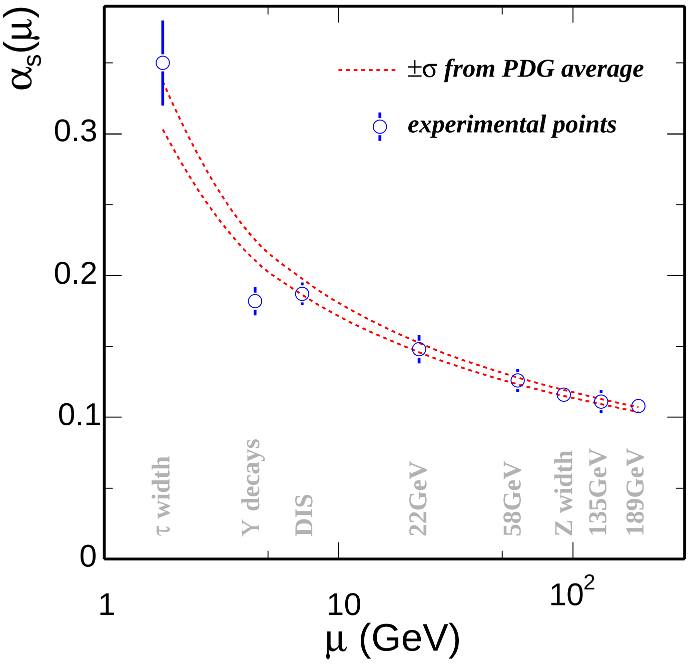

Figure 1.1: Lattice QCD calculations compared with coupling constant α_s from experiments.

functions, but it can not be directly calculated from first principles. With process-dependent functions i.e. hard processes involving large momentum transfers, one can calculate the reactions by perturbative expansions in the coupling constant α_s.

The electrodynamic coupling constant α is equal to $\frac{1}{137}$ in QED. However, the renormalized QCD coupling shows the dependence of renormalization scale (μ) [Bet02a], because of the gluons self-interactions. The running coupling $\alpha_s(\mu)$ can be written as:

$$\alpha_s(\mu) \equiv \frac{g_s^2(\mu)}{4\pi} \approx \frac{4\pi}{\beta_0 \ln(\mu^2/\Lambda^2_{\mathrm{QCD}})}, \tag{1.1}$$

Here g_s is the strong charge in the gauge group. Besides the quark masses $g_s$is the only parameter in the QCD Lagrangia. β_0 (>0) is the first coefficient of the β-function (renormalization neglects the higher orders). At shorter distance or with larger momentum transfers ($\alpha_s \rightarrow 0$ as $\mu \rightarrow \infty$) the strong force of the gluon-gluon self-coupling becomes smaller, which is known as asymptotic freedom. In this case, QCD can be calculated perturbatively. Many experiments measured α_s at different scales. Since some of the precise measurements come from Z^0 decays, it has become universal to use $\alpha_s(M_z)$ as the label. The $\alpha_s(M_Z) = 0.1176 \pm 0.002$ [Pdg08a] comes from a fit to the experimental data, and the QCD scale $\Lambda_{QCD} \sim 200$ MeV. Fig. 1.1 shows lattice QCD calculations compared with coupling constant α_s from experiments..

1.1.2 Deconfinement

Quarks are regarded as point-like. and by Because of the binding potential $V_0(r)$, which increases with the quark separation r,

$$V_0(r) \sim \sigma r \tag{1.2}$$

they are confined in the hadron. Here σ (string tension) is the energy per unit separation distance. In order to isolate a quark ,Infinite amount of energy are needed. Thus, splitting a hadron into isolated quarks is impossible. The definition of deconfined quarks is that they can move in a volume much larger than the volume of a nucleon (a hadron). To date, deconfined quarks have never been seen in normal temperature and density.

In QCD theory, the interaction between quarks depends on the intrinsic color charges. The color charges exhibit a long-range feature - confinement. At the same time, the color charges can be screened in the same way as electric charges in an extreme high density of color charges, which is known as Debye screening: the long-range interaction is shortened in dense medium of charges. The potential with color screening [Sat00a] is given by

$$V(r) \sim \sigma r \left[\frac{1 - exp(-\mu r)}{\mu r}\right] \tag{1.3}$$

at high density, here μ is the color screening mass.

Figure 1.2 shows the potential as a function of distance r. The potential increases linearly with r, when μ is equal to 0; while the potential remains a finite constant as r increases, when μ is not equal to 0. Long range effects are removed by the damping of the binding force. As color screening occurs at adequately high density, we could imagine a picture as following: hadrons which are made up of point-like quarks start to overlap, thus each quark is surrounded by a large number of quarks in the vicinity of the volume size (the intrinsic spatial extension of nucleons). It is impossible to identify which quarks are the original constituents of a specific nucleon at previous state of low density. Out of a certain point, it is meaningless for the concept of a hadron. Thus in the case of color screening, it will be short-range of the interactions between the quarks

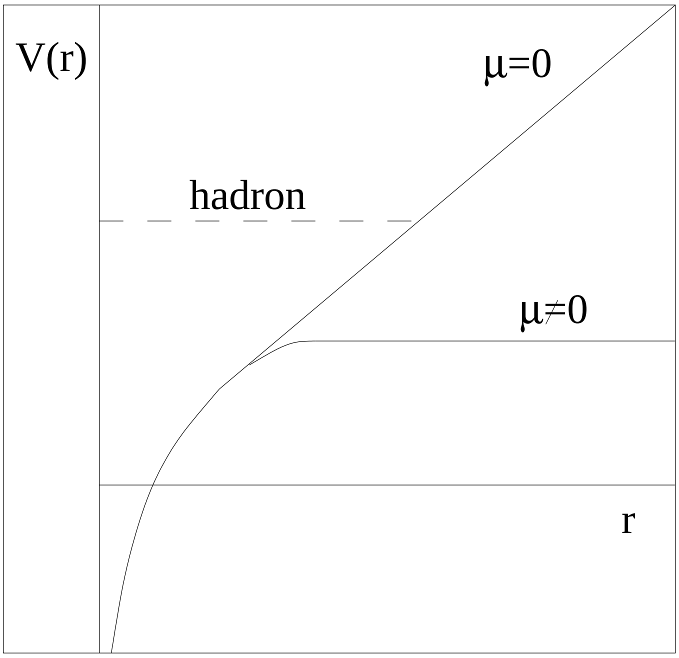

Figure 1.2: Color screening of the confining potential. All calculations are from [Sat00a].

and gluons. The hadron matter is converted to the Quark Gluon Plasma as the color insulator is converted to the color conductor[Sat00a].

The results of lattice QCD suggest that quarks will be deconfined if the temperature is sufficient high. A rapid increase in entropy density can reflect the existence of color degrees of freedom. In fig. 1.3, it shows that the ratio of the pressure over T^4 rises sharply when the temperature is greater than the critical temperature $T_c \sim 160$ MeV. The transition from the hadronic phase to the QGP phase could be reflected by the rapidly increase. In the QGP phase, quarks and gluons degrees of freedom have been built up. The arrows in fig. 1.3 represent the Stefan-Boltzman limits (in this case, the deconfined quarks and gluons are non-interacting and massless). A significant deviation from the SB limit can be observed, which suggests there are some remaining interactions among the quarks and gluons in the QGP phase.

1.2 Relativistic Heavy Ion Collisions

The main goal of building the Relativistic Heavy Ion Collider (RHIC) is to create bulk matter of deconfined quarks and gluons (Quark Gluon Plasma) and study its properties in

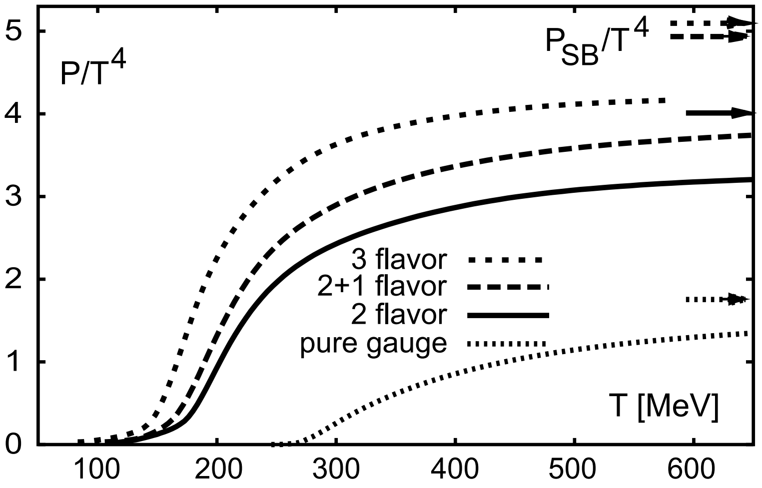

Figure 1.3: P/T^4 (Pressure over T^4) as a function of T based on LQCD calculation for several different number of quark flavors. The arrows represent the corresponding Stefan-Boltzmann pressure. All LQCD calculations are from [Kar02a].

extreme high temperature and density. The new form of matter created in the laboratory is believed to exist at very early stage of universe evolution. Studying QGP formation will help us to understand the fundamental structure of the matter and evolution of our universe.

1.2.1 Collision Geometry

In relativistic heavy ion collisions, the geometry of the collisions can be defined by the participant spectator model. Figure 1.4 shows a schematic view of heavy ion collision between symmetric Lorentz contracted projectile and target nuclei in the center of mass frame. The impact parameter b is the distance between the center of nuclei and characterize the centrality of collision. The nucleons taking part in the primary collisions are called as participants and the rest that are not participated in the collisions are called as spectators. In most heavy ion experiments, the impact parameter is estimated by measuring the size of the participants and/or the spectators. The participants and the spectators are well separated experimentally because the spectator keeps it longitudinal velocity and mostly emitted in the forward (backward) rapidity, while the secondary particles from participants are peaked around mid-rapidity. Once the impact parameter

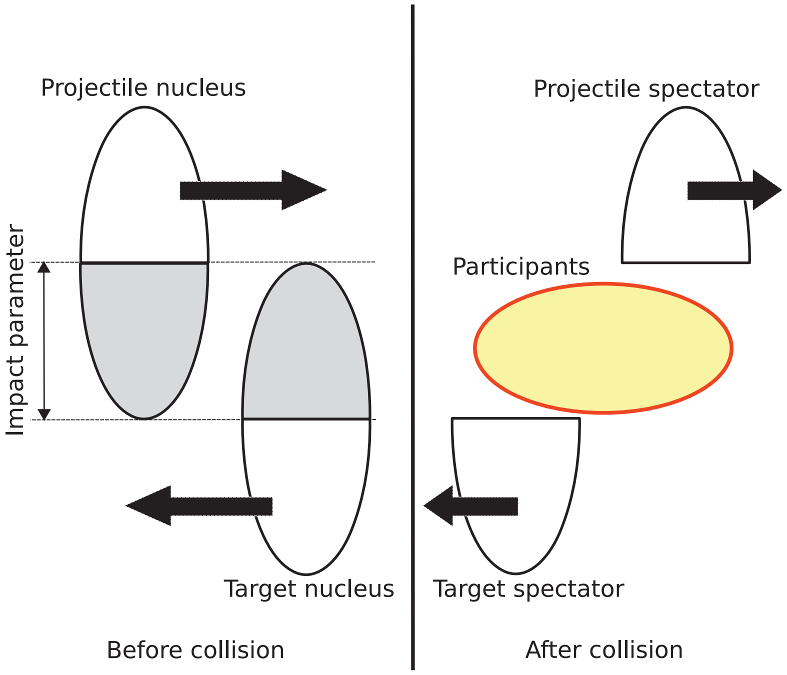

Figure 1.4: A schematic view of the geometry for a heavy ion collisions.

of the collision is determined, the Glauber Model [Mil07b] provides the number of participant nucleons (N_{part}), number of nucleon-nucleon collisions (N_{coll}), and the spatial eccentricity (ε) for a given impact parameter. These quantities can be calculated analytically or numerically under the following assumptions: a) Collisions of two nuclei are expressed in terms of the individual interactions of the constituent nucleons. b) At high energies, nucleons travels on straight line trajectories and are essentially undeflected. c) Inelastic nucleon-nucleon cross-section is independent of the number of collisions for a nucleon underwent before.

What is the relation between these quantities and the experimental observables? N_{part} is scaled with the volume of the interaction region, i.e., $N_{\text{part}} \propto A$, where A is the mass number of nucleus, it is often assumed that the multiplicity dN/dy is proportional to N_{part}: $dN/dy \propto N_{\text{part}} \propto A$. This relation can be obtained from the ideal hydrodynamics with (1+1)-dimensional expansion.

For processes involving large momentum transfer (hard scattering processes), all nucleon-nucleon collisions are assumed to be independent because of their small cross sections. Therefore, the cross-sections for hard-scattering processes should scale with the number of binary nucleon-nucleon collisions.

Perfect liquid hydrodynamics suggest that initial anisotropy in the coordinate space are directly converted into the momentum anisotropy in the final momentum space. Since hydrodynamic model always assumes the local thermal equilibrium, the relation between initial spatial eccentricity and the final momentum anisotropy could provide the signal of possible thermalization in the early stage of heavy ion collisions.

1.2.2 Time Evolution

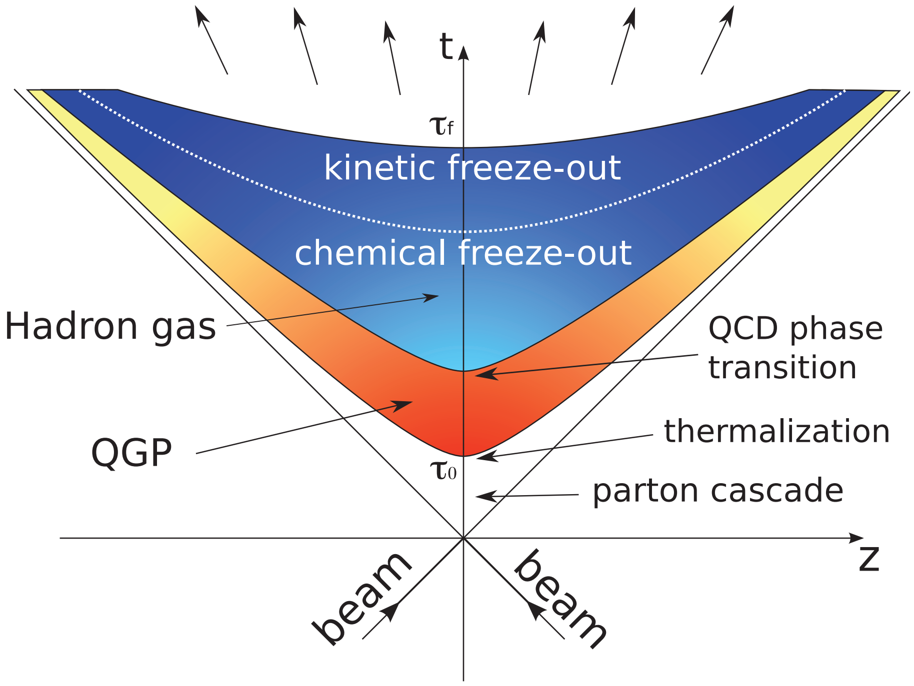

Figure 1.5: Space-time Evolution of a Heavy Ion Collision.

Fig. 1.4 shows a simplified space-time evolution of a heavy ion collision which consists of 4 stages; (i) a parton cascade stage, (ii) a QGP phase, (iii) an interacting hadron gas phase and (iv) a free hadron stage.

Parton cascade stage: $0 < \tau < \tau_0$

Several models are proposed to describe the dynamics of initial parton-parton scattering in heavy ion collisions: the color-string models [Mat87a], color glass condensate [Mcl01a], and perturbative QCD models [Wan97a]. The parton production mechanism in parton cascade stage, however, is not well understood, and it is being actively studied both from theoretical and experimental point of view.

QGP phase and QCD phase transition: $\tau_0 < \tau < \tau_f$

The frequent scatterings of the partons leads to the local thermal equilibrim at τ_0. Once the local thermal equilibrium is attained, the relativistic hydrodynamics can be used to describe the evolution of the system. The hydrodynamic equation of motions [Kol03a] are given by:

$$\partial_\mu T^{\mu\nu} = 0, T^{\mu\nu}(x) = u^\mu u^\nu(\epsilon + P) - g^{\mu\nu} P \tag{1.4}$$

$$\partial_\mu j_i^\mu = 0, j_i^\mu(x) = n_i u^\mu \tag{1.5}$$

where ϵ, P and n_i are the proper energy density, pressure and density of charge i in local rest frame, and u_μ is the four velocity. $T^{\mu\nu}$ is the energy-momentum tensor, j^μ is the charge current density. The equation of motion is derived from the local conservation of energy and momentum $\partial_\mu T^{\mu\nu} = 0$ and local charge conservation $\partial_\mu j^\mu = 0$.

The essential assumption is the thermal and chemical equilibrium (locally) reached in the applied system. For heavy-ion collisions, due to the dense nature, the interactions between the constituents (partons or hadrons) should be strong and frequent. If the time of the interactions is long enough, the system will reach (local) equilibrium. The initial condition is prior to the reach of (local) equilibrium. At the late hadronic stage of system evolution, the interaction rates are small and can not sustain the (local) thermal equilibrium. So the hydrodynamics is only applicable in the middle possible QGP phase. The initial condition and hadronization need be modelled for a complete description of a collision. A sharp hadroniztion is modelled by the Cooper-Frye formula [Coo74a], which calculates the momentum distribution for hadrons created from the fluid elements on the freeze-out hyper-surface. Once modeling the hadronization is done, one can take advantage of the time evolution of hydrodynamics backward to estimate the initial conditions.

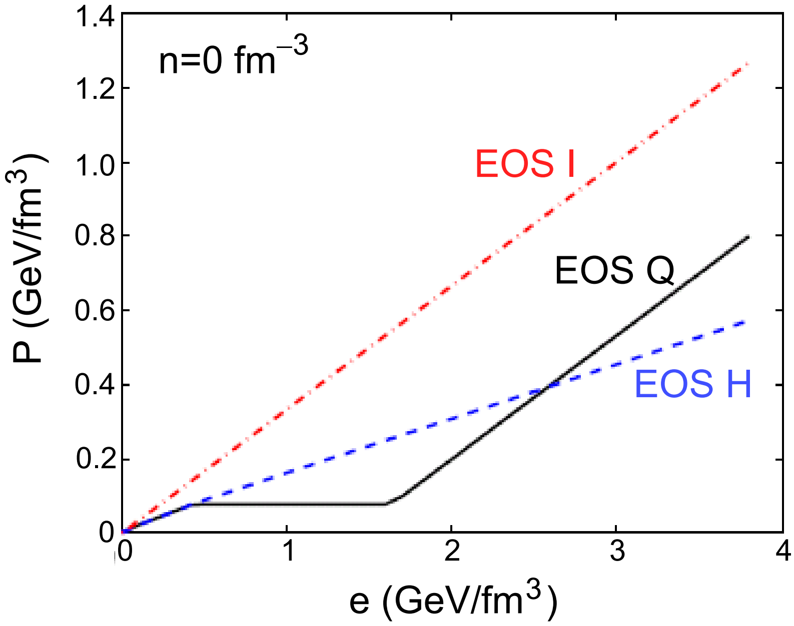

Figure 1.6: Pressure as a function of energy density at vanishing net baryon density for Equation-of-State of a Hagedorn resonance gas (EOS H), an ideal gas of massless partons (EOS I) and a connection of the two via a first-order transition at $T_c = 164$ MeV (EOS Q) [Kol03a].

With the equation of motion, the equation-of-state (EOS) need be modelled for calculation of the thermodynamic quantities of the system. Figure 1.6 shows the Equation of State from LQCD results. These EOS are used in hydrodynamic calculation in [Kol03a]. One example of EOS for a heavy ion collision is shown in solid line (EOS Q) connecting an ideal gas of massless partons at high temperature to a Hagdorn hadron resonance gas at low temperature via a first-order phase transition.

Freeze-out and free hadrons stage: $\tau_f < \tau$

The plasma expansion lead the drop of temperature, eventually hadronization takes place and relative number of species of the emitted particles is fixed at chemical freezeout temperature. The particles are rescattering each other until the hadronic interactions no longer occurred. Kinetic freeze-out happens if the kinetic equilibrium is no longer maintained, and no further hadronic interactions occur until the free streaming particles are detected. Only the hadrons from the free hadrons stage can be detected in the heavy ion experiments. It is very challenging to probe the early stage of the heavy ion collisions with hadrons measured in the finalstage.

1.3 Experimental Observations

Firstly, it is important to define what is QGP in experimental aspect. QGP is regarded as a locally thermalized state of matter. In this new state of matter, quarks and gluons are deconfined, so that patonic degrees of freedom become dominant over the nuclear, rather than merely nucleonic , volumes [Ada05a]. To claim the formation of QGP, The thermalization and deconfinement are two important features. In this section, we introduce some experimental observables at RHIC.

1.3.1 Hard Probe: Jet Quenching

The bulk medium is produced by the dynamical processes, at the same time, energetic particles are also produced by hard scattering processes. A penetrating probe is provided by the interactions of these energetic particles with the medium. The hard partons, namely, jets, will interact with the medium and thus go through energy lose. The gluon density of the medium could be reflected by the amount of the energy loss. The suppression of high p_T hadrons in the final state compared to that of no medium effects, for example, $p+p$ collisions, can be explained by fragmentation of the softened partons into hadrons. This is so-called jet quenching effect[Wan92a, Wan98a, Wan05a].

When $p_T > 5$ GeV/c, the perturbative QCD hard-scattering processes can explain the observed hadron spectra in Au+Au collisions at RHIC exhibiting the power-law falloff in cross section with increasing p_T [Adl02a]. The nuclear modification factor, $R_{\mathrm{A}B}$, is usually defined by

$$R_{AB}(p_T) = \frac{d^2N^{AA}/dp_Td\eta}{T_{AB}d^2\sigma^{pp}/dp_Td\eta} \tag{1.6}$$

here $d^2\sigma^{pp}/dp_Td\eta$ represents the measured differential cross section in $p+p$ inelastic collisions, $d^2N^{AA}/dp_Td\eta$ is the differential yield in $A+B$ collisions. In order to compare collisions in different systems, $T_{AB} = \langle N_{\mathrm{bin}}\rangle/\sigma^{pp}_{\mathrm{inelastic}}$ is introduced to take the nuclear geometry in consideration, where $\langle N_{\mathrm{Bin}}\rangle$ is the average number of binary nucleon-nucleon collisions. One can quickly conclude: in the case of A + B collision is only a simple superposition of $p+p$ collisions, R_{AB} should be equal to 1.

In the left panel of Fig. 1.7, it shows R_{AB} as a function of p_T in Au+Au and d+Au collisions. When $p_T > 5$GeV/c, hadron yields are almost suppressed 5 times if we compare to naive binary scaling expectations in central Au+Au collisions. While we don't observe any suppression in d+Au collisions. This suggests that the suppression can not be simply explained by the nuclear effects, i.e., nuclear shadowing of parton distribution functions and initial state multiple scattering. Further, the energy lose is suppose to depend on the length of the traveling path of partons . The medium can be penetrated by the partons which are near the surface, but the back-to-back produced partons will go through a significant length in the hot and dense medium and loose most of their energies into the medium, hence, they can not be observed. In the right panel of Fig. 1.7, the azimuthal distribution of hadrons with p_T is greater than 2 GeV/c relative to a trigger hadron with p_T^{trig} is greater than 4 GeV/c are shown. A pair of hadrons generated from a single jet will cause the near-side correlation, namely, $\Delta\phi \approx 0$, which can be observed in $p+p$, d+Au and Au+Au collisions. A pair of hadrons generated

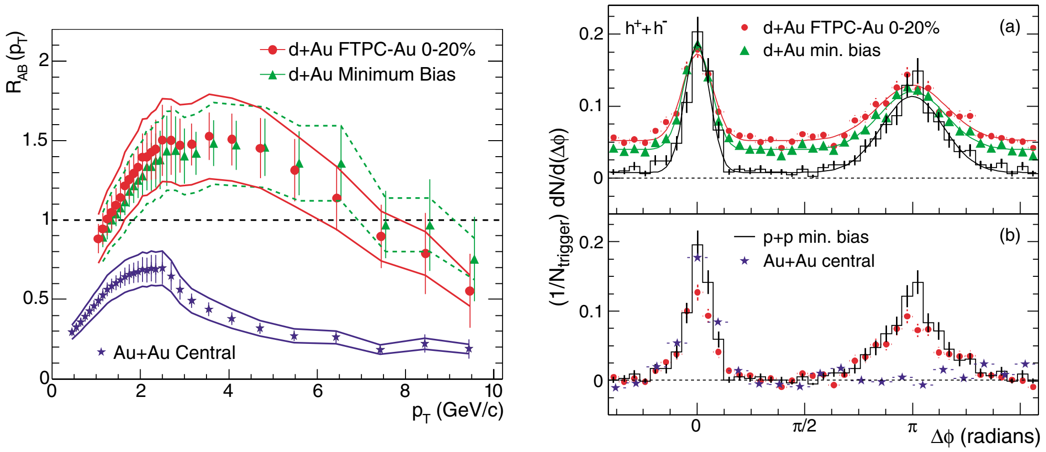

Figure 1.7: Left Panel: $R_{AB}(p_T)$ for minimum bias and $0-20\%$ most central d+Au collisions, and central Au+Au collisions. For clarity, the minimum bias d+Au collisions data are shifted 100 MeV/c to the right. The normalization uncertainties are shown by the bands. The right Panel: (a) Two-particle azimuthal distributions corrected by the efficiency in minimum bias and $0-20\%$ most central d+Au collisions, and p+p collisions. (b) A comparison of two-particle azimuthal distributions in $0-20\%$ most central d+Au collisions to those in p+p and Au+Au collisions. The respective backgrounds have been subtracted. The figure is from [Ada03b]

from back-to-back di-jets will cause the away-side correlation, $\Delta\phi \approx \pi$, which can be observed both in p+p and d+Au collisions. In most central Au+Au collisions, one can observe the significant disappearance of back-to-back correlation. These important results strongly indicate that the hot and dense medium has been built-up in heavy ion collisions at RHIC.

1.3.2 Bulk Properties

By studying the multiplicity, hadron yield, momentum spectra, etc., especially in the low p_T region, where most of final hadrons are produced, we can learn the properties of bulk matter created in collisions. Because of the dynamical origin (evolution) of the bulk-like matter, the information of the degree of thermalization and Equation of State (EoS) related to the hot and dense matter, QGP, formation are expected to be extracted.

1.3.2.1 Chemical Freeze-out

As the inelastic rescatterings stop at chemical freeze-out in relativistic heavy ion collisions, thus the content of the hadronic elements do not change since then. One can get the information for the properties of the bulk matter created in the heavy ion collisions (actually at the time of chemical freeze-out) by measuring the particle yields of different hadron species.

In the thermal model[Bra03a, Hwa03a, Hua88a], it usually assumes equilibrium on chemistry and thermodynamics. Thus, it is possible to extract some chemical freeze-out information such as chemical freeze-out temperature (T_{ch}), baryon chemical potential (μ_B) and strangeness suppression factor (γ_s) and so on by the model.

The ratios of p_T integrated particle yield for different particle species in the most central Au+Au events at $\sqrt{s_{NN}} = 200$ GeV measured by the STAR experiment are shown in fig. 1.8. The horizontal lines represent the fitting results of thermal model to the data. The fits of thermal model works well for stable and long-lived hadrons, such as π, K and p, through strange and multi-strange baryons, Λ, Ξ and Ω. But the significant deviations can be observed for the short-lived resonance yields, such as Λ^* and

K^*. This is possibly due to the hadronic re-scatterings after chemical freeze-out. Based on the fit, the extracted chemical freeze-out temperature (T_{ch}) is 163 ± 4 MeV, and the baryon chemical potential (μ_B) is 24 ± 4 MeV. The strangeness suppression factor, γ_s [Xu02a], as a function of number of participants are shown in the inset in Fig. 1.8. The deviation from chemical equilibrium can be reflected by the quantity, γ_s. As we can see, γ_s increases from 0.75 in peripheral collisions, then saturates to 0.99 in central collisions. γ_s is around unity in central Au+Au collisions. It suggests that the chemical equilibrium has been reached in central Au+Au collisions at $\sqrt{s_{NN}} = 200$ GeV.

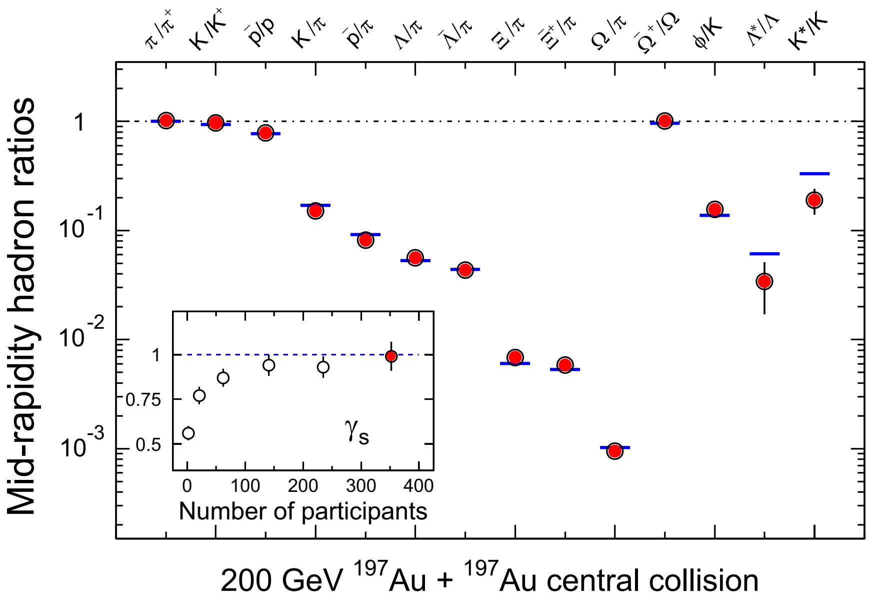

Figure 1.8: The ratios of p_T-integrated yields for several kinds of hadron at mid-rapidity in central Au+Au collisions at $\sqrt{s_{NN}} = 200$ GeV. All results are measured by STAR experiment. The results of thermal model fits to the measured yield ratios are shown by the horizontal lines. The resulting fit parameters are: $T_{ch} = 163 \pm 4$ MeV, $\mu_B = 24 \pm 4$ MeV, $\gamma_s = 0.99 \pm 0.07$ [Bar04a]. In the inset panel, it shows the value of γ_s as a function of number of participants (N_{part}). For comparison, the result from p+p collisions at $\sqrt{s_{NN}} = 200$ GeV (leftmost point) are also shown.

1.3.2.2 Kinetic Freeze-out

There are still some elastic collisions after chemical freeze-out. The constituents cease the interactions until that the system reaches the kinetic (thermal) freeze-out. The information on the characteristics of the system at kinetic freeze-out could be provided by the measurements of hadron spectra as a function of transverse momentum (p_T). We usually use the fit motivated by hydrodynamics [Sch93a] to the spectra for characterizing the transverse expansion of the system. The random motion and the collective motion components, which is respectively described by the fit parameter $T_{\rm fo}$ and $\langle\beta_T\rangle$, can be extracted by the fit. Where $T_{\rm fo}$ stands for kinetic freeze-out temperature and $\langle\beta_T\rangle$ stands for radial flow collective velocity.

In fig. 1.9, it shows the centrality dependence of kinetic freeze-out temperature and radial flow collective velocity. All results are from STAR experiment. As the events become more and more central, one can observe the value of $T_{\rm fo}$ is getting smaller and smaller, while the value of $\langle\beta_T\rangle$ is getting lager and larger for pion, kaon and proton. It suggests that the system freeze out at the relatively lower temperature in more central events, while the stronger collective flow is developed in the more peripheral collisions. For comparison, the results from $p+p$ collisions are also shown. The kinetic freeze-out temperature is almost consistent with that in the most Au+Au peripheral collisions, but the radial flow collective velocity is smaller. The multi-strange particles, ϕ and Ω, show a higher freeze-out temperature and smaller radial flow velocity than those of pion, kaon and proton, in the most central collisions. The fact that their kinetic freeze-out temperature is similar to the chemical freeze-out temperature suggests ϕ and Ω are less sensitive to the late hadronic interactions after chemical freeze-out [Ada04a, Bar04a, Bra95a, Bra99a, Bas99b]. Based on this interpretation, the radial flow velocity of ϕ and Ω should be built up prior to the chemical freeze-out, thus, they are believed to be particularly sensitive to the early partonic stage of the system create in the heavy ion collisions.

1.3.2.3 Collective Flow and Thermalization

As we discussed above, the transverse momentum spectra of different particle species reflects the components of random and collective motion. The extracted kinetic freeze-out temperature of the system connects to the random motion component. The pressure

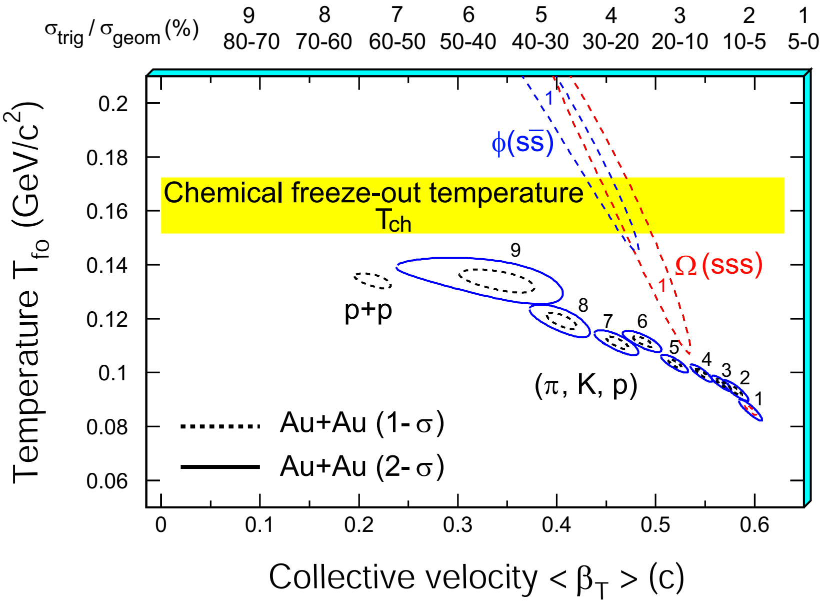

Figure 1.9: The contour plots of χ^2 for the kinetic freeze out temperature (T_{fo}) and the radical flow velocity ($\langle\beta_T\rangle$) extracted from thermal + radial flow fits to pion, kaon, proton in nine centrality bins in Au+Au collisions at $\sqrt{s_{NN}}$ = 200 GeV and p+p collisions at the same beam energy. From top to bottom, it is 70%-80% to 5% most central Au+Au collisions, respectively. The results of multi-strange hadron, ϕ and Ω, are shown only for the most central Au+Au events. 1σ and 2σ contours are represented by the dashed and solid curves, respectively. The figure is from [Ada05a].

(density) gradient from the overlapping region of two nuclei in the collisions is the origin of the collective motion component in mid-rapidity. The frequent interactions between constituents push the created matter outwards, a common velocity is built up in this process. As the collective flow depends on the strength of interactions, it can be directly connected to the pressure gradient, degree of freedom, equation of state and degree of thermalization. The common velocity of all produced particles defines the collectivity.

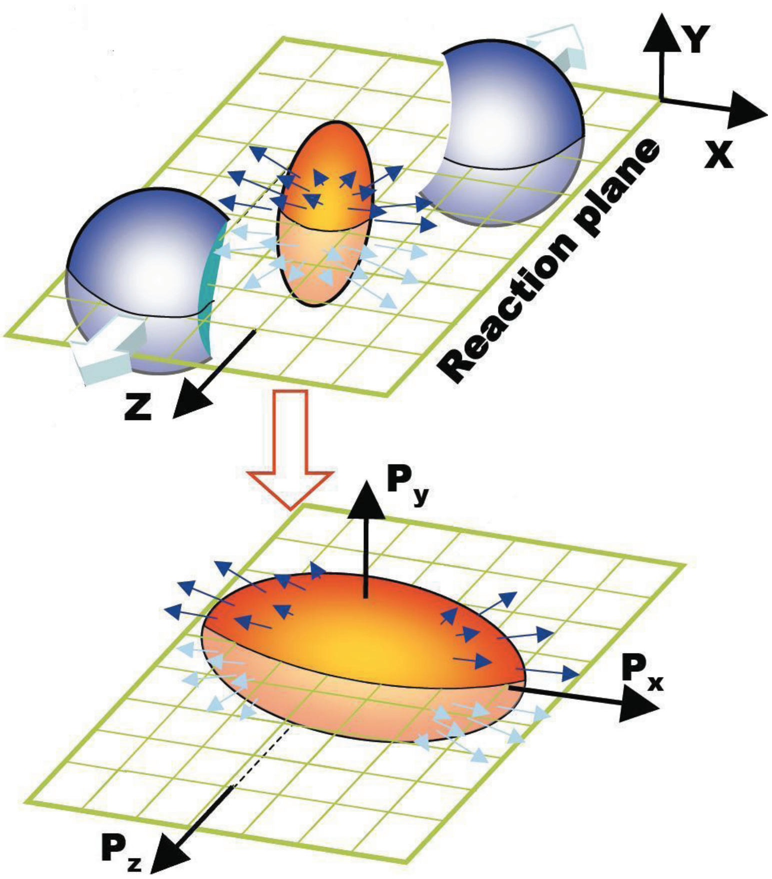

Figure 1.10: Event anisotropy in spatial and momentum space with respect to the reaction plane determined from the x (impact parameter) and z (beam) directions.

The collision geometry is shown in Fig. 1.10. In non-central collisions, the overlap area of two nuclei in the transverse plane has a short axis, which is parallel to the impact parameter, and a long axis perpendicular to it. The reaction plane is defined by the impact parameter (x) and beam (z) directions. We usually study the azimuthal anisotropy of in the momentum space with respect to the reaction plane. Since the initial anisotropy in the spatial space has an almond shape with respect to the reaction plane, this almond shape of the initial profile is converted by the pressure gradient into a final anisotropy in the momentum space.

$$\frac{\partial\rho}{\partial x} \sim \Delta p_x$$

$$\frac{\partial\rho}{\partial y} \sim \Delta p_y$$

$$\langle p_x \rangle > \langle p_y \rangle$$

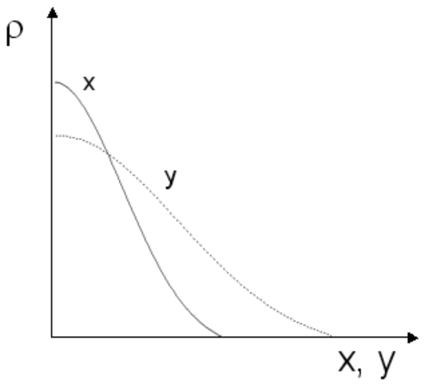

Figure 1.11: A sketch map of initial particle density in x and y direction.

As shown on the top of Fig. 1.10, the length in x direction is shorter than that in y direction in the spatial space. This results in larger density gradient in x direction than in y direction. The projection of all particles on one dimension (x or y direction) is shown in Fig. 1.11. The areas under the density curves in x and y directions are same, they are equal to total number of particles. The larger density gradient in horizontal direction (x) leads to the larger pressure gradient in this direction, if we compare with vertical direction (y). The larger pressure gradient further results in larger collective velocity. As shown at the bottom of Fig. 1.10, The anisotropy in the initial spatial space will translate into the anisotropy in the momentum space. In this process, the initial spatial anisotropy will be washed out by the momentum space anisotropy during the system expansion; on the other word, the spatial anisotropy only exists at the early stage of the collisions. Thus, the driving force quenches itself, this is so-called self-quenching effect. It makes anisotropic flow sensitive to the early stage [Sor97a].

Figure 1.12: Two components of hydrodynamic flow.

As illustrated in Fig. 1.12, the term of flow has two important aspects: (i) collectivity of produced hadrons and (ii) the local thermalization among these hadrons. Through the interactions among constituents, collectivity will be built up provided that the initial profile of the system is anisotropic. If the interactions are strong enough, the system will finally reach local equilibrium and develop hydrodynamic type flow.

1.3.2.4 Elliptic Flow v_2

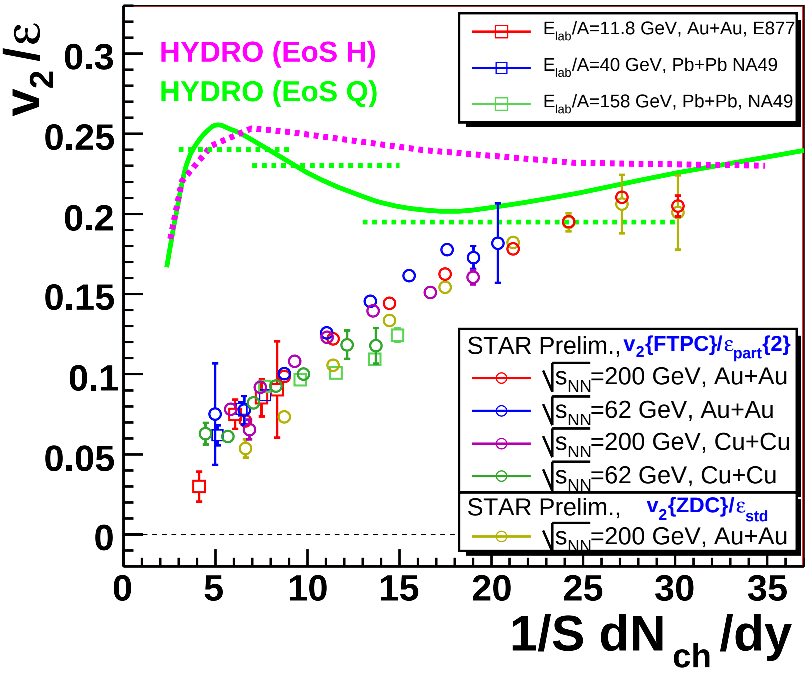

Figure 1.13: v_2/ε as a function of $1/S\ dN_{\rm ch}/dy$ for charged hadrons. The results are from AGS, SPS and RHIC. This figure is from [Vol07a].

The anisotropy of the initial profile is defined by the eccentricity:

$$\varepsilon = \frac{\langle y^2 - x^2 \rangle}{\langle y^2 + x^2 \rangle} \tag{1.7}$$

here x is the direction of impact parameter, y is the long axis which is perpendicular to beam direction and x. $\langle\ \rangle$ stand for an event by event average.

The azimuthal distribution of produced particles (with respect to the reaction plane) in the momentum space can be expressed by the Fourier expansion [Oll92a, Oll93a, Vol96a]:

$$E\frac{d^3N}{d^3p} = \frac{1}{2\pi}\frac{d^2N}{p_T dp_T dy}(1 + \sum_{n=1}^{\infty} 2v_n cos[n(\phi - \Psi_r)]) \tag{1.8}$$

where p_T, y and ϕ is the transverse momentum, rapidity, and the azimuthal angle (in the momentum space) of a particle in each event; Ψ_r is the azimuthal angle of the reaction plane in the laboratory frame. v_n is the n_{th} harmonic coefficient. v_1 which is usually called directed flow is the first order harmonic coefficient. The elliptic flow, v_2, which characterizes the ellipse shape of the azimuthal anisotropy, is the second order harmonic coefficient. According to the definition, v_2 can be written by:

$$v_2 = \langle \frac{p_x^2 - p_y^2}{p_x^2 + p_y^2} \rangle \tag{1.9}$$

Where p_x and p_y are the momentum components in the transverse plane.

As we discussed before, the local thermalization is one of the characteristics of QGP. Thus it is important to investigate whether the system created in heavy ion collisions reaches the thermalization. It is argued in Ref. [Vol00a] that the system size and centrality dependence of v_2 can be used to study the question of thermalization. The arguments are following: If the system reached thermalization, the elliptic flow in difference systems and centrality bins only depends on the initial geometry, namely, eccentricity. Otherwise, if the system is still away from equilibrium, for example, in the low density limit, elliptic flow depends both on the initial geometry and system size or centrality bins.

In Fig. 1.13, it shows v_2/ε as a function of $1/S\ dN_{\text{ch}}/dy$ for charged hadrons from various experiments, where S is the transverse area of the colliding system, dN_{ch}/dy is the yield of charged hadrons in the mid-rapidity. Hence, dN_{ch}/dy over S is the transverse particle density in mid-rapidity. In this plot, these results are shown: 1. Au+Au and Cu+Cu collisions at both 62.4 GeV and 200 GeV from STAR experiments; 2. Pb+Pb collisions at both 40A GeV and 158A GeV from NA49 experiments; 3. Au+Au at 11.8A GeV from E877 experiments. It can be observed that v_2/ε increases linearly as a function of $1/S\ dN_{\text{ch}}/dy$ when $1/S\ dN_{\text{ch}}/dy$ is less than 25. The particle density $1/S\ dN_{\text{ch}}/dy$ can connect to the probability of interactions between constituents. The interactions should be much more frequently in more central events if we compare to the peripheral events. One can imagine The system will reaches the equilibrium provided the interactions are

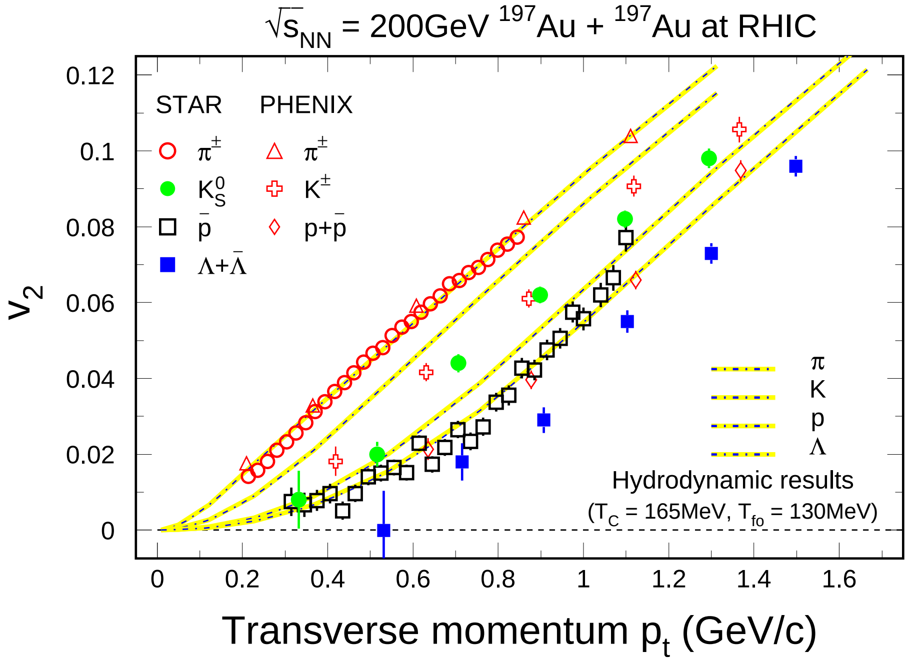

Figure 1.14: v_2 as a function of p_T for $\pi^{\pm}$, K_S^0, $\bar{p}$ ($p + \bar{p}$) and $\Lambda + \bar{\Lambda}$ in minimum bias Au+Au collisions at $\sqrt{s_{NN}}$ = 200 GeV. The results are from both STAR and PHENIX experiments. The dot-dashed lines stand for the ideal hydrodynamic calculations [Huo01a, Huo03a]. In the model calculations, early thermalization and ideal fluid expansion are assumed. The equation of state (EOS) is based on LQCD calculation, which includes a phase transition at T_c = 165 MeV and a sharp kinetic freeze-out with T_{fo} = 130 MeV [Kol03a]. The figure is from [Old04a].

strong enough. Thus, the increasing of v_2/ε as a function of particle density suggests the system created in heavy ion collisions evolves towards the thermalization in high particle density. The thermalization might be built-up in the most central Au+Au collisions at the top energy of RHIC.

In Fig. 1.14, it shows v_2 as a function of transverse momentum (low p_T region) in minimum bias Au+Au collisions at $\sqrt{s_{NN}} = 200$ GeV. The data are from STAR and PHENIX experiments at RHIC. For these presented identified particles: pion, K_S^0, proton and $\Lambda + \bar{\Lambda}$, the larger v_2 can be observed for the the heavier particle at a given p_T bin. The so-called mass ordering effect is consistent with the ideal hydrodynamic calculations [Huo01a, Huo03a] which are shown by the dot-dashed lines. In the used hydrodynamic model, the critical temperature (T_c) and the freeze-out temperature ((T_{fo})) have been set to 165 MeV and 130 MeV, respectively. To get good agreement with experimental data,the parameters of the ideal hydrodynamic model have been adjusted. Thus, the magnitude of v_2 is well reproduced.

It shows v_2 as a function of transverse momentum in minimum bias Au+Au collisions at $\sqrt{s_{NN}} = 200$ GeV in panels (a) and (b) of Fig. 1.15. v_2 as a function of transverse momentum for K_S^0 and $\Lambda+\bar{\Lambda}$ are shown, together with multi-strange baryon $\Xi^- + \overline{\Xi}^+$ and $\Omega+\bar{\Omega}$in panel (a) and (b), respectively. The results of ideal hydrodynamic model [Huo01a] are presented by dotted curves. In the intermediate p_T region ($2 < p_T < 5\mathrm{GeV}/c$), v_2 data start to saturate. This is inconsistent with the ideal hydrodynamic results. Furthermore, all particles group into two groups, baryon and meson group. The $v2$ of baryons is greater than that of mesons at a give p_T bin. The saturated v_2 of The multi-strange baryons, $\Xi^- + \overline{\Xi}^+$ and $\Omega + \bar{\Omega}$ show sizeable v_2 with that of $\Lambda + \bar{\Lambda}$within statistical errors. It is argued that multi-strange baryons have small hadronic cross section [Bar04a, Bra95a, Bra99a, Bas99b], thus they are less sensitive to the late hadronic interactions. Based on this interpretation, the elliptic flow of these multi-strange baryons should be developed at early partonic stage. It indicates that partonic collectivity has been developed at the top energy collisions of RHIC.

v_2 scaled by the number of constituent quarks as a function of p_T scaled by the number of constituent quarks for pion, proton, K_S^0, $\Lambda + \bar{\Lambda}$, $\Xi^- + \overline{\Xi}^+$ and $\Omega + \bar{\Omega}$are shown

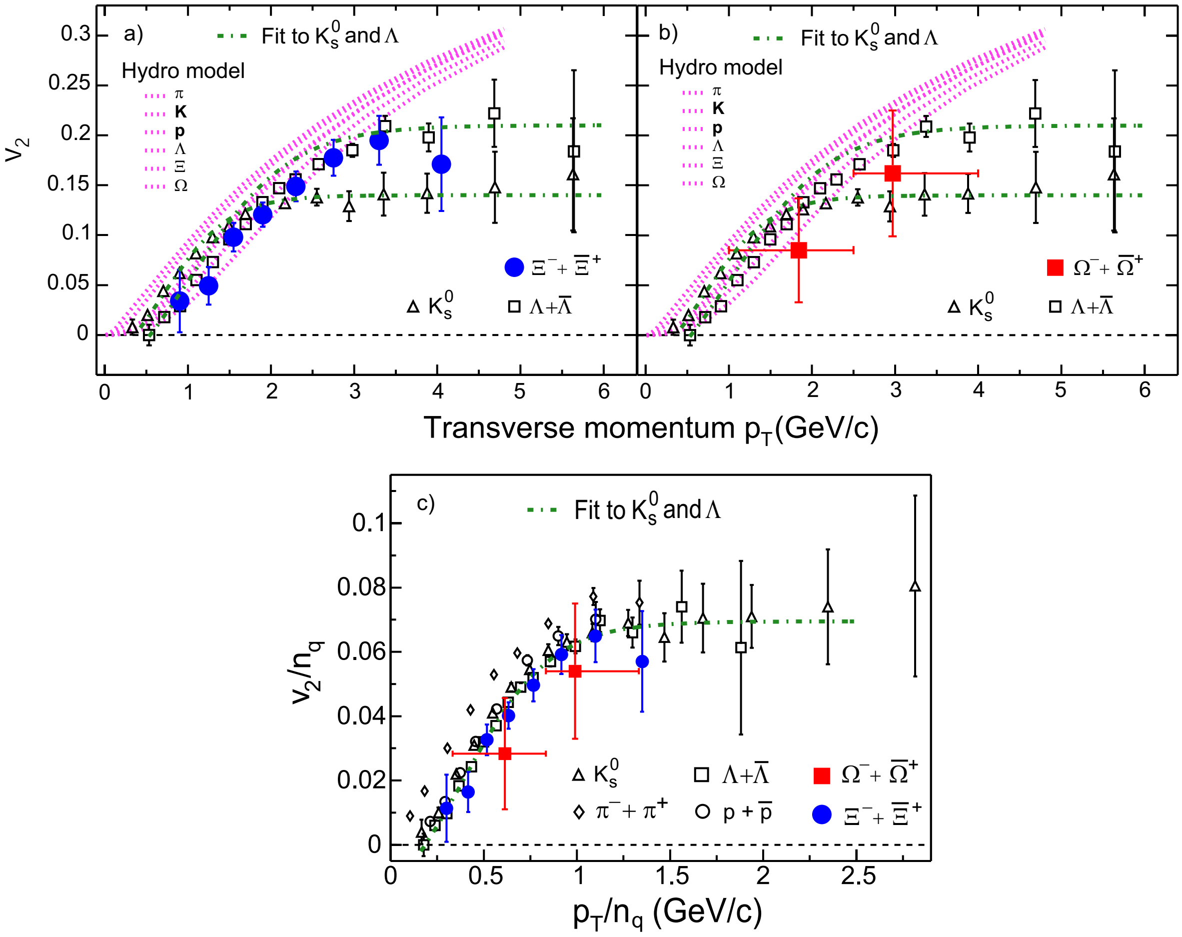

Figure 1.15: (a): v_2 as a function of transverse momentum for K_S^0, $\Lambda + \bar{\Lambda}$ and $\Xi^- + \overline{\Xi}^+$ in minimum bias Au+Au collisions at $\sqrt{s_{NN}} = 200$ GeV. The results are from STAR experiment [Ada04c]. (b): the same as (b), but $\Omega + \bar{\Omega}$ instead of $\Xi^- + \overline{\Xi}^+$. In (a) and (b), the results for K_S^0 and $\Lambda + \bar{\Lambda}$ are shown together with a fit which is represented by the dot-dashed lines. The dotted curves stand for the ideal hydrodynamics model calculations. (c): v_2 scaled by the number of constituent quarks as a function of p_T scaled by the number of constituent quarks for pion, proton, K_S^0, $\Lambda + \bar{\Lambda}$, $\Xi^- + \overline{\Xi}^+$ and $\Omega + \bar{\Omega}$. The results of π and $p + \bar{p}$ are from PHENIX experiment. The figure is from [Ada05a].

in panel (c) of Fig. 1.15. Namely, n_q is set to two for mesons, while n_q is set to three for baryons. It can be observed that all data follow an universal curve when the n_q scaled transverse momentum is greater than 1 GeV/c. This scaling in v_2 is usually named Number of constituent Quark (NQ) scaling.

Theorists found quark recombination and coalescence models [Fri03a, Gre03a, Lin02a, Vol02a] can roughly explain the NQ scaling. In these models, it assumes that the elliptic flow of hadrons is developed by recombining constituent quarks into hadrons. Before the constituent quarks form hadrons, these quarks develop a certain amount of elliptic flow. This suggests that the system has been in a deconfined state prior to hadronization and quarks are the effect degree of freedom of the matter created in heavy ion collisions at RHIC.

1.4 Thesis Motivation

In this thesis, we will present the v_2 measurement of charged hadrons and strange hadrons in Au+Au and Cu+Cu collisions with different beam energies at RHIC-STAR experiment. Our main motivations and goals are as follows:

1. The previous results mainly focus on the v_2 measurement in Au+Au collisions. Since the conditions in Au+Au collisions might not hold in smaller systems and at lower beam energies, the system-size and beam-energy dependence of identified hadron v_2 will shed light on the systematic properties of partonic collectivity and quark degrees of freedom. Further, the study of v_2 in collisions of nuclei smaller than Au+Au will allow us to test the early thermalization hypothesis in Au+Au collisions. To date, there are only a few studies of identified hadron v_2 in Cu+Cu collisions. In this thesis, we present the results of v_2 for charged hadrons, K_S^0, $\Lambda + \bar{\Lambda}$ and $\Xi^- + \overline{\Xi}^+$ in Cu+Cu collisions at$\sqrt{s_{NN}}$ = 62.4 and 200 GeV.

2. The Number of Quark scaling reflects constituent quark is the most effect degree of freedom in determining hadron flow at intermediate p_T. This suggests that the system has been in the deconfined state prior to hadronization. We will discuss the partonic

collectivity by testing the validity of the NQ scaling in collisions at RHIC and measuring the v_2 for multi-strange hadrons ϕ, $\Xi^- + \overline{\Xi}^+$ and $\Omega + \bar{\Omega}$.

3. The centrality and system size dependence of v_2 is related to the physics of the system created in high energy nuclear collisions. Since in the ideal hydrodynamic limit the centrality dependence of v_2 is mostly defined by the elliptic anisotropy of the overlapping region of the colliding nuclei, and in the low density limit by the product of the elliptic anisotropy and the multiplicity, it should be a good indicator of the degree of equilibration reached in the reaction. We will present a systematical study of centrality and system size dependence of v_2.

4. Theoretical analyses found that the centrality and system size dependence of v_2 can be described by a simple model based on eccentricity scaling and incomplete thermalization. Within these models the lack of perfect equilibration allows for estimates of the effective parton cross section in the quark-gluon plasma and of the viscosity to entropy density ratio (η/s) [Oll07a]. Thus, the v_2 results in this thesis should allow extrapolation to the ideal hydrodynamic limit and extraction of η/s.

The rest of the thesis is organized as following. Chapter 2 will review the facilities used to study heavy-ion collisions. The Relativistic Heavy Ion Collider (RHIC) and its programs will be discussed. The STAR detector system will be discussed in more details. Chapter 3 includes analysis methods. Techniques for measuring charged hadron and strange hadron v_2 and different flow methods will be discussed. Chapter 4 will present the results of this analysis. Chapter 5 will stimulate discussions on centrality dependence of v_2 measurements. Chapter 6 will give summary and outlook. In the following, we use $h^{\pm}$, Λ, Ξ and Ω to denote charged hadron, $\Lambda + \bar{\Lambda}$, $\Xi^- + \overline{\Xi}^+$ and $\Omega + \bar{\Omega}$, respectively.

CHAPTER 2

Experimental Setup

2.1 An Introduction to the Relativistic Heavy-Ion Collider

The Relativistic Heavy-Ion Collider (RHIC) which is the first experimental facility designed to collide the heavy-ion beams locates at Brookhaven National Laboratory in Upton, New York. The top energy is $\sqrt{s_{NN}} = 200$ GeV for gold beams and $\sqrt{s} = 500$ GeV for proton beams at RHIC. The Large Hadron Collider (LHC) which was built by the European Organization for Nuclear Research (CERN) were were successfully running last year. It is designed for p+p collisions up to $\sqrt{s} = 14$ TeV and Pb+Pb collisions up to $\sqrt{s_{NN}} = 5.5$ TeV.

There are two concentric storage rings in the RHIC, Blue Ring and Yellow Ring. Blue Ring is designed for clockwise beam, while the Yellow Ring is designed for the counter-clockwise beam. The beams of ions are bent and focused by the super conducting magnets in the ring. Because of these two independent rings and sources of ions, different kinds of collisions are possible at RHIC, for example, equal species of ions (Au+Au , p+p), unequal species of ions (d+Au). The beams can collide with each other at different place at RHIC along their 3.8 km circumference, for example, six o'clock and eight o'clock position. In Tab. 2.1, it shows the basic design parameters of RHIC. For gold ion beams, the top energy is 100 GeV/u. This number depends on the charge over mass ratio of the ions. Thus, the top energy is 125 GeV/u for beams of lighter ion and 250 GeV/u for proton beams. The mean luminosity is 8×10^{26} cm$^{-2}s^{-1}$ in Au+Au collisions at $\sqrt{s_{NN}} = 200$ GeV; with electron cooling, the luminosity can reach 7×10^{27} cm$^{-2}s^{-1}$.

The mean luminosity is 2.4×10^{32} cm$^{-2}s^{-1}$ in p+p collisions at $\sqrt{s} = 250$ GeV; with electron cooling, the luminosity is 8×10^{32} cm$^{-2}s^{-1}$.

	Gold beam
Top energy	100 GeV/u
Nominal luminosity	1×10^{26} cm$^{-2}s^{-1}$
life time	10 hours

Table 2.1: The basic performance parameters for gold beam at RHIC.

In Fig. 2.1, it shows the whole acceleration process at RHIC. In the injector chain, three accelerators can strip electrons around the atoms and accelerate ions at the same time.

The ion source of Tandem Van Graaff provides the gold atoms. Then the gold atoms are stripped of the electrons partially and accelerated to 1 MeV/u. At the exit of Tandem, the gold atoms are stripped further and selected by the magnets. The Booster Synchrotron accelerates the beams of gold ions (+32e) to 95 MeV/u in the next step. At the exit of the Booster Synchrotron, the gold ions are stripped again and reaches +77e charge state. The beams with these gold ions (+77e) are injected to the Alternating Gradient Synchrotron and accelerated to 10.8 GeV/u. At the exit of the Alternating Gradient Synchrotron, the gold ions are stripped to the charge state of +79e finally, and then, injected to the RHIC. Beams of ions can be accelerated to the required energy by the last step at RHIC.

2.2 Experimental Programs at RHIC

Four experimental groups locate at RHIC. The STAR collaboration and the PHENIX collaboration are two big programs. The STAR collaboration locates at the position of 6 o'clock, and the PHENIX collaboration locates at the position of 8 o'clock. Besides the STAR collaboration and the PHENIX collaboration, there are two relatively smaller programs: the PHOBOS collaboration and the BRAHMS collaboration. The PHOBOS collaboration locates at the position of 10 o'clock, and the BRAHMS collaboration lo-

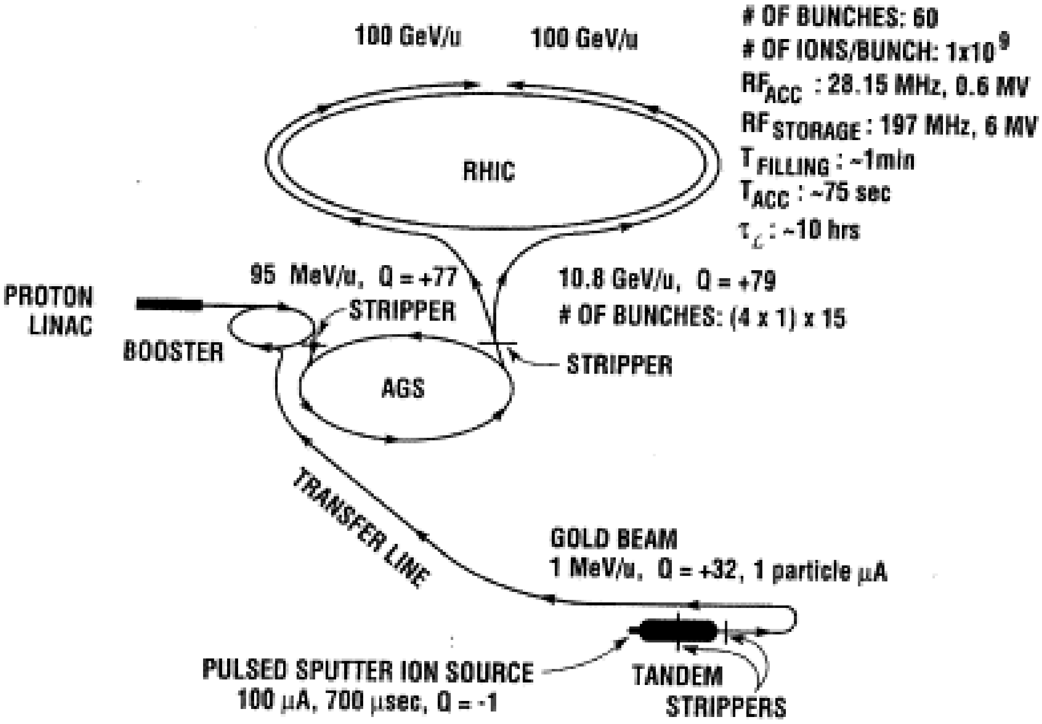

Figure 2.1: The Relativistic Heavy-Ion collider together with the facilities accelerating the beams to the injection energy of RHIC.

cates at the position of 2 o'clock. In Fig. 2.2, the detectors of STAR, PHENIX, PHOBOS and BRAHMS (global view) are shown.

STAR detectors have large acceptance of two pi azimuthal angle. The experiment at STAR [Ack03a] mainly focuses on event by event correlations and fluctuations, particle identification and jet like correlations. The main detector Time Projection Chamber (TPC) covers the mid-rapidity, $|\eta| < 1.3$. In the forward rapidity, $2.5 < |\eta| < 4$, there are Forward Time Projection Chambers. We will introduce the detectors at STAR in detail later.

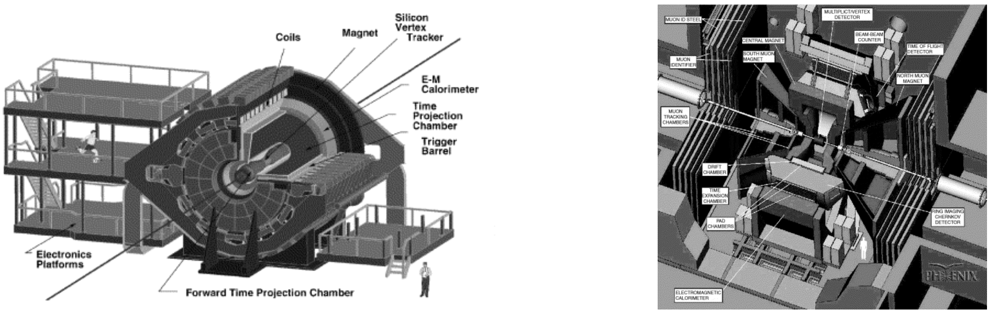

STAR detectors PHENIX detector

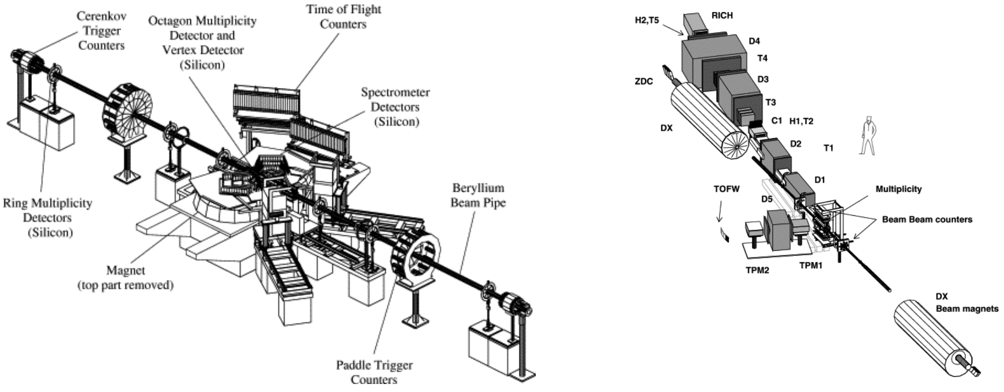

PHOBOS detectors BRAHMS detectors

Figure 2.2: The detectors of the STAR, PHENIX, PHOBOS and BRAHMS programs at RHIC.

PHENIX detectors have relatively smaller acceptance but are detectors with fast data taking. The experiment at PHENIX [Adc03a] mainly focuses on heavy flavor, copiously produced hadron identification (pion, kaon and proton) and lepton identification. A spectrometer with two arms and systems of tracking, which is used to record the information of electrons, hadrons and photons at mid-rapidity, locates in the center. It has $2\times\pi/2$ acceptance and overs mid-rapidity, $|\eta| < 0.35$. There are two muon spectrometers in the forward direction, which are used to measure muons at forward rapidity, covering $1.1 < |\eta| < 2.4$ with two pi azimuthal angle acceptance.

BRAHMS detector consists of two small solid-angle spectrometers. The propose of BRAHMS experiment is for measuring charge particles over a wide range of rapidity, $0 < y < 4$ with the transverse momentum region of, $0.2 < p_T < 3.0\ GeV/c$.

The main detectors of PHOBOS experiments [Bac03a] are a multiplicity detector and two spectrometer arms in the mid-rapidity. It is designed to detect charge particles using a multiplicity detector in the full azimuthal and measure identified particles around mid-rapidity.

2.3 STAR Detectors

As we discussed above, the Solenoidal Tracker, STAR, is mainly designed for measuring event by event correlations and fluctuations, particle identification and jet like correlations. With the energy in the Time Projection Chamber, pion and kaon can be identified up to 0.7 GeV and proton can be identified up to 1.1 GeV. By the decay topology, many kinds of particles can be reconstructed, such as, K_S^0, Λ, ϕ and Ω and so on. Thus, one can study the hadron yields and p_T spectra by the good ability of particle type identification; also correlations and fluctuations could be studied for different particle species.

Figure 2.3 is a cutaway plot for the STAR detectors. There are many detectors locating at different places at STAR. The STAR detector are surrounded by a large magnet [Ber03a], the magnitude of the magnet is 0.25 Tesla for half field and 0.5 Tesla for full field. The beam pipe [Mat03a] was made by Berillium. This material can minimize particles scatterings and conversions of photons, because of its low charge of nuclear and low density. The Time Projection Chamber (TPC) [And03a] is the most important detector at STAR. It record the information of tracks at mid-rapidity (the full coverage is $|\eta| < 1.8$). In the forward rapidity, $2.5 < |\eta| < 4$, the information of tracks are record by

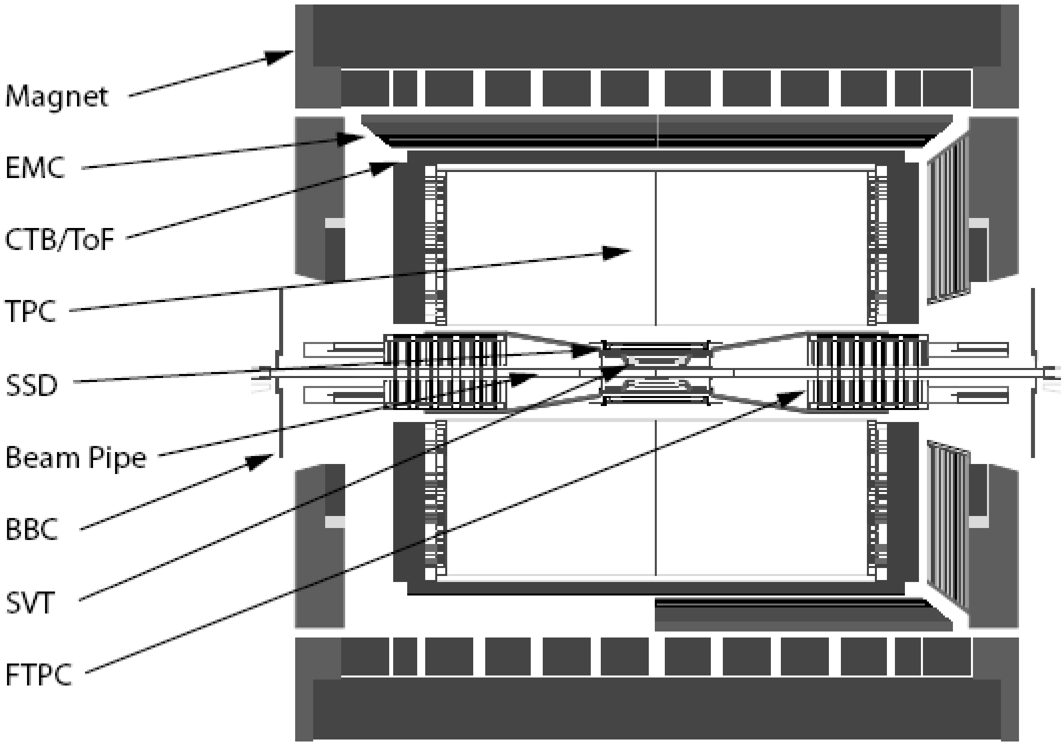

Figure 2.3: STAR detectors (cutaway view).

two Forward Time Projection Chambers (FTPC) [Ack03b]. Both TPC and FTPCs have the two pi azimuthal acceptance. The Silicon Vertex Tracker (SVT) [Bel03a] and the Silicon Strip Detector (SSD) [Arn03a] had been used for providing precise primary vertex and improving the resolution of hit points of tracks. They were took out after the seventh run (2007) at RHIC. The full Barrel ElectroMagnetic Calorimeter (BEMC) [Bed03a] and the End cap ElectroMagnetic Calorimeter (EEMC) [All03a] are on the west of STAR. BEMC and EEMC are used to identify photons and electrons. In the rapidity region of $2.5 < \eta < 3.5$, the Photon Multiplicity Detector (PMD) [Agg03a] records the information of the spatial distribution of photons. TPC can identify particle type by the energy loss. Pion and kaon can be identified up to 0.7 GeV, while proton can be identified up to 1.1 GeV. To extend the particle identification ability at STAR, the full Time Of Flight (TOF) [Bon03a], which covers rapidity region of $-1 < \eta < 1$ with two pi full azimuthal coverage, has installed in 2009.

The upgrade program of STAR detectors are under progress to expand the detection capabilities and physics program. TOF upgrade which has been finished successfully in 2009 improves the ability of particle identification. With the incoming Heavy Flavor Tracker (HFT) [Wie06a], direct reconstruction of heavy quark contained hadrons, such as J/ψ, D mesons, will be possible. Systematic study of heavy quark contained hadrons will help us to understand the properties of the hot and matter created in heavy ion collisions and determine the Equation of State finally.

CHAPTER 3

Analysis Method

In this chapter, we present the selection criteria for events and tracks, reconstruction of K_S^0, Λ, Ξ and Ω, event plane determination, the analysis methods for v_2 measurement, and systematic uncertainties on v_2.

3.1 Event and Track Selection

The data set used in this thesis consists of, minimum bias events for Cu+Cu collisions at $\sqrt{s_{NN}}$ = 200 GeV and 62.4 GeV taken during run V and minimum bias Au+Au events at $\sqrt{s_{NN}}$ = 200 GeV and 9.2 GeV taken during run VII.

Trigger Setup Name	Production	Vertex Cut	Trigger ID	Events No.
cuProductionMinBias	P06ib	$\|V_z\| < 30$ cm	66007	28 M
cuProductionHighTower	P06ib	$\|V_z\| < 30$ cm	66007	10 M

Table 3.1: Run V trigger and events selection in minimum bias Cu+Cu collisions at $\sqrt{s_{NN}}$ = 200 GeV.

Trigger Setup Name	Production	Vertex Cut	Trigger ID	Events No.
cu62ProductionMinBias	P05id	$\|V_z\| < 30$ cm	76007, 76011	17 M

Table 3.2: Run V trigger and events selection in minimum bias Cu+Cu collisions at $\sqrt{s_{NN}}$ = 62.4 GeV.

The trigger and event selection are summarized in Table 3.1-3.4. Events with the z position of vertex (V_z) further than 30 cm (75 cm for 9.2 GeV Au+Au dateset) from the main TPC center were discarded. Events useful for our analysis are listed in the

Trigger Setup Name	Production	Vertex Cut	Trigger ID	Events No.
ProductionMinBias	P08ic	$\lvert V_z\rvert < 30$ cm	200001, 200003, 200013	55 M
Production2	P08ic	$\lvert V_z\rvert < 30$ cm	200001, 200003, 200013	11 M

Table 3.3: Run VII trigger and events selection in minimum bias Au+Au collisions at $\sqrt{s_{NN}}$ = 200 GeV.

Trigger Setup Name	Production	Vertex Cut	Trigger ID	Events No.
ProductionMinBias	P08ic	$\lvert V_z\rvert < 75$ cm	minimum bias	3 k

Table 3.4: Run VII trigger and events selection in minimum bias Au+Au collisions at $\sqrt{s_{NN}}$ = 9.2 GeV.

most right column. The total number of minimum bias events is 38 million for 200 GeV Cu+Cu data set, 17 million for 62.4 GeV Cu+Cu data set, 66 million for 200 GeV Au+Au data set and 3 k for 9.2 GeV Au+Au data set.

Centrality Bin	Multiplicity	Geometric Cross Section
1	19-29	$50-60\%$
2	30-45	$40-50\%$
3	46-66	$30-40\%$
4	67-97	$20-30\%$
5	98-138	$10-20\%$
6	$\geq$139	$0-10\%$

Table 3.5: Run V centrality bins in Cu+Cu collisions at $\sqrt{s_{NN}}$ = 200 GeV.

I would be necessary to introduction the definitions of different kinds of tracks here. TPC can record the hit points of each track. The global track can be gotten by a fit of helix function to the hit points directly. Usually, we define the primary collisions vertex based on all global tracks in each event. The primary track can be gotten by a fit of helix function to the hit points together with the identified primary vertex. The total number of tracks in each event recorded by the TPC can be used to define centrality bins of collisions. The reference multiplicity is defined as following: the number of the

Centrality Bin	Multiplicity	Geometric Cross Section
1	14-21	$50-60\%$
2	22-32	$40-50\%$
3	33-48	$30-40\%$
4	49-70	$20-30\%$
5	71-100	$10-20\%$
6	≥101	$0-10\%$

Table 3.6: Run V centrality bins in Cu+Cu collisions at $\sqrt{s_{NN}} = 62.4$ GeV.

Centrality Bin	Multiplicity	Geometric Cross Section
1	10-20	$70-80\%$
2	21-38	$60-70\%$
3	39-68	$50-60\%$
4	69-113	$40-50\%$
5	114-177	$30-40\%$
6	178-268	$20-30\%$
7	269-398	$10-20\%$
8	399-484	$5-10\%$
9	≥485	$0-5\%$

Table 3.7: Run VII centrality bins in Au+Au collisions at $\sqrt{s_{NN}} = 200$ GeV.

Centrality Bin	Multiplicity	Geometric Cross Section
1	17-73	$30-60\%$
2	74-161	$10-30\%$
3	≥162	$0-10\%$

Table 3.8: Run VII centrality bins in Au+Au collisions at $\sqrt{s_{NN}} = 9.2$ GeV.

primary tracks recorded by the TPC with fifteen or more hit fit points and a Distance of the Closest Approach (DCA) to the primary collision vertex (gDca) no more than 3 cm (gDca < 3 cm) with the rapidity region of $-0.5 < \eta < 0.5$.

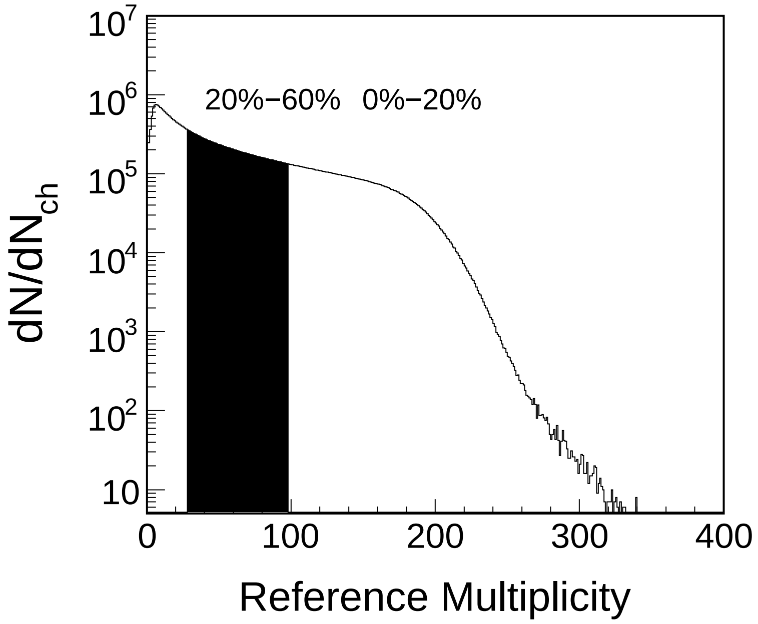

Figure 3.1: The reference multiplicity distribution in Cu+Cu collisions at $\sqrt{s_{NN}} = 200$ GeV. The geometry cross section used for v_2 analysis is combined into two centrality intervals shown in the Figure.

The inclusion of inner tracking for the Run VII Au+Au 200 GeV data rendered reference multiplicity a poor method to determine centrality. There is a dependence on the primary vertex position for the reconstruction efficiency in the $|V_z| < 30$ cm region. The dependence was generally absent for TPC tracking only used in many of the previous productions, and is undesirable since it requires the centrality cuts to change as a function of V_z. To this end, another variable called global reference multiplicity (gRefmult) was introduced. The only difference between the reference multiplicity and global reference multiplicity is that the global reference multiplicity requires the primary tracks in the TPC with the 10 or more fit points. The remaining issues are biases on multiplicity distribution introduced by the main online Vertex Position Detector (VPD) trigger setup (200013). The biases come from two sources. Firstly, over the full range in V_z, the VPD is more efficient at triggering on central events relative to peripheral.

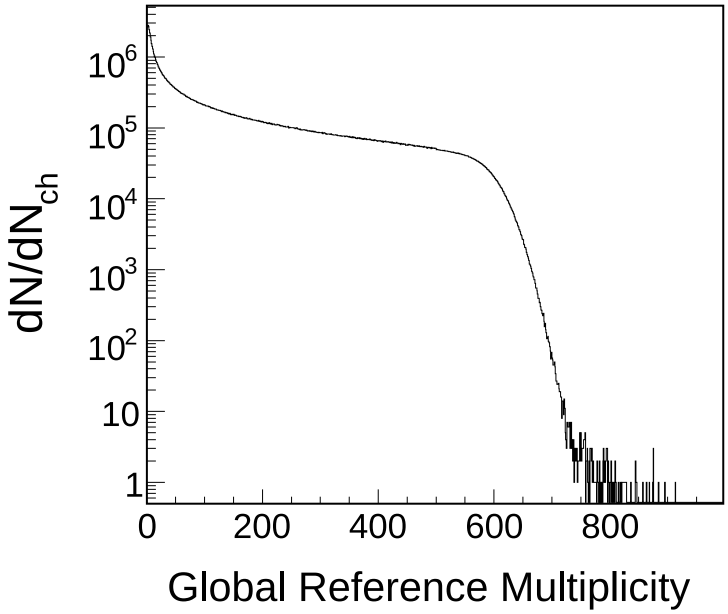

Figure 3.2: The Global reference multiplicity (gRefmult) distribution in Au+Au collisions at $\sqrt{s_{NN}} = 200$ GeV.

This leads to a general deficit in peripheral events for a given data sample. The second comes from a centrality dependence of the VPD's online V_z resolution which is worse for peripheral events relative to central. Since the trigger setup (200013) insisted events fall within the inner tracking acceptance i.e. with an online cut of $|V_z| < 5$ cm, the resolution issue means that events at the higher $|V_z|$'s are more likely to peripheral whereas the events at lower $|V_z|$'s are more likely to be central. The V_z dependent biases in multiplicity distribution require a re-weighting correction to be applied for all analysis. The correction has to be applied as a function of V_z in 2 cm bins for acceptance reasons. In a given V_z bin, firstly the weights have to be determined. This is done by normalizing the 1D global reference multiplicity distribution by the number of events with global reference multiplicity > 500. The ideal multiplicity distribution from MC Glauber then has to be divided by the normalized global reference multiplicity distribution to calculate the weights.

The centrality bins and the corresponding geometric cross section for Cu+Cu and Au+Au collisions are listed in Table 3.5 - 3.8. The geometric cross section listed in Table 3.5 - 3.7 list the definition of centrality bins for the data set we mentioned before.

Figure 3.1 shows reference multiplicity distribution without the Glauber correction in Cu+Cu collisions at $\sqrt{s_{NN}} = 200$ GeV. Events more peripheral than 60% centrality are not used in the analysis. The three combined centrality bins used in the analysis are $0-20\%$, $20-60\%$ and $0-60\%$, which are indicated in the Figure 3.1. Figure 3.2 shows global reference multiplicity distribution with the re-weighting correction mentioned before.

3.2 K_S^0, Λ, Ξ and Ω Reconstruction

We reconstruct K_S^0, Λ, Ξ and Ω through their weak decay channels. The properties of these decays are summarized in Table 3.9.

Particle Type	Decay Channel	Branching Ratio (%)	$c\tau$ (cm)	Mass (GeV/c^2)
K_S^0	$\pi^+ + \pi^-$	68.95 ± 0.14	2.68	0.497
$\Lambda(\bar{\Lambda})$	$p + \pi^-$ $(\bar{p} + \pi^+)$	63.9 ± 0.5	7.89	1.115
Ξ^- $(\bar{\Xi}^+)$	$\Lambda + \pi^-$ $(\bar{\Lambda} + \pi^+)$	99.89 ± 0.04	4.91	1.321
Ω^- $(\bar{\Omega}^+)$	$\Lambda + K^-$ $(\bar{\Lambda} + K^+)$	67.8 ± 0.7	2.46	1.672

Table 3.9: K_S^0, Λ, Ξ and Ω weak decay properties

3.2.1 K_S^0 and Λ Reconstruction

The weak decay topology is used to reconstruct K_S^0 and $\Lambda(V^0)$. We usually call them V^0, as they are neutral and the decay topology looks like letter "V". The decay channel can be found in Tab. 3.9. The decayed daughters, p and π, are identified though the energy loss (dE/dx) in the TPC. As the information of momentum and mass for each daughter is known, one can calculate the invariant mass for the V^0 candidate. Of course, there are many fake V^0 candidates. It may be because of the misidentification of the daughters or daughters from different V^0 or other correlations between the daughters, and so on. The fake V^0 candidates are called combinatorial background.

Figure 3.3 shows the decay topology for V^0. By the distance of closet approach (dca) between the daughters, the information on the decay vertex can be determined. One can imagine, the fake decay vertexes should exhibit quite larger distance of closet approach between daughters (fake) than the real one. Dca1 and Dca2 in the plot are the distance of closet approach of the negative and positive daughter to the primary collisions vertex. As the real primary tracks are emitted from the primary collisions vertex, the distance of closet approach to the primary collisions vertex should approach to zero. We can apply this cut for selecting the real decay daughters. The distance of closet approach of the $\overrightarrow{p}$ direction of V^0 to the primary collisions vertex is represented by b in the topology plot. If the V^0s are directly created in the collisions, the value of b is close zero. rv is decay length of V^0.

In order to reduce the combinatorial background, optimized decay topology cuts are used in the analysis. In the following, we take the decay length of V^0 as an example. As listed in Tab. 3.9, the decay length ($c\tau$) for K_S^0 and Λ is 2.68 cm and 7.89 cm, respectively. Thus, the vertexes of decay are a few centimeters away from the primary collision vertex. So we can exclude some fake decay vertexes by the cut of DCA from primary collisions vertex to V0.

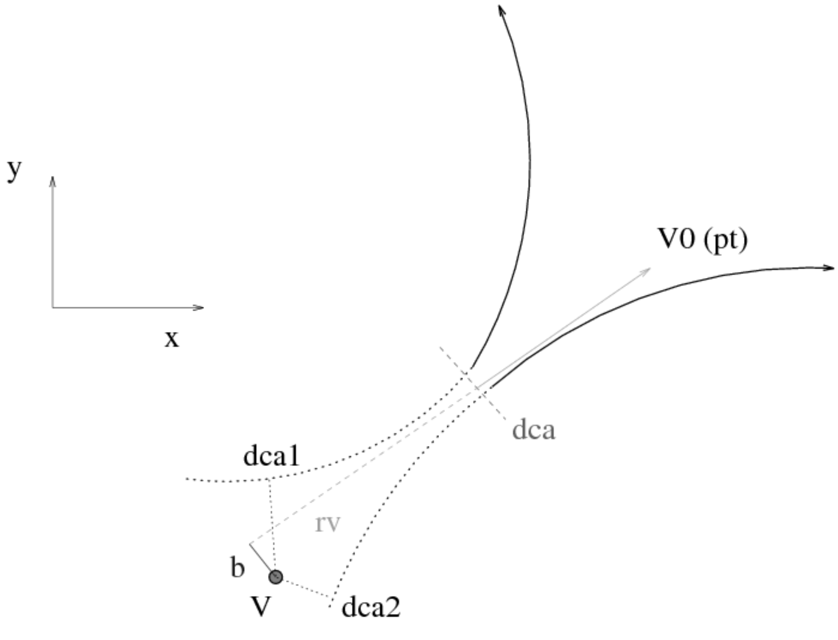

Figure 3.3: The decay topology for V^0. This figure is from [Mar98a]

The optimized cuts for K_S^0 and Λ in Cu+Cu collisions at $\sqrt{s_{NN}} = 200$ GeV are listed in Tab. 3.10 and Tab. 3.11, respectively. These cuts are the default cuts applying

p_T (GeV/c)	< 0.8	0.8-3.6	> 3.6
π dca to primary vertex (cm)	> 1.5	> 1.0	> 0.5
dca between daughters (cm)	< 0.7	< 0.75	< 0.5
dca from primary vertex to V0	< 0.7	< 0.75	< 0.5
decay length (cm)	4-150	4-150	10-120

Table 3.10: Cuts selection criteria for K_S^0 in Cu+Cu collisions at $\sqrt{s_{NN}} = 200$ GeV.

p_T (GeV/c)	< 0.8	0.8-3.6	> 3.6
π dca to primary vertex (cm)	> 2.5	> 2.0	> 1.0
p dca to primary vertex (cm)	> 1.0	> 0.75	> 0
dca between daughters (cm)	< 0.7	< 0.75	< 0.4
dca from primary vertex to V0	< 0.7	< 0.75	< 0.75
decay length (cm)	4-150	4-150	10-125

Table 3.11: Cuts selection criteria for Λ in Cu+Cu collisions at $\sqrt{s_{NN}} = 200$ GeV.

to the v_2 analysis.

3.2.2 Ξ and Ω Reconstruction

The decay topology for multi-strange hadrons, Ξ and Ω, is a little bit complicated than V^0's. We usually call it cascade topology, which you can find it in Fig. 3.4. Both Ξ and Ω decays into a pion (kaon) with the same charge of Ξ or Ω and a Λ baryon with zero charge. Then, the Λ daughter decays into a π and a p, which can be reconstructed by the V^0 topology as mention before. The final three daughter tracks are shown in Fig. 3.4 by solid curves. Hence, there are two steps to reconstruct Ξ and Ω: firstly, reconstructing Λ by the V^0 topology; then, finding the suitable Λ together with another bachelor daughter (charged pion or kaon) to reconstruct Ξ and Ω.

The combinatorial background in the reconstruction can be reduced by applying the decay topology cuts. There are seven possible criteria for topological cut, as shown in Fig. 3.4: Distance of closest approach of $\Xi(\Omega)$ to the primary collision vertex, dca $\Xi(\Omega)$

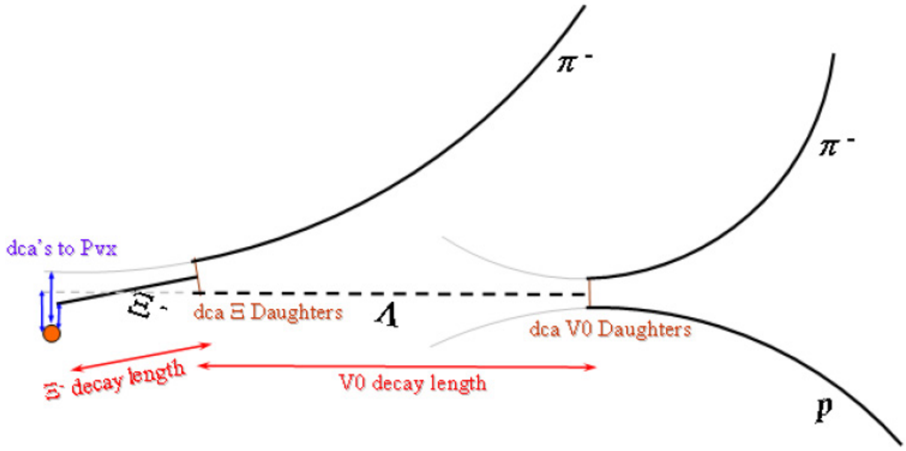

Figure 3.4: The decay topology for multi-strange hadrons, Ξ and Ω. Here the Ξ^- decay topology is shown as an example. Solid curves represent three daughter tracks (two charged pions and a proton). The dashed curve represents Λ daughter in the decay. The possible criteria for topological cut are all shown in the plot.

to PVx; Distance of closest approach of the Λ daughter to the primary collision vertex, dca Λ to PVx; Distance of closest approach of the bachelor daughter pion(kaon) to the primary vertex, dca Bach. to PVx; Distance of closest approach between $\Xi(\Omega)$ daughters, Λ and the bachelor daughter pion (kaon); Distance of closest approach between Λ daughters, the proton and pion; The decay length of multi-strange hadron, $\Xi(\Omega)$; The decay length of Λ daughter.

Table 3.12 lists the optimized cuts for Ξ (a) and Ω (b) in collisions at $\sqrt{s_{NN}} = 200$ GeV.

3.2.3 Invariant Mass Distributions

Figure 3.5 shows K_S^0, Λ, Ξ and Ω invariant mass distribution in $\sqrt{s_{NN}} = 200$ GeV Cu+Cu collisions for a selected p_T region in mini-bias collisions $(0-60\%)$. The red dashed lines are the background estimation.

For K_S^0 and Λ, the remaining backgrounds are estimated from the fit to the invariant mass distribution with functions describing signals and backgrounds. The fit function is

Cut Parameter	Cut Value
dca Ξ to PVx	< 0.4
dca bach. to PVx	> 1.5
dca Λ to PVx	> 0.1
dca Λ to bach.	< 0.7
dca p to π daug.	< 0.7
dl Ξ	≥ 5 cm
dl Λ	$> 23 - 4 \times$ dl Ξ
mass Λ	± 0.007 GeV/c^2
nHits bach.	≥ 25
nHits p	≥ 25
nHits π	≥ 25
N. $\sigma_{dE/dx}$ bach.	3
N. $\sigma_{dE/dx}$ p	3
N. $\sigma_{dE/dx}$ π	3

(a)

Cut Parameter	Cut Value
dca Ω to PVx	< 0.6
dca bach. to PVx	$> 0.1 + 1.6 \times \sqrt{\text{dca}\Omega \text{ to PV}}$
dca Λ to PVx	$> 0.1 + 1.8 \times \sqrt{\text{dca}\Omega \text{ to PV}}$
dca Λ to bach.	< 0.5
dca p to π daug.	< 0.3
dl Ξ	≥ 3.2 cm
dl Λ	≥ 3.2 cm
mass Λ	± 0.007 GeV/c^2
nHits bach.	≥ 30
nHits p	≥ 30
nHits π	≥ 25
N. $\sigma_{dE/dx}$ bach.	3
N. $\sigma_{dE/dx}$ p	3
N. $\sigma_{dE/dx}$ π	3

(b)

Table 3.12: Selection parameters for Ξ (a) and Ω (b) in Au+Au collisions at $\sqrt{s_{NN}} = 200$ GeV . dca is the abbreviation of distance of closest approach, dl is the abbreviation of decay length, bach. is the abbreviation of bachelor, daug. is the abbreviation of daughter, and PVx is the abbreviation of primary collision vertex.

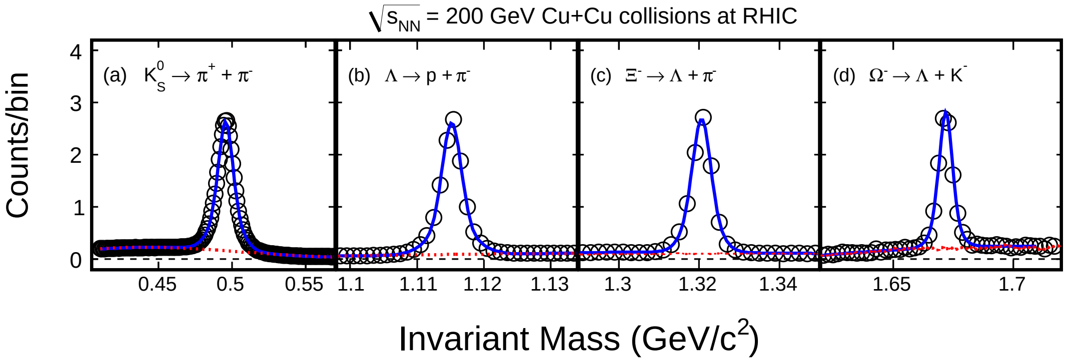

Figure 3.5: Invariant mass distributions for (a) K^0_S ($1.2 < p_T < 1.4$ GeV/c), (b) Λ ($1.4 < p_T < 1.6$ GeV/c), (c) Ξ ($1.25 < p_T < 1.75$ GeV/c) and (d) Ω ($0 < p_T < 10$ GeV/c) in $\sqrt{s_{NN}}$ = 200 GeV Cu+Cu minimum bias ($0-60\%$) collisions. The dashed lines are the background estimation from the fit to the invariant mass distribution for K^0_S and Λ, the reconstruction of pion (kaon) and rotated Λ track pairs for Ξ and Ω. For clarity, the invariant mass distributions for K^0_S, Λ, Ξ and Ω are scaled by 1/50 000, 1/130 000, 1/5 000 and 1/1 000, respectively. The error bars are shown only for the statistical uncertainties.

two gaussian plus a polynomial. We use two gaussian functions with the same mass peak parameter to describe signal and use a polynomial function to describe the backgrounds. The fourth and second order polynomial functions are used in order to estimate the systematic errors from background uncertainties. The systematic error is a few percent, we will discuss in details later. The background distribution is estimated from the polynomial in the fit. The signal distribution is estimated by data minus polynomial. The signal over total ratio distribution and background over total ratio distribution (fit over data) will be used to extract K^0_S and Λ signal v_2 .

For Ξ and Ω, the background can be reproduced by rotating the Λ candidate by 180^0 in the transverse plane and then reconstructing the Ξ and Ω candidates. The rotation of the Λ breaks the correlation in the invariant mass and therefore mimics the background of uncorrected decay pairs.

3.3 Event Plane

In this section, we introduce the Fourier expansion of azimuthal particle distribution and its properties with respect to the reaction plane. And we also introduce event plane which is the estimate of the true reaction plane determined by using the signal of flow itself.

3.3.1 Fourier Expansion of Azimuthal Distribution

Since the azimuthal distribution of emitted particles $dN/d\phi$ is the periodic function with 2π fundamental period, it is natural to expand azimuthal distribution into fourier series with 2π period.

$$\begin{aligned}\frac{dN}{d\phi} &= \frac{x_0}{2\pi} + \frac{1}{\pi}\sum_{n=1}^{\infty}(x_n\cos(n\phi) + y_n\sin(n\phi)) \\ &= \frac{x_0}{2\pi}(1 + 2\sum_{n=1}^{\infty}(\frac{x_n}{x_0}\cos(n\phi) + \frac{y_n}{y_0}\sin(n\phi)))\end{aligned} \tag{3.1}$$

Because there is only a finite number of particles in each event, the Fourier coefficients x_n and y_n can be expressed as:

$$x_n = \int_0^{2\pi} d\phi\frac{dN}{d\phi}\cos(n\phi) = \sum_{n=1}^{M} w_i\cos(n\phi_i) \equiv Q_x \tag{3.2}$$

$$y_n = \int_0^{2\pi} d\phi\frac{dN}{d\phi}\sin(n\phi) = \sum_{n=1}^{M} w_i\sin(n\phi_i) \equiv Q_y \tag{3.3}$$

where i runs over all particles (M) used to determined the event plane, ϕ_i is the azaimuthal angle of the emitted i^{th} particle and w_i is the weight (p_T, ϕ etc) to minimize the dispersion of event plane (i.e. maximum event plane resolution). We define the following two-dimentional vector $\mathbf{Q} = (Q_x,\ Q_y)$ called as a flow vector.

If we assume ϕ in Eq. 3.1 is defined relative to the reaction plane, then $dN/d\phi$ becomes an even function and we can omit y_n terms since the integration would be zero in Eq. 3.3,

$$\frac{dN}{d\phi} = \frac{x_0}{2\pi}(1 + 2\sum_{n=1}^{\infty}\frac{x_n}{x_0}\cos(n\phi)) = \frac{x_0}{2\pi}(1 + 2\sum_{n=1}^{\infty}\frac{x_n}{x_0}\cos(n[\phi_{\mathrm{lab}} - \Psi])) \tag{3.4}$$

Where ϕ_{lab} is the azimuthal angle of fixed orientation in the experiment, Ψ is the azimuthal angle of true reaction plane and $v_n = x_n/x_0$ is the magnitude of anisotropy. We introduce the following two variables,

$$v_n^{\mathrm{obs}} = \frac{x_n}{x_0} \tag{3.5}$$

$$\Psi_n = \frac{1}{n}\tan^{-1}(\frac{y_n}{x_n}), \quad 0 \le \Psi_n \le \frac{2\pi}{n} \tag{3.6}$$

From Eq. 3.5 and 3.6, measured azimuthal distribution $r^m(\phi)$ can be given by

$$r^m(\phi) = \frac{x_0}{2\pi}(1 + 2\sum_{n=1}^{\infty} v_n^{\mathrm{obs}}\cos(n[\phi_{\mathrm{lab}} - \Psi_n])) \tag{3.7}$$

Compare Eq. 3.4 and 3.7, one can see that Ψ_n gives event plane, which is the estimate of an azimuthal angle of true reaction plane. It is reconstructed from the reaction products event-by-event basis. The reconstructed plane (event plane) differs in general from the true reaction plane by an error $\Delta\Psi$, thus, the measured azimuthal angle of event plane Ψ_n is related to the true azimuthal angle of reaction plane Ψ by $\Psi_n = \Psi + \Delta\Psi$. Averaging over many events, one obtains the following relation between the measured and true Fourier coefficients:

$$\begin{aligned} v_n^{\mathrm{obs}} &= \langle\cos(n[\phi_{\mathrm{lab}} - \Psi_n])\rangle \\ &= \langle\cos(n[\phi_{\mathrm{lab}} - \Psi] - n[\Psi_n - \Psi])\rangle \\ &= \langle\cos(n[\phi_{\mathrm{lab}} - \Psi]) \cdot \cos(n\Delta\Psi)\rangle + \langle\sin(n[\phi_{\mathrm{lab}} - \Psi]) \cdot \sin(n\Delta\Psi)\rangle \\ &= \langle\cos(n[\phi_{\mathrm{lab}} - \Psi]) \cdot \cos(n\Delta\Psi)\rangle \\ &= v_n\langle\cos(n\Delta\Psi)\rangle \end{aligned} \tag{3.8}$$

from line 3 to 4, we assume that $\phi_{\mathrm{lab}} - \Psi$ and $\Delta\Psi$ are statistically independent. And we use the reflection symmetry of $\phi_{\mathrm{lab}} - \Psi$ and $\Delta\Psi$, i.e. average sine term vanish under that condition. This assumption is valid for the system with large multiplicity.

3.3.2 Event Plane Determination

Since an azimuthal angle of true reaction plane is unknown, we have to determine estimated reaction plane (event plane) experimentally. In this analysis, the Time Projection Chamber (TPC) and the Forward Forward Time Projection Chambers (FTPC) are used to determine an event plane for each event. Both the TPC and the FTPC have full azimuthal coverage. The FTPC cover pseudo-rapidity $2.5 < |\eta| < 4.0$. This rapidity gap helps to reduce non-flow contributions, which is the correlations not originated from the reaction plane, such as di-jet correlations, resonance decays, and Bose-Einstein correlations.

Event plane is calculated by the Eq. 3.9 - 3.11

$$Q_2 \cos(2\Psi_2) = X_2 = \sum_i w_i \cos(2\phi_i) \tag{3.9}$$

$$Q_2 \sin(2\Psi_2) = Y_2 = \sum_i w_i \sin(2\phi_i) \tag{3.10}$$

$$\Psi_2 = \left(\tan^{-1} \frac{\sum_i w_i \sin(2\phi_i)}{\sum_i w_i \cos(2\phi_i)} \right) /2 \tag{3.11}$$

where X_2 and Y_2 is the projection of event plane to x and y axes respectively. The sum goes over particles used in the event plane calculation, which is called flow tracks. The flow tracks selection criteria are list in Table 3.13, where the nHits means the number of the hits used for reconstruction of the tracks, nHits/nMax means the ratio of the number of fit hits to maximum possible hits. The w_i is weights. Usually the weights are assigned with the transverse momentum. This choice of weights is to make the event plane resolution the best by maximizing the flow contributions to the flow vector. Note that the event plane angle Ψ_2 is in the range $0 < \Psi_2 < \pi$.

Flow track selection criteria	
nHits	> 15
nHits/nMax	> 0.52
dca	< 2 cm
transverse momentum	$0.15 < p_T < 2.0$ GeV/c

Table 3.13: Selection criteria for flow tracks.

3.3.3 Flattening Event Plane Distribution

The azimuthal angle distribution of event plane should be Identical in all directions in the laboratory frame. Thus the event plane distribution has to be a flat distribution if the detectors have the ideal acceptance. In experiments, flattening the event plane procedure is necessary due to the acceptance effect. For event plane reconstructed from TPC tracks, ϕ weight, which is generated by inverting the ϕ distributions of detected tracks for a large event sample, is an effective method to flatten the distribution. The detector bias is removed by applying the ϕ weight at the ϕ of each track to that track. The ϕ weights are folded into the weight w_i in Equation 3.9 and 3.10.

Due to the serious loss of acceptance for FTPCs (the number of tracks detected by the best sector is about 6 times greater than the worst one), ϕ weight method is not enough to generate the flat event plane distribution. Thus, the shifting method [Bar97a] is applied to force the event plane distribution to be flat. The Equation 3.12 shows the formula for the shift correction. The average in Equation 3.12 goes over a large sample of events. In the analysis, the correction is done up to twentieth harmonic. The distributions of Ψ_2^{East} and Ψ_2^{West} are flatten separately and then the full-event plane distributions are flattened. Accordingly, the observed v_2 and resolution are calculated using the shifted (sub)event plane azimuthal angle.

$$\Psi' = \Psi + \sum_n \frac{1}{n}[-\langle\sin(2n\Psi)\rangle\cos(2n\Psi) + \langle\cos(2n\Psi)\rangle\sin(2n\Psi)] \tag{3.12}$$

Figure 3.6 shows the second harmonic event plane azimuthal distribution after shift corrections are applied. To show how flat it is, we do a constant fit to the event plane

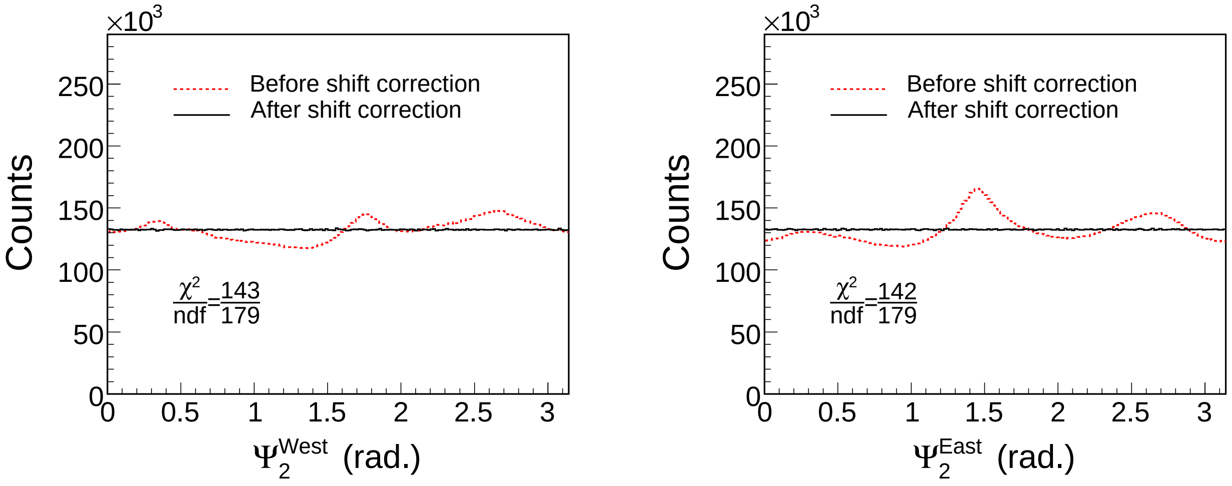

(a)

(b)

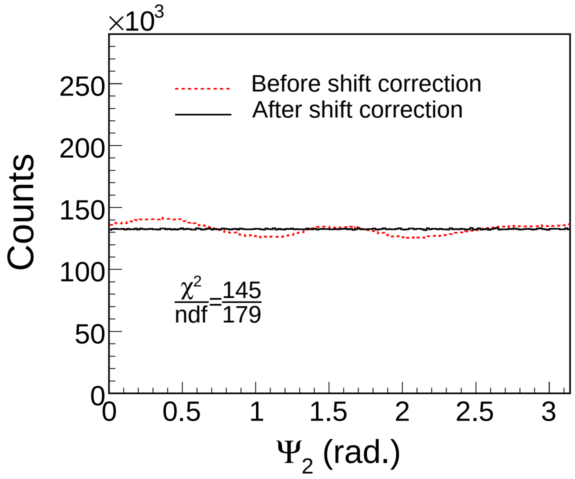

(c)

Figure 3.6: (a) Event plane reconstructed from west FTPC, (b) East FTPC, (c) West plus east FTPC, before and after shift correction. The χ^2 is for a fit to a constant.

azimuthal distribution. The χ^2/ndf is less than 1. As the event plane is flat, the acceptance effects will not bias the measurements of v_2.

3.3.4 Event Plane Resolution

According to Equation 3.8, the measured v_2 is equal to the value of v_2^{obs} divided by $\langle\cos(n\Delta\Psi)\rangle$. This can be understood as following: when we measure the reaction plane, due to finite flow particles and flow signal, there should be some uncertainties. It causes the difference between the measured reaction plane (event plane) and the real reaction plane. Thus, the observed v_2 should be corrected by the factor in Equation 3.8. [Vol98a]:

$$v_2 = \frac{v_2^{\mathrm{obs}}}{\langle\cos[2(\Psi_2 - \Psi_r)]\rangle} \tag{3.13}$$

The brackets in the denominator means the average over the all events. v_2, v_2^{obs} represent the real elliptic flow and the observed elliptic flow signal; while Ψ_2 and Ψ_r represent the measured azimuthal angle of reaction plane (event plane angle) and the azimuthal angle of real reaction plane. The denominator in the right side of the Equation, $\langle\cos[2(\Psi_2 - \Psi_r)]\rangle$ is the event plane resolution. As it is not measurable, we usually calculate the event plane resolution for sub events firstly. The steps are following: At first, a full event is divided in to two equal sub events; then one can measure the event plane angle in two sub events; The resolution for the sub event is defined by Equation 3.14 [Pos98a].

$$\langle\cos[2(\Psi_2^A - \Psi_r)]\rangle = \sqrt{\langle\cos[2(\Psi_2^A - \Psi_2^B)]\rangle} \tag{3.14}$$

Since we have two independent event plane from west and east FTPC (or the random sub events from TPC), we can estimate the event plane resolution by measuring the relative azimuthal angle $\Delta\Psi_2^{\mathrm{FTPC}} \equiv 2(\Psi_2^{\mathrm{West}} - \Psi_2^{\mathrm{East}})$. This is based on the assumption that there are no other correlations except flow effects. Taking into account that the multiplicity of the full event is twice as large as that of the sub-event, the full event plane resolution is given by Equation 3.15.

$$\langle\cos[2(\Psi_2 - \Psi_r)]\rangle \ = \ C\sqrt{\langle\cos[2(\Psi_2^A - \Psi_2^B)]\rangle} \tag{3.15}$$

In the case of low resolution (≤ 0.2), such as for the FTPC event plane, C approaches $\sqrt{2}$.

Centrality Bin	Resolution	Geometric Cross Section
1	0.112 ± 0.004	50 – 60%
2	0.138 ± 0.004	40 – 50%
3	0.163 ± 0.003	30 – 40%
4	0.180 ± 0.003	20 – 30%
5	0.175 ± 0.003	10 – 20%
6	0.147 ± 0.003	0 – 10%
	0.160 ± 0.001	0 – 60%

Table 3.14: Resolution for the FTPC event plane in Cu+Cu collisions at $\sqrt{s_{NN}} = 200$ GeV.

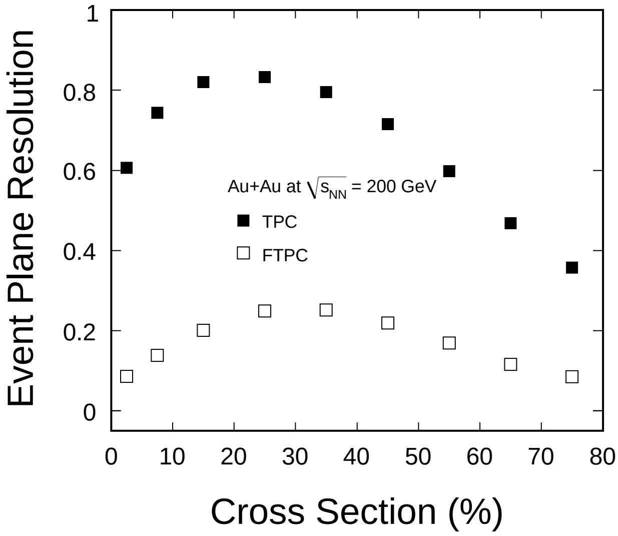

Figure 3.7: Resolution for the TPC and FTPC event plane in Au+Au collisions at $\sqrt{s_{NN}} =$ 200 GeV.

Table 3.14 shows the resolution for FTPC event plane in Cu+Cu collisions at $\sqrt{s_{NN}}$ = 200 GeV. The resolution depends on the number of tracks used and the magnitude of the event asymmetry. For the most peripheral collisions, the small multiplicity reduces the resolution while for the most central collisions, the small v_2 weakens it. As a consequence, the resolution reaches its maximum at the centrality of $20-30\%$ of the collision cross section. Figure 3.7 shows the resolution for the TPC and FTPC event plane in Au+Aucollisions at $\sqrt{s_{NN}}$ = 200 GeV, the TPC event plane resolution is greater than that of the FTPC by a factor of 4.

3.4 v_2 Methods

In this section, we discuss the methods to extract v_2.

3.4.1 The Event Plane Method

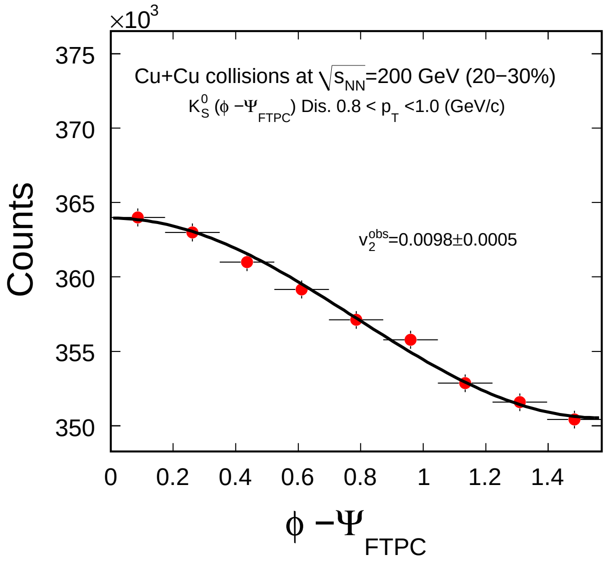

Figure 3.8: The distribution of $dN/d(\phi-\Psi_{\rm FTPC})$ for K^0_S at a chosen p_T bin (0.8 - 1.0 GeV/c) in Cu+Cu collisions at $\sqrt{s_{NN}}$ = 200 GeV. Black line shows the fit curve.

Fig. 3.8 shows the $dN/d(\phi-\Psi)$ distribution for K^0_S at a chosen p_T bin (0.8 - 1.0

GeV/c). The measured v_2 is extracted by fitting $dN/d(\phi - \Psi)$ distribution with Fourier expansion of azimuthal distribution:

$$\frac{dN}{d(\phi - \Psi)} = N(1 + 2v_2^{\mathrm{obs}} \cos(2(\phi - \Psi_2))) \tag{3.16}$$

Where N and v_2^{obs} are free parameters. The measured v_2, i.e. v_2^{obs}, need to be corrected with event plane resolution by Eq. 3.13.

3.4.2 The Scalar Product Method

The Scalar Product method [Adl02b, Ada05c] is similar to the Event Plane method, and gives v_2 as:

$$v_2(p_T) \quad = \frac{\langle Q_2 u_{2,i}^*(p_T)\rangle}{2\sqrt{\langle Q_2^A Q_2^{B*}\rangle}} \tag{3.17}$$

where $u_{2,i} = \cos(2\phi_i) + i\sin(2\phi_i)$ is a unit vector of the ith particle, $Q_2 = \sum_k u_{2,k}$ is the flow vector with the sum running over all other particles k in the event. The superscript * denotes the complex conjugate of a complex number. A and B denote the two subevents. In the case that Q_2 is normalized to a unit vector, Eq. (3.17) reduces to the Event Plane method. In the Scalar Product method, one can use a different (re-centering) technique [Sel08a] to correct for detector effects, which presents an alternative to the weighting and shifting procedures. The Scalar Product method is applied to the v_2 measurement of charged hadrons.

3.4.3 The v_2 versus m_{inv} Method

When we measure v_2 of the reconstructed particles, such as K_S^0, Λ, Ξ and Ω, v_2 versus m_{inv} method is often use. In Fig. 3.5, it shows the invariant mass distributions for these particles. Even with the optimized topology cuts, there are still some residual combinatorial backgrounds. The v_2 versus m_{inv} method is designed for extracting the v_2 of real signal.

The equation in the following illustrates the v_2 versus m_{inv} method:

$$v_2^{\text{Sig+Bg}}(m_{\text{inv}}) = v_2^{\text{Sig}} \frac{\text{Sig}}{\text{Sig} + \text{Bg}}(m_{\text{inv}}) + v_2^{\text{Bg}}(m_{\text{inv}}) \frac{\text{Bg}}{\text{Sig} + \text{Bg}}(m_{\text{inv}}) \tag{3.18}$$

Based on the invariant mass distribution of the reconstructed particle, we can get the total candidates (signals plus backgrounds) as a function of invariant mass. With estimating the backgrounds as a function of invariant mass, we can get the the ratio of signals over total candidates and the ratio of backgrounds over total candidates as a function of invariant mass. Assuming a certain function form for the v_2 of backgrounds as a function of invariant mass, we can finally extract the v_2 of signals as a function of invariant mass by fitting the data of the v_2 of total candidates to the Equation 3.18.

As an example, Figure 3.9 shows how the v_2 versus m_{inv} method works for $K_S^0(1.4 < p_T < 1.6$ GeV) in Au+Au collisions at $\sqrt{s_{NN}} = 200$ GeV. In panel (a), the solid curve stands for the estimate of backgrounds by a fit of the 4th order polynomial function. Based on the invariant mass distribution and estimated backgrounds, we can get $\frac{\text{Bg}}{\text{Sig+Bg}}$ and $\frac{\text{Sig}}{\text{Sig+Bg}}$ as a function of invariant mass. In panel (b), The data points (open circles) stands of the v_2 if all candidates of K_S^0, while the solid curve is the fit to the data with Equation 3.18. In order to understand this method profoundly, we show the v_2 contributions from the signals (blue curve) and combinatorial backgrounds (red curve) together with the fit to the total v_2 of candidates (solid curve) as a function of invariant mass in panel (c).

The contribution of backgrounds could be well constrained by utilizing this method. As we can see in the invariant mass plot, the ratio of backgrounds over total candidates are equal to unity in the left and right side of the distribution. It means all these data point are contributions from backgrounds. This provides good constraints to the v_2 of backgrounds when we applying the fit to the data. The most important part of systematic uncertainty in this method comes from estimate of the backgrounds. Estimating the background by different functions can help us to understand the systematic uncertainty. We will discuss it in detail in the section of systematic uncertainties.

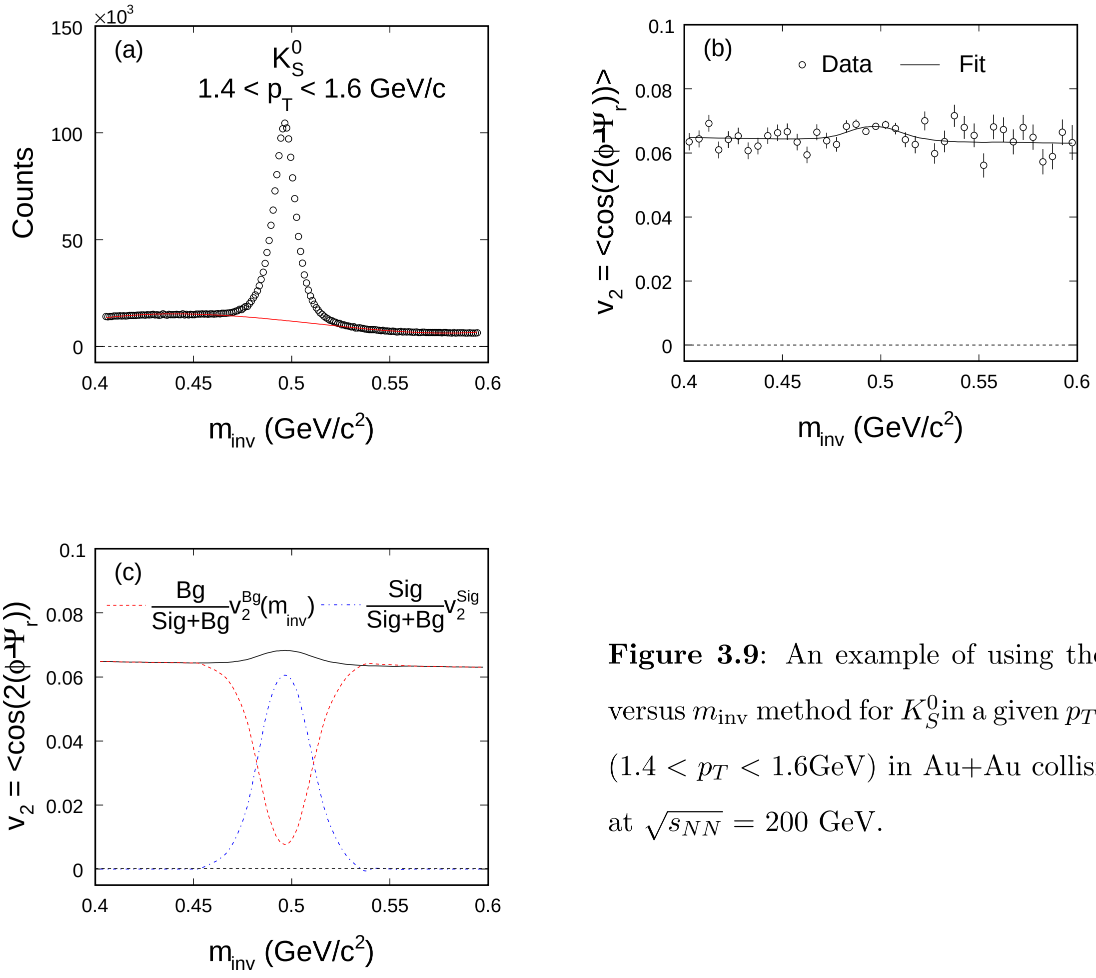

Figure 3.9: An example of using the v_2 versus m_{inv} method for K_S^0in a given p_T bin $(1.4 < p_T < 1.6\text{GeV})$ in Au+Au collisions at $\sqrt{s_{NN}} = 200$ GeV.

3.5 Systematic Uncertainties

3.5.1 Systematic Error on the FTPC Event Plane

The systematic uncertainties in v_2 analysis procedures are studied. We estimate the systematic errors from shifting of the FTPC event plane by comparing v_2 using different maximum harmonic in Eq. (3.12). The systematic errors from the flattening process are less than 1%.

3.5.2 Systematic Error on Reconstruction of Strange Hadrons

The systematic errors in K_S^0 and Λ v_2 measurement from background uncertainty, combining centrality and cut criteria are estimated using Event Plane method. The background uncertainty is estimated by fitting the background with second and fourth order polynomial. The systematic uncertainty from cut criteria is estimated by varying cuts with reasonable values.

The systematic errors on K_S^0 and Λ from background and cut criteria are summarized in Table 3.15.

	K_S^0		Λ	
Centrality	Background	Cut criteria	Background	Cut criteria
$0-60\%$	1%	2%	1%	2%
$0-20\%$	1%	2%	1%	4%
$20-60\%$	4%	1%	5%	1%

Table 3.15: Summary of systematic error of v_2 on reconstruction of strange hadrons in Cu+Cu collisions at $\sqrt{s_{NN}} = 200$ GeV.

3.5.3 Systematic Error on Non-flow Effect

The method of determining v_2 using cumulants of various orders has been shown to eliminate non-flow correlations. However, the method is useful only for large values of flow and multiplicity. For the relatively low values of flow and multiplicity seen in Cu+Cu collision, the non-flow correlations have been estimated, as described below.

The Event Plane method with the TPC event plane is sensitive to non-flow effects. Particles of interest tend to correlate with particles used in the flow vector calculation due to short-range non-flow correlations. Also, particles of two random sub-events tend to have those correlations. Thus, non-flow exists in both the observed v_2 (the numerator of Eq. (3.13)) and the resolution (Eq. (3.15)). To reduce non-flow effects due to short-range correlations, we take advantage of the large η gap between the two FTPCs sitting at the two sides of the collision in the forward regions. Non-flow is reduced by the η gap between the TPC and FTPCs, but this may not be large enough to remove all non-flow correlations. Thus, we investigate these effects by comparing the azimuthal correlations measured in Cu+Cu to those in p+p collisions, where all correlations are assumed to be of non-flow origin [Ada04b]. Taking into account the non-flow contribution, the numerator of Eq. (3.17) can be written as follows [Ada04b, Adl02b]:

$$\langle\sum_i \cos[2(\phi_{p_T} - \phi_i)]\rangle \;=\; M v_2(p_T)\overline{v_2} \;+\; \text{nonflow} \tag{3.19}$$

where ϕ_{p_T} is the azimuthal angle of particles from a given p_T bin ($u^*_{2,i}$ in Eq. (3.17)) and the sum goes over all tracks k in an event used to determine the flow vector (Q_2 in Eq. (3.17)). The angled brackets denote averaging over the events. The first term in the right-hand side of Eq. (3.19) represents the contribution from elliptic flow. $v_2(p_T)$ is the value of elliptic flow at a given p_T. $\overline{v_2}$ is the elliptic flow on average for all particles used in the sum of Eq. (3.19). The multiplicity of particles contributing to the sum is denoted by M. All other correlations subject to non-flow go to the second term in the right-hand side of Eq. (3.19). It is assumed that the quantity $\langle Q_2 u^*_{2,i}(p_T)\rangle$ in p+p collisions can be used to estimate the non-flow in AA collisions [Ada04b, Ada05c].

$$M v_2(p_T)\overline{v_2} \;= \langle Q_2 u^*_{2,i}(p_T)\rangle_{AA} - \;\langle Q_2 u^*_{2,i}(p_T)\rangle_{pp} \tag{3.20}$$

Dividing both sides by $2\sqrt{\langle Q_2^A Q_2^{B*}\rangle_{AA}}$ as in Eq. (3.17) gives

$$v_2\{AA - pp\}(p_T) \;=\; \frac{\langle Q_2 u^*_{2,i}(p_T)\rangle_{AA} - \langle Q_2 u^*_{2,i}(p_T)\rangle_{pp}}{2\sqrt{\langle Q_2^A Q_2^{B*}\rangle_{AA}}} \tag{3.21}$$

because $2\sqrt{\langle Q_2^A Q_2^{B*}\rangle_{AA}} = 2\sqrt{(M/2)\overline{v_2}(M/2)\overline{v_2}} = M\overline{v_2}$.

Comparing p+p and AA collisions, one might expect some changes in particle correlations: there could be an increase in correlations due to a possible increase of jet multiplicities in AA collisions or, conversely, some decrease due to the suppression of high p_T back-to-back correlations [Adl03a]. It is difficult to make an accurate estimate of the possible uncertainties. The fact that at high p_T ($p_T > 5$ GeV/c) the p+p results are very close to central Au+Au [Ada04b, Ada05c] suggests that the uncertainties are relatively small. In the following, we use $v_2\{AA-pp, \mathrm{TPC}\}$ and $v_2\{AA-pp, \mathrm{FTPC}\}$ to denote $v_2\{AA-pp\}$ calculated with TPC and FTPC flow vectors, respectively.

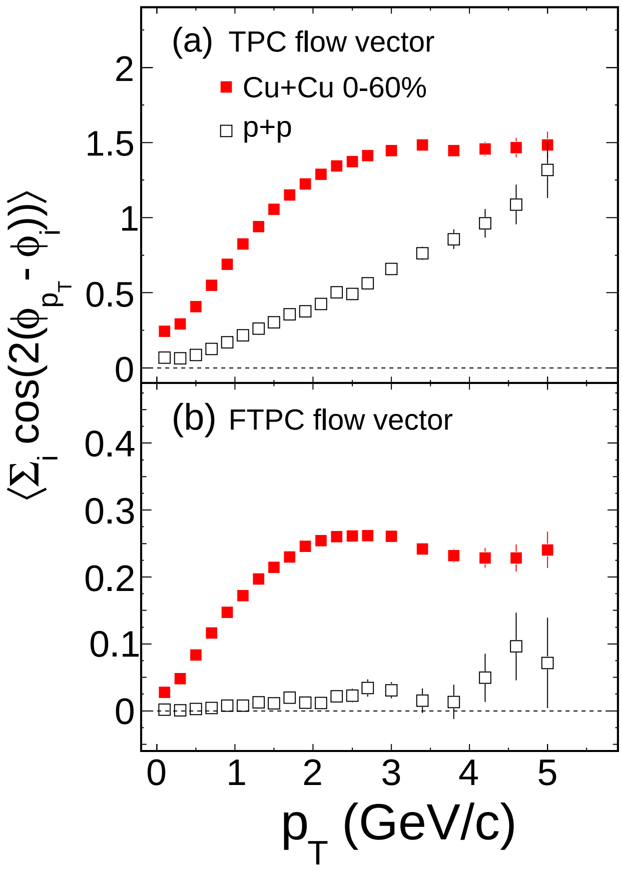

Figure 3.10: Charged hadron azimuthal correlations as a function of p_T in $\sqrt{s_{NN}} = 200$ GeV 60% most central Cu+Cu collisions (closed squares) compared to those from $\sqrt{s_{NN}} = 200$ GeV p+p collisions (open squares). Flow vector calculated from (a) TPC tracks, (b) FTPC tracks.

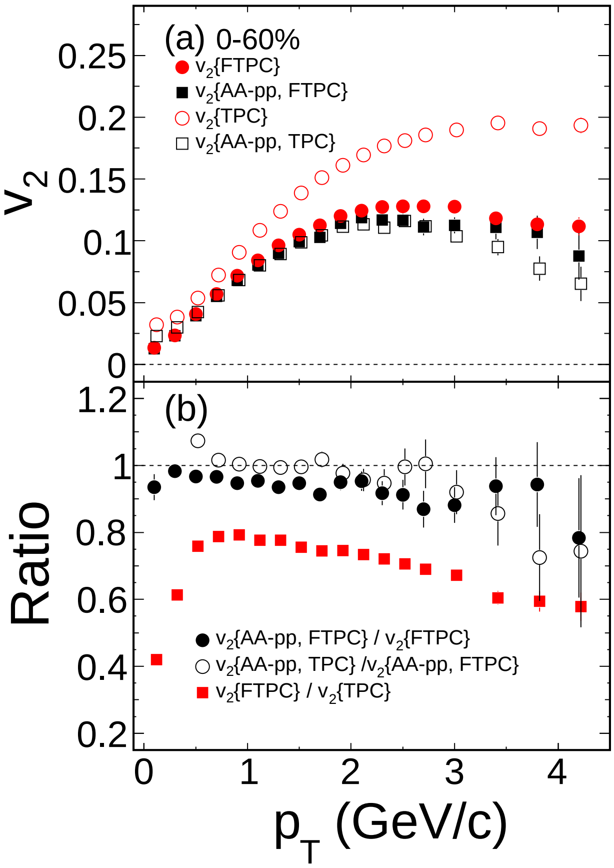

Figure 3.11: (a) Charged hadron $v_2(p_T)$ in $\sqrt{s_{NN}} = 200$ GeV 0−60% Cu+Cu collisions. Open circles, closed circles, open squares and closed squares represent the results of v_2 as a function of p_T measured by the TPC flow vector ($v_2\{\mathrm{TPC}\}$), the FTPC flow vector ($v_2\{\mathrm{FTPC}\}$), the TPC and FTPC flow vector with subtracting the azimuthal correlations in p+p collisions ($v_2\{AA-pp, \mathrm{TPC}\}$, $v_2\{AA-pp, \mathrm{FTPC}\}$). (b) The ratio of the results for the various methods described in (a).

Non-flow is one of the largest uncertainties in elliptic flow measurements. As we mentioned above, this effect can be investigated by comparing the azimuthal correlations measured in Cu+Cu collisions to those in p+p collisions. The event average of the sum of the correlations is given by Eq. (3.19).

Figure 3.10 shows the azimuthal correlation, Eq. (3.19), as a function of p_T for the $0-60\%$ centrality range in Cu+Cu collisions at $\sqrt{s_{NN}}$ = 200 GeV, compared to p+p collisions. As we can see, the azimuthal correlations in Cu+Cu collisions, shown as solid squares, increase with p_T and then saturate above 2 GeV/c while those in p+p collisions, shown as open squares, monotonically increase with p_T in the case of the TPC flow vector. With the flow vector determined from FTPC tracks the azimuthal correlations around midrapidity in p+p collisions are small when p_T is less than 4 GeV/c. It means that one strongly reduces the non-flow effects with the FTPC flow vector relative to the one seen with the TPC flow vector.

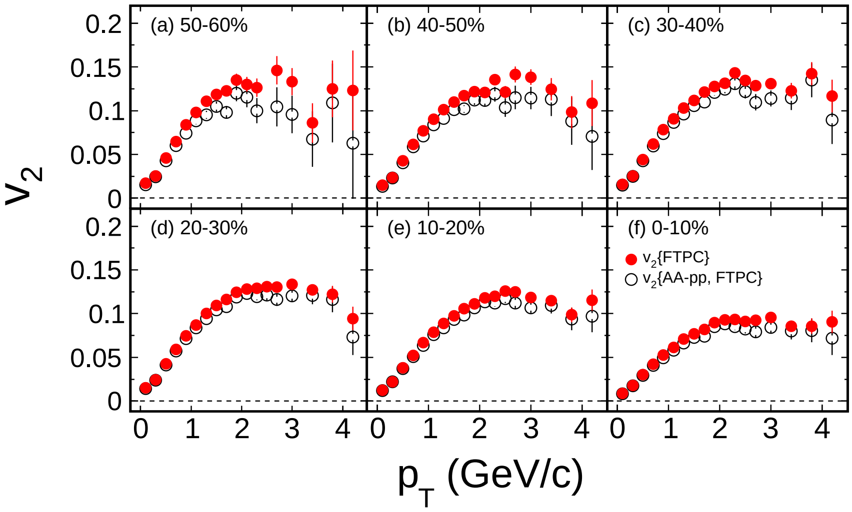

Figure 3.12: Charged hadron v_2\{FTPC\} (closed circles) and $v_2\{AA-pp,\text{FTPC}\}$ (open circles) as a function of p_T in $\sqrt{s_{NN}}$ = 200 GeV Cu+Cu collisions for centrality bins: (a) $50-60\%$, (b) $40-50\%$, (c) $30-40\%$, (d) $20-30\%$, (e) $10-20\%$ and (f) $0-10\%$. The percentages refer to fraction of most central events.

In order to illustrate the sensitivity to non-flow for the various flow analysis methods, we first analyzed $h^{\pm}$ elliptic flow in the 60% most central Cu+Cu collisions at $\sqrt{s_{NN}}$ = 200 GeV. As shown in Fig. 3.11 (a), the fact that v_2\{TPC\} is significantly

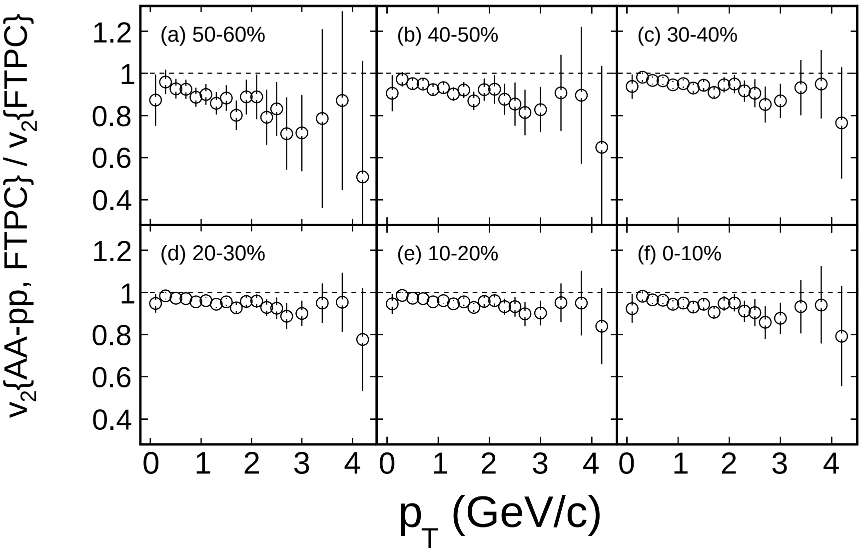

Figure 3.13: Ratios of $v_2\{AA-pp,\text{FTPC}\}/v_2\{\text{FTPC}\}$ for charged hadron as a function of p_T in $\sqrt{s_{NN}}=200$ GeV Cu+Cu collisions for centrality bins: (a) $50-60\%$, (b) $40-50\%$, (c) $30-40\%$, (d) $20-30\%$, (e) $10-20\%$ and (f) $0-10\%$. The percentages refer to fraction of most central events.

larger than $v_2\{\text{FTPC}\}$ indicates a larger non-flow effect in $v_2\{\text{TPC}\}$. With the large η gap between West and East FTPCs, non-flow effects due to the short-range correlations are reduced in $v_2\{\text{FTPC}\}$. $v_2\{\text{FTPC}\}$ saturates at $p_T\sim 2.5$ GeV/c and then falls off slightly up to $p_T\sim 4$ GeV/c. In order to estimate the remaining non-flow effects in $v_2\{\text{FTPC}\}$, we subtract the azimuthal correlations of p+p collisions from those in Cu+Cu collisions according to Eq. (3.21). In Fig. 3.11 (a), $v_2\{AA-pp,\text{FTPC}\}$ is close to $v_2\{\text{FTPC}\}$ in the region $p_T<4$ GeV/c. To quantitatively illustrate non-flow systematic uncertainties, Fig. 3.11 (b) shows the ratios of $v_2\{AA-pp,\text{FTPC}\}$ to $v_2\{\text{FTPC}\}$, $v_2\{AA-pp,\text{TPC}\}$ to $v_2\{AA-pp,\text{FTPC}\}$ and $v_2\{\text{FTPC}\}$ to $v_2\{\text{TPC}\}$ as a function of p_T. $v_2\{\text{FTPC}\}/v_2\{\text{TPC}\}$ shows that non-flow in $v_2\{\text{TPC}\}$ increases from 20% at $p_T\sim 0.8$ GeV/c to 40% at $p_T\sim 3.5$ GeV/c. Based on the comparison between $v_2\{AA-pp,\text{FTPC}\}$ and $v_2\{\text{FTPC}\}$, the residual non-flow in $v_2\{\text{FTPC}\}$ is less than 10% below $p_T\sim 4$ GeV/c. We also checked the $v_2\{AA-pp\}$ calculated with the TPC flow vector. Beyond $p_T\sim 3$ GeV/c, $v_2\{AA-pp,\text{TPC}\}$ seems systematically lower, but within errors it is similar to $v_2\{AA-pp,\text{FTPC}\}$. This shows that most of the non-flow is eliminated by subtracting the azimuthal correlation in p+p collisions, validating our earlier assumption.

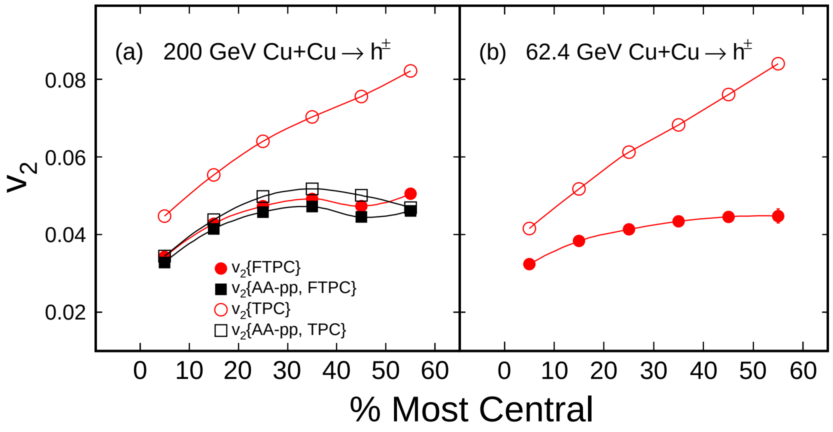

Figure 3.14: Charged hadron v_2 integrated over p_T and η vs. centrality for the various methods described in the text in $\sqrt{s_{NN}} = 200$ GeV and 62.4 GeV Cu+Cu collisions.

To illustrate the centrality dependence of the systematic uncertainties, Fig. 3.12 shows $v_2\{\text{FTPC}\}$ and $v_2\{AA - pp, \text{FTPC}\}$ as a function of p_T for six centrality bins. Ratios of $v_2\{AA - pp, \text{FTPC}\}$ to $v_2\{\text{FTPC}\}$ for each centrality bin are shown in Fig. 3.13 from (a) the most peripheral bin $50 - 60\%$ to (f) the most central bin $0 - 10\%$. For each centrality bin, the ratio falls off slightly as p_T increases. For the two peripheral bins $50 - 60\%$ and $40 - 50\%$, the ratios drop faster than in the other bins, indicating larger non-flow contributions in $v_2\{\text{FTPC}\}(p_T)$ in peripheral Cu+Cu collisions. Figure 3.14 shows charged hadron v_2 integrated over p_T ($0.15 < p_T < 4$ GeV/c) and η ($|\eta| < 1.0$) vs. centrality for the various methods. It is clear that $v_2\{\text{TPC}\}$ is much higher than for the other methods, especially for the peripheral collisions.

To summarize the non-flow systematics we employed the Scalar Product method with TPC and FTPC flow vectors for $h^{\pm}$ in Cu+Cu collisions at $\sqrt{s_{NN}} = 200$ GeV. The results for the 60% most central events are shown in Fig. 3.11. $v_2\{\text{TPC}\}$ has large non-flow contributions while $v_2\{\text{FTPC}\}$ eliminates most of the non-flow. In what follows, we will report our results in term of $v_2\{\text{FTPC}\}$. For simplicity v_2 denotes $v_2\{\text{FTPC}\}$

except when the flow method is explicitly specified. With the assumption of pure non-flow effects in p+p collisions, we use $v_2\{AA-pp, \mathrm{FTPC}\}$ to estimate non-flow systematic errors in $v_2\{\mathrm{FTPC}\}$. Ratios of $v_2\{AA-pp, \mathrm{FTPC}\}$ to $v_2\{\mathrm{FTPC}\}$ are shown for the 60% most central events in Fig. 3.11 (b) and six centrality bins in Fig. 3.13. The ratios show that non-flow effects increase with p_T for all centrality bins and non-flow effects are larger in more peripheral bins. The non-flow systematic error is 5% for $0-40\%$ collisions and 10% for $40-60\%$ collisions. For K_S^0, ϕ, Λ and Ξ v_2, we assume a similar magnitude of non-flow contributions.

The non-flow systematic uncertainty for strange hadron in Au+Au collisions at $\sqrt{s_{NN}}$ = 200 GeV has been discussed in [Abe08a]. The systematic errors between Event Plane method (the TPC event plane) and Lee-Yang Zero method are in order of 10%. Also, for simplicity v_2 denotes $v_2\{\mathrm{TPC}\}$ in Au+Au collisions except when the flow method is explicitly specified.

CHAPTER 4

Results

In this chapter, we present the measurements of v_2 at mid-rapidity $|Y| < 1$ ($|\eta| < 1$ for charged hadrons) from Cu+Cu and Au+Au collisions. v_2 results are presented for strange hadrons (K_S^0, Λ and Ξ) in Cu+Cu collisions at $\sqrt{s_{NN}} = 200$ GeV, for charged hadrons in Cu+Cu collisions at $\sqrt{s_{NN}} = 200$ and 62.4 GeV, for π, p, K_S^0, Λ, ϕ, Ξ and Ω in Au+Au collisions at $\sqrt{s_{NN}} = 200$ GeV, for charged hadrons in Au+Au collisions at $\sqrt{s_{NN}} = 9.2$ GeV.

4.1 Transverse Momentum Dependence of v_2 in Mini-bias Events

Figure 4.1 shows minimum bias v_2 for K_S^0, Λ and Ξ at mid-rapidity $|Y| < 1$ ($|\eta| < 1$ for charged hadrons) in Cu+Cu collisions at $\sqrt{s_{NN}} = 200$ GeV. The circles, squares, upper triangles and lower triangles represent K_S^0, Λ, Ξ and charged hadrons, respectively. The error bars are statistical errors. The strange hadrons v_2 is measured up to $p_T \sim 4$ GeV/c. Strange hadrons and charged hadrons v_2 increase with p_T and then saturate at higher p_T. At low p_T ($p_T < 1.5$ GeV/c), the heavier Λ has smaller v_2 than the lighter K_S^0. At intermediate p_T ($2 < p_T < 4$ GeV/c), Λ v_2 is greater than K_S^0.

Figure 4.2 shows minimum bias v_2 for π, p, K_S^0, Λ, ϕ, Ξ and Ω at mid-rapidity $|Y| < 1$ in Au+Au collisions at $\sqrt{s_{NN}} = 200$ GeV. A clear mass ordering can be seen when $p_T < 2$ GeV/c. Beyond this p_T region ($p_T > 2$ GeV/c), all particles are grouped according to hadron type (baryon or meson), and the v_2 of baryon group is greater than that of meson.

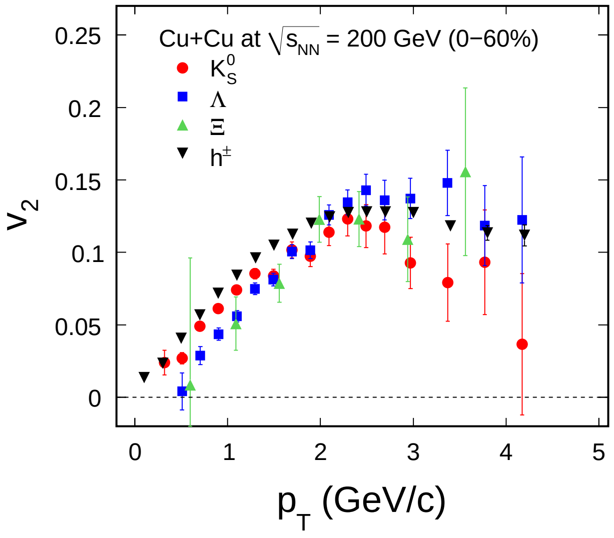

Figure 4.1: Elliptic flow (v_2) as a function of transverse momentum (p_T) at mid-rapidity $|Y| < 1$ ($|\eta| < 1$ for charged hadrons) for minimum bias ($0 - 60\%$ geometrical cross section) in Cu+Cu collisions at $\sqrt{s_{NN}}$ = 200 GeV. The error bars are statistical errors.

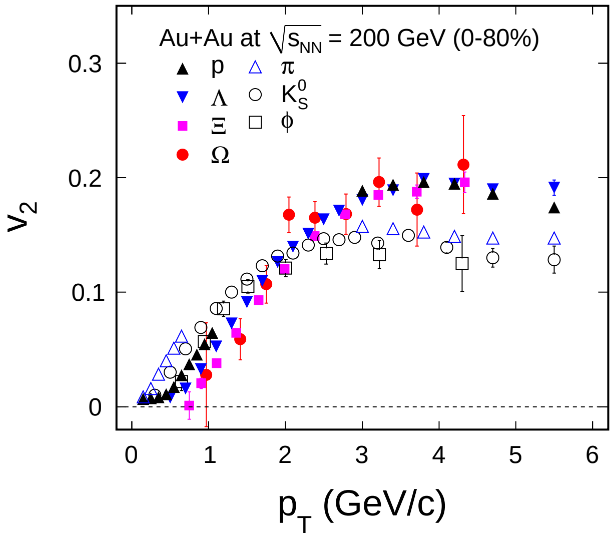

Figure 4.2: Elliptic flow (v_2) as a function of transverse momentum (p_T) at mid-rapidity $|Y| < 1$ for minimum bias ($0 - 80\%$ geometrical cross section) in Au+Au collisions at $\sqrt{s_{NN}}$ = 200 GeV. The error bars are statistical errors.

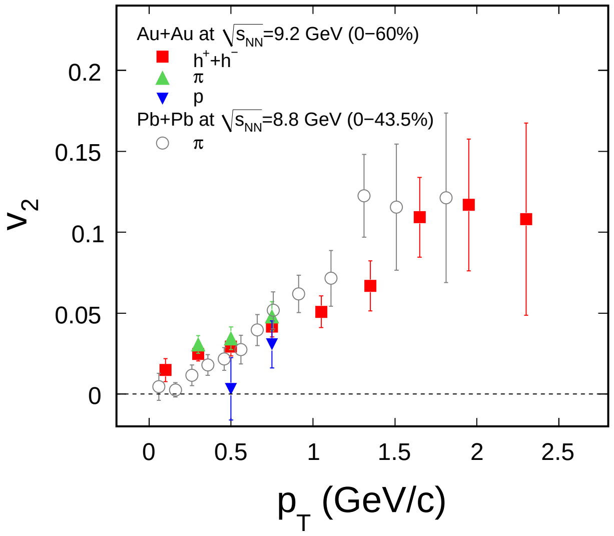

Figure 4.3: Elliptic flow (v_2) as a function of transverse momentum (p_T) at mid-rapidity $|Y| < 1$ ($|\eta| < 1$ for charged hadrons) for minimum bias ($0 - 60\%$ geometrical cross section) in Au+Au collisions at $\sqrt{s_{NN}} = 9.2$ GeV. For comparison, v_2 (p_T) results for π (open circles) from NA49 [Alt03a] in $0 - 43.5\%$ Pb+Pb collisions at $\sqrt{s_{NN}} = 8.8$ GeV, are also shown. The error bars are statistical errors.

With 3 k events collected using STAR detector from a test run of the collider in the year 2008, we present the results of an elliptic flow analysis of Au+Au collisions at $\sqrt{s_{NN}}$ = 9.2 GeV. Figure 4.3 shows minimum bias v_2 for π, p and charged hadrons at mid-rapidity $|Y| < 1$ ($|\eta| < 1$ for charged hadrons). Within error bars, it is consistent with the results of NA49 at the similar beam energy and system size. It indicates the capabilities of the STAR detector to pursue the proposed beam energy scan [Abe10a].

4.2 Centrality Dependence of v_2

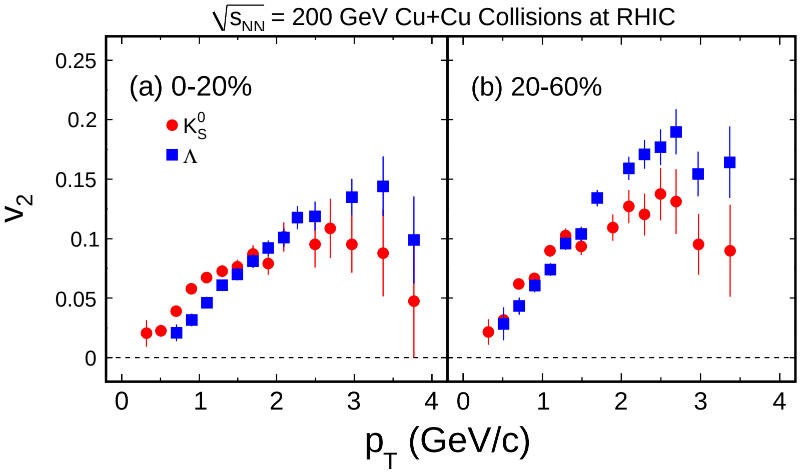

Figure 4.4: v_2 of K_S^0 and Λ as a function of p_T for $0 - 20\%$ and $20 - 60\%$ centrality bins in Cu+Cu collisions at $\sqrt{s_{NN}}$ = 200 GeV.

Figure 4.4 shows v_2 of K_S^0 and Λ as a function of p_T at mid-rapidity for Cu+Cu collisions at $\sqrt{s_{NN}}$ = 200 GeV for (a) $0 - 20\%$ and (b) $20 - 60\%$. Symbols and errors are presented in the same way as minimum bias data in Figure 4.1. The p_T dependence of v_2 is similar in these two centrality bins: v_2 increases at low p_T, and then saturates at intermediate p_T. The mass ordering ($p_T < 2$ GeV/c) and the hadron type dependence ($p_T > 2$ GeV/c) can be observed. The values of v_2 in peripheral collisions is larger than that in central collisions.

Centrality dependence of $v_2(p_T)$ for charged hadrons in Cu+Cu collisions at $\sqrt{s_{NN}}$ =

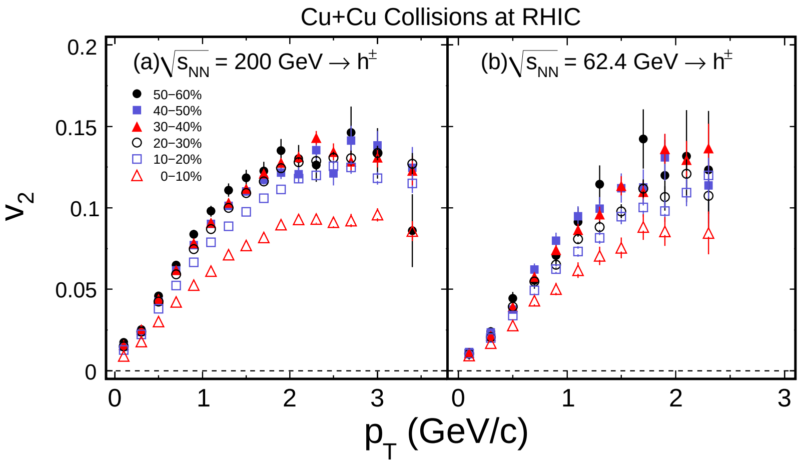

Figure 4.5: Charged hadron v_2 as function of p_T for $50 - 60\%$ (solid circles), $40 - 50\%$ (solid squares), $30 - 40\%$ (solid triangles), $20 - 30\%$ (open circles), $10 - 20\%$ (open squares) and $0 - 10\%$ (open triangles) in $\sqrt{s_{NN}} = 200$ GeV and 62.4 GeV Cu+Cu collisions.

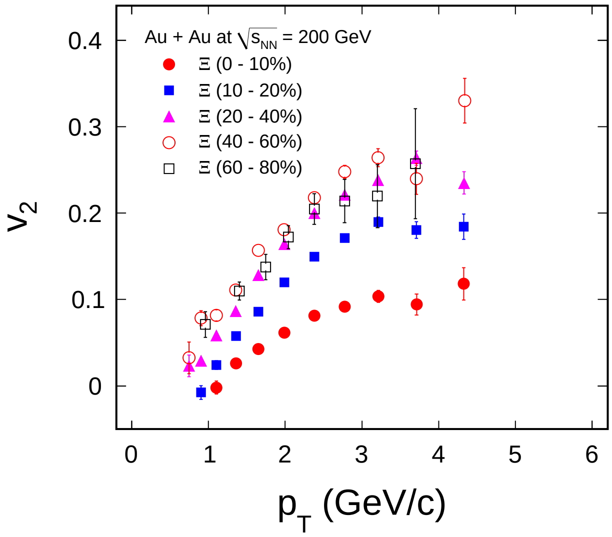

Figure 4.6: Ξ v_2 as function of p_T for $60 - 80\%$, $40 - 60\%$, $20 - 40\%$, $10 - 20\%$, and $0 - 10\%$ in $\sqrt{s_{NN}} = 200$ GeV Au+Au collisions.

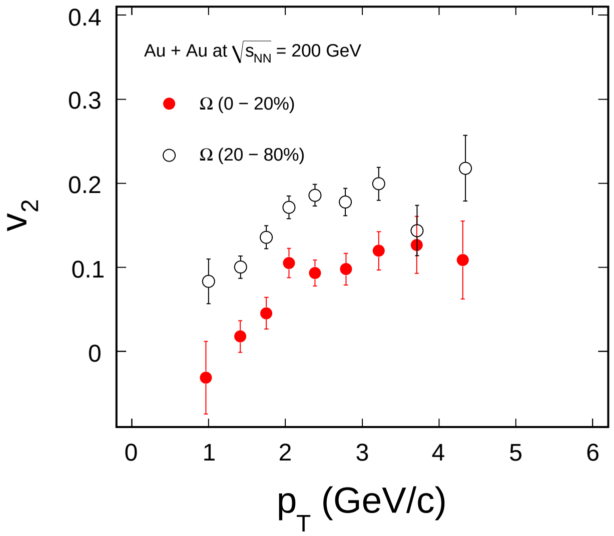

Figure 4.7: Ω v_2 as function of p_T for $20-80\%$ and $0-20\%$ in $\sqrt{s_{NN}}$ = 200 GeV Au+Au collisions.

200 GeV and 62.4 GeV are shown in Figure 4.5. The observed trend is that v_2 increases with p_T, reaches its maximum and then slightly decreases. The magnitude of v_2 increase from central to peripheral collisions.

With the large statistics in run VII, we can measured the v_2 for multi-strange hadron much more precisely. Figure 4.6 to 4.7 show the centrality dependence of $v_2(p_T)$ for $\Xi^- + \overline{\Xi}^+$ and Ω in Au+Au collisions at $\sqrt{s_{NN}}$ = 200 GeV. We divide all events into five centrality intervals for $\Xi^- + \overline{\Xi}^+$, from the top 10% to $60-80\%$ peripheral collisions. For Ω, the results are from $0-20\%$ and $20-80\%$ centrality bins. The magnitude of v_2 is smaller in the more central collisions, which is similar to the results of charge hadrons [Bai07a].

4.3 p_T-integrated v_2 for Strange Hadron

Average v_2 over measured p_T range, which we denote $\langle v_2 \rangle$ are calculated as

$$\langle v_2 \rangle = \frac{\int_0^\infty dp_T dN/dp_T \times v_2(p_T)}{\int_0^\infty dp_T dN/dp_T} = \frac{\sum_i dN^i/dp_T \times v_2^i(p_T)}{\sum_i dN^i/dp_T} \tag{4.1}$$

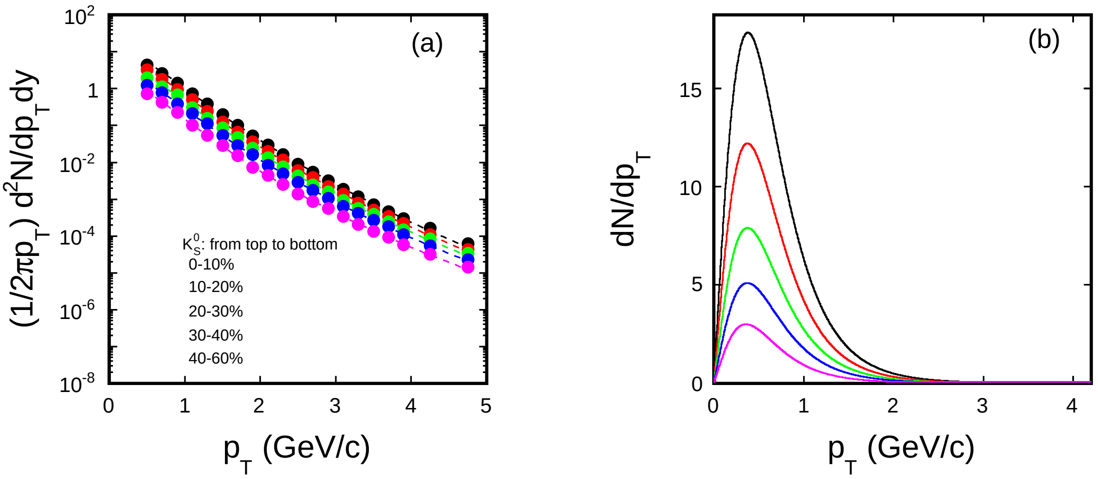

Figure 4.8: The p_T spectra and dN/dp_T distribution for K_S^0 from central (top) to peripheral (bottom) collisions. Dashed lines in panel (a) represent fitting results by Eq. 4.2. The curves in panel (b) have been scaled for clarity.

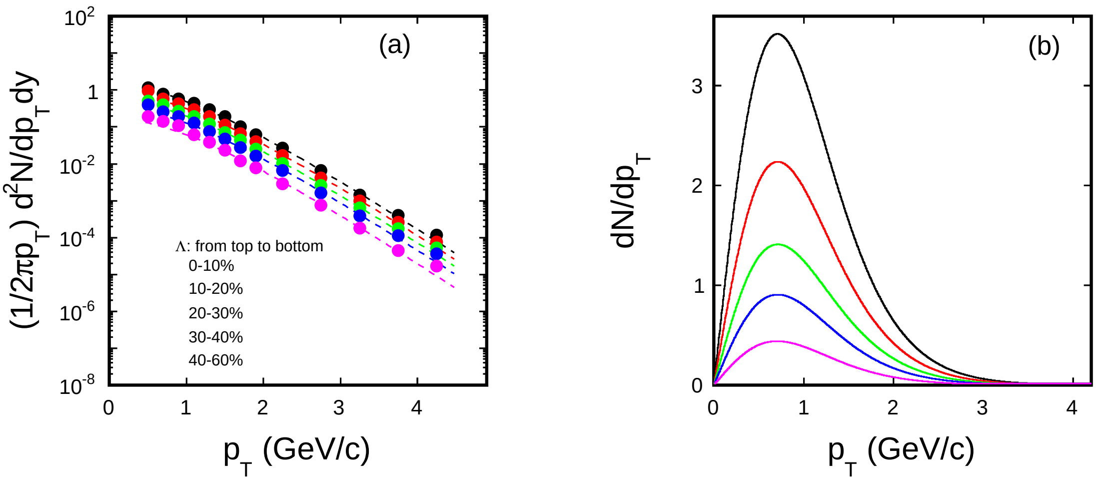

Figure 4.9: The p_T spectra and dN/dp_T distribution for Λ from central (top) to peripheral (bottom) collisions. Dashed lines in panel (a) represent fitting results by Eq. 4.3. The curves in panel (b) have been scaled for clarity.

Where dN/dp_T is the transverse momentum distributions, and $v_2(p_T)$ is the differential v_2 as a function of p_T. Since we measure both spectra and v_2 in the limited p_T, the integral in Eq. 4.1 are replaced to the sum of data points in the third term, We estimate v_2 and dN/dp_T for lower p_T range by extrapolating the fitting results to $p_T \to 0$. Higher p_T range are also extrapolated for both v_2 and dN/dp_T but they do not contribute the $\langle v_2 \rangle$ for all particle species, thus we just integrate the results up to the maximum of measured p_T.

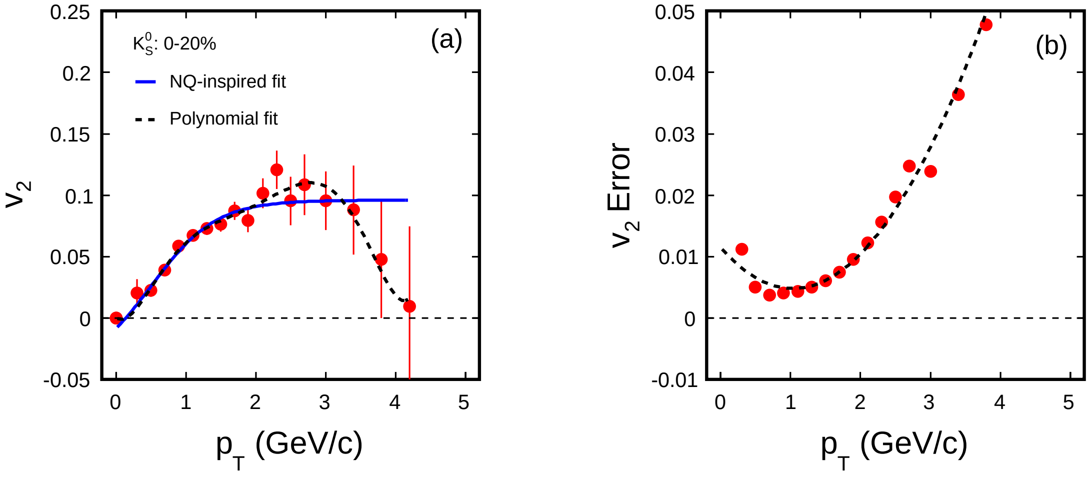

Figure 4.10: $v_2(p_T)$ for K_S^0 in $0-20\%$ centrality bin. (a) Fitting results for $v_2(p_T)$ by polynomial and Eq. 4.4, (b) A polynomial fit to v_2 errors.

Fig. 4.8 - 4.9 show transverse momentum spectra for K_S^0 and Λ as a function of centrality. We parameterize the p_T spectra by the following functions:

$$f^{K_S^0}(p_T) = A \cdot (1 + \frac{\sqrt{p_T^2 + m_0^2} - m_0}{nT})^{-n} \tag{4.2}$$

$$f^{\Lambda} = A \cdot \sqrt{p_T^2 + m_0^2} \cdot e^{-\frac{\sqrt{p_T^2+m_0^2}-m_0}{T}} \tag{4.3}$$

Where A, n, T are the free parameters.

Fig. 4.10 - 4.11 show the fitting results of $v_2(K_S^0)$ and $v_2(\Lambda)$ as a function of p_T for $0-20\%$ centrality bin. To extrapolate the data to low and high p_T, we use polynomials

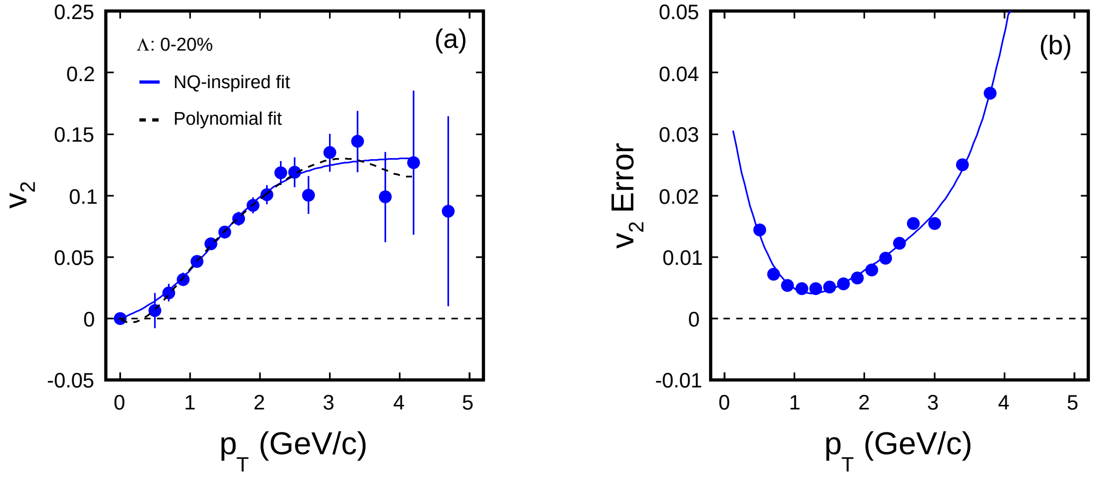

Figure 4.11: $v_2(p_T)$ for Λ in $0-20\%$ centrality bin. (a) Fitting results for $v_2(p_T)$ by polynomial and Eq. 4.4, (b) A polynomial fit to v_2 errors.

and Eq. 4.4

$$f_{v_2}(n) = \frac{an}{1+e^{-(p_T/n-b)/c}} - dn \tag{4.4}$$

The errors of v_2 are fitted by polynomials. The fit from Eq. 4.4 (n_q-inspired fit) is used for value, and the difference of $\langle v_2 \rangle$ obtained with n_q-inspired fit and polynomial fit is quoted as systematic error.

	K_S^0			Λ		
Centrality	$\langle v_2 \rangle$	Stat. error	Sys. error	$\langle v_2 \rangle$	Stat. error	Sys. error
$0-20\%$	0.035	0.00265	0.0036	0.0403	0.00298	0.0023
$20-60\%$	0.045	0.00266	0.0010	0.0670	0.00530	0.0013

Table 4.1: Strange hadron (K_S^0 and Λ) elliptic flow integrated over p_T ($p_T < 4.0$ GeV/c) and y ($y < 1.0$) in Cu+Cu collisions at $\sqrt{s_{NN}} = 200$ GeV.

Results for K_S^0 and Λ in $\sqrt{s_{NN}} = 200$ GeV Cu+Cu collisions are summarized in Table. 4.1. Due to the statistics, we only extracted the integrated v_2 from two centrality bins. Fig. 4.12 shows the results for K_S^0, Λ and Ξ in $\sqrt{s_{NN}} = 200$ GeV Au+Au collisions. For Ξ, we followed the similar procedures applied to Λ to extract the integrated v_2. The errors are total statistical and systematic uncertainties added in quadrature.

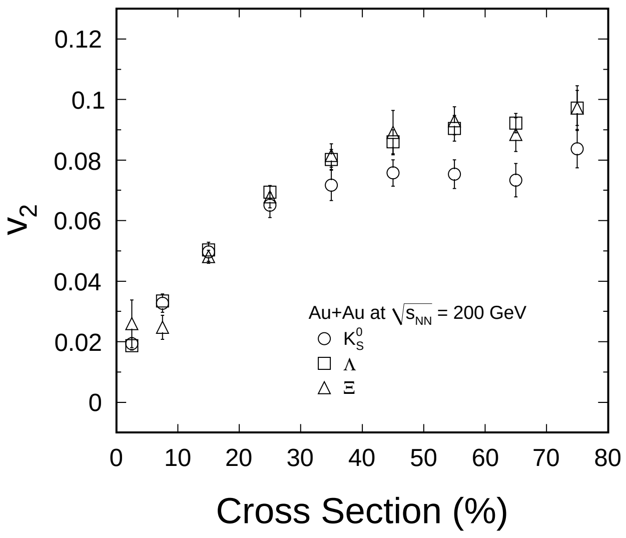

Figure 4.12: Strange hadron (K^0_S, Λ and Ξ) elliptic flow integrated over p_T ($p_T < 4.0$ GeV/c) and y ($y < 1.0$) in Au+Au collisions at $\sqrt{s_{NN}} = 200$ GeV.

CHAPTER 5

Discussion

This chapter is organized in the following way: in Section 1, we discuss the partonic collectivity at RHIC; in Section 2, we compare the experimental data to the ideal hydro calculations; in Section 3, we address the thermalization question through the system and centrality dependence of v_2; in Section 4, we investigate whether the top energy RHIC data reach the ideal hydro limit by applying a two parameter fit (Knudsen No. fit) to v_2/ε as function of particle density, the extracted Knudsen No. is also used to estimate η/s.

5.1 Partonic Collectivity

Quark coalescence [Mol03a] or recombination [Hwa03b, Fri03a] mechanisms in particle production predict that at intermediate p_T ($2 < p_T < 5$ GeV/c) Number of Quark (NQ) scaled v_2 will follow a universal curve. Thus, the NQ scaling is considered evidence for partonic degrees of freedom.

In Figure 5.1, we systematically discuss the NQ scaling at RHIC. The available data are from Au+Au and Cu+Cu colliding systems. The top beam energy is $\sqrt{s_{NN}} = 200$ GeV; we also have data from relatively lower beam energy $\sqrt{s_{NN}} = 62.4$ GeV, which can be used to study the energy dependence of NQ scaling. Figure 5.1(a) shows the results for all strange hadrons including the pure multi-strange hadrons ϕ and Ω. All data are from Run VII. With the large statistics, we can measure the v_2 much more precisely than before, especially for multi-strange hadrons. Figure 5.1(b) shows the results for K_S^0, Λ and Ξ in Cu+Cu collisions at $\sqrt{s_{NN}} = 200$ GeV. The data in Figure 5.1(c) are

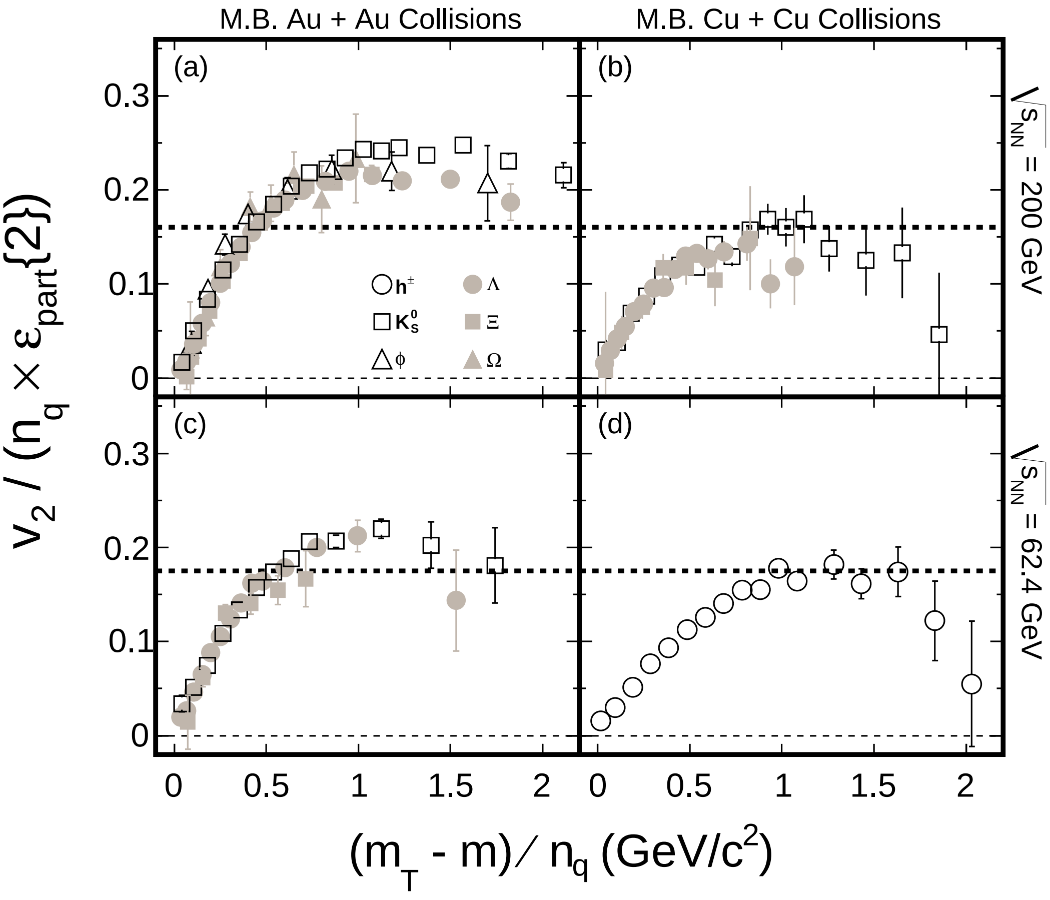

Figure 5.1: Number of Quark (NQ) and participant eccentricity scaled v_2 as a function of transverse energy $(m_T - m)$ divided by NQ for (a) Au+Au at $\sqrt{s_{NN}}$ = 200 GeV, (b) Cu+Cu at $\sqrt{s_{NN}}$ = 200 GeV, (c) Au+Au at $\sqrt{s_{NN}}$ = 62.4 GeV and (d) Cu+Cu at $\sqrt{s_{NN}}$ = 62.4 GeV minimum bias events. Open circles, squares, triangles and solid circles, squares, triangles represent charged hadrons, K_S^0, ϕ, Λ, Ξ and Ω, respectively. The error bars on the data points represent statistical uncertainties.

from the STAR publication [Abe07a]. Due to limited statistics, only charged hadron results are shown in Figure 5.1(d) for Cu+Cu collisions at $\sqrt{s_{NN}} = 62.4$ GeV. We set the mass of charged hadron equal to that of π. In order to remove the initial geometry, v_2 is scaled by eccentricity. The participant eccentricity is the initial configuration space eccentricity of the participants which is defined by [Bac07a]

$$\varepsilon_{\text{part}} = \frac{\sqrt{(\sigma_y^2 - \sigma_x^2) + 4(\sigma_{xy}^2)}}{\sigma_y^2 + \sigma_x^2} \tag{5.1}$$

In this formula, $\sigma_x^2 = \langle x^2 \rangle - \langle x \rangle^2$, $\sigma_y^2 = \langle y^2 \rangle - \langle y \rangle^2$ and $\sigma_{xy} = \langle xy \rangle - \langle x \rangle \langle y \rangle$, with x, y being the position of the participating nucleons in the transverse plane. The root mean square of the participant eccentricity

$$\varepsilon_{\text{part}}\{2\} = \sqrt{\langle \varepsilon_{\text{part}}^2 \rangle} \tag{5.2}$$

is calculated from the Monte Carlo Glauber model [Mil03b, Mil07a] and Color Glass Condensate (CGC) model [Dre05a, Dre07a, Dre07b, Dre09a]. (See Table 5.1 for $\varepsilon_{\text{part}}\{2\}$.) Since the event plane is constructed from the hadrons which have their origin in participant nucleons, what we actually measure is the root mean square of v_2 with respect to the participant plane [Pos09a] when the event plane resolution is less than 0.2. In this case, $\varepsilon_{\text{part}}\{2\}$ is the appropriate measure of the initial geometric anisotropy taking the event-by-event fluctuations into account [Vol06a, Alv08a, Pos09a].

In Figure 5.1, Glauber model has been used to calculate the eccentricities, but it is similar in the case of CGC model. The conclusions from Figure 5.1 are as follows:

(i) There is a clear number of quark (NQ) scaling for all systems and beam energies studied here. (Due to the limited statics, this test is not done for Cu+Cu collisions at $\sqrt{s_{NN}} = 62.4$ GeV.) It indicate the partonic collectivity has been built up at RHIC.

(ii) After removing the initial geometry by eccentricity, stronger collective flow can be observed in the larger system.

In particularly, in Figure 5.2, we compare the elliptic flow of protons and pions to that of the multi-strange hadrons Ω and ϕ. (These hadrons have valence quark content $sss(\overline{sss})$ and $(\overline{s}s)$ respectively.) The important point is that the Ω is nearly

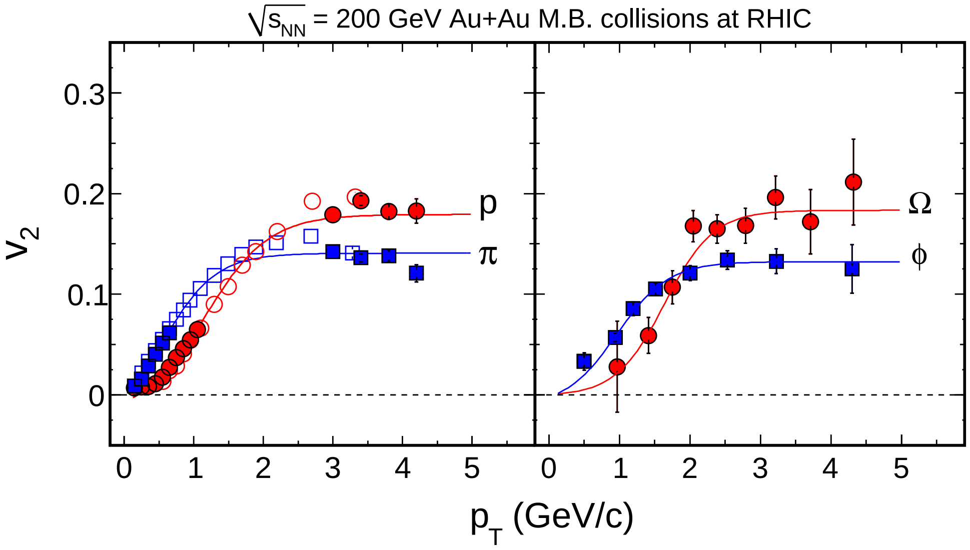

Figure 5.2: v_2 as function of p_T for π, p (left) and ϕ, Ω (right) in Au + Au minimum-bias collisions at $\sqrt{s_{NN}} = 200$ GeV. Open symbols represent results from PHENIX [Iss06a]. Lines represent NQ-inspired fit [Don04a].

twice as heavy as the proton and more importantly, both Ω and ϕ are less sensitive to the hadronic process [Sho85a, Hec98a, Bas99b, Che03a, Bia81a, Mul72a]. Nevertheless they show nearly the same elliptic flow as the protons and pions. This provides fairly convincing evidence that the majority of the elliptic flow develops during the partonic process. Thus, it directly points to partonic collectivity at RHIC.

5.2 Ideal Hydrodynamics Test

The results for π, p, K_S^0, Λ, Ξ, and Ω are shown in Figure 5.3 for various centralities of Au+Au collisions at $\sqrt{s_{NN}} = 200$ GeV. Shown are results for minimum bias and three other centrality bins. All $v_2(p_T)$ results are from the event plane method. The systematic uncertainties extracted from PID cuts, background subtractions, and combining centralities are shown as shaded bars in the figure. The systematic uncertainty in the method itself is not included. The shaded band in figure 5.3(c) indicates the nonflow systematic uncertainties for K_S^0 and Λ for the $10-40\%$ centrality bin.

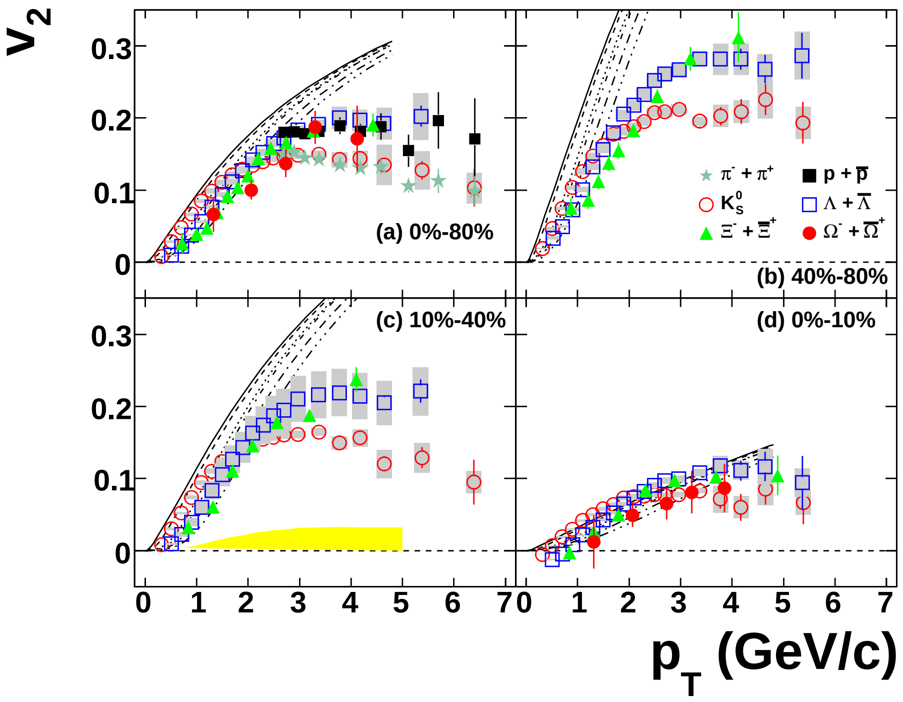

Figure 5.3: v_2 of K_S^0 (open circles), Λ (open squares), Ξ (filled triangles), and Ω (filled circles) as a function of p_T for (a) $0-80\%$, (b) $40-80\%$, (c) $10-40\%$, and (d) $0-10\%$ in Au+Au collisions at $\sqrt{s_{NN}}$ = 200 GeV. The error bars represent statistical uncertainties. The bands on the data points represent systematic uncertainties as discussed in the text. For comparison, π (stars) and p (filled squares) results are shown in (a). The systematic uncertainty of nonflow for K_S^0 and Λ for $10-40\%$ (c) is plotted as a shaded band near 0. For comparison, results from ideal hydrodynamic calculations [Huo06a, Huo06b] are shown: at a given p_T, from top to bottom, the lines represent the results for π, K, p, Λ, Ξ, and Ω. The figure is from [Abe08a].

The results from an ideal hydrodynamic model [Huo06a, Huo06b] are displayed by the lines. Figure 5.3 shows that the ideal hydrodynamic model calculations reproduce the mass ordering of v_2 in the relatively low p_T region (the heavier the mass, the smaller the v_2) but overshoot the values of v_2 for all centrality bins. There seems to be a p_T dependence in the disagreement, and for more central collisions, the overshoot does not take place until a higher p_T. In other words, the system agrees better with the ideal hydrodynamic model for more central collisions. Although we do not expect a large nonflow contribution at the low transverse momentum region, the centrality selections between the model calculations based on the impact parameter and the data based on the multiplicity are different, which may also affect the model and data agreement. Note that we observe possible negative values of $v_2(p_T)$ for the heavier hadrons at the lowest observed p_T in the most central Au+Au collisions. At higher p_T, the hydrodynamic type mass ordering evolves into a hadron type ordering (baryons versus mesons). There the results show two groups depending on the number of quarks in the hadron; the baryons are higher than the mesons. For all p_T, v_2 evolves toward larger values in going from central collisions to more peripheral collisions. The ideal hydrodynamic model also predicts this centrality dependence, though it fails to describe the behavior at higher p_T.

Figure 5.4 shows the v_2 for K_S^0, Λ and Ξ as a function of p_T in different centrality selections for Cu+Cu collisions at $\sqrt{s_{NN}} = 200$ GeV along with results of hydrodynamical calculations [Huo08a]. The ideal hydrodynamical model does not describe the centrality dependence of our data. For $0-20\%$, the model under-predicts the data and for $20-60\%$, it over-predicts the v_2.

As a conclusion, we find that the ideal hydrodynamical calculations fails to reproduce the data in both Au+Au and Cu+Cu collisions at $\sqrt{s_{NN}} = 200$ GeV. Since hydrodynamics is a theory based on thermalization, it may provide a tool to test whether the system created at RHIC reaches thermalization. To date, there are serval effects not included in the model, such as geometrical fluctuations in the initial conditions (particularly important in central collisions), finite viscosity effects. It remains to be seen if these effects can account for the difference between the models and data.

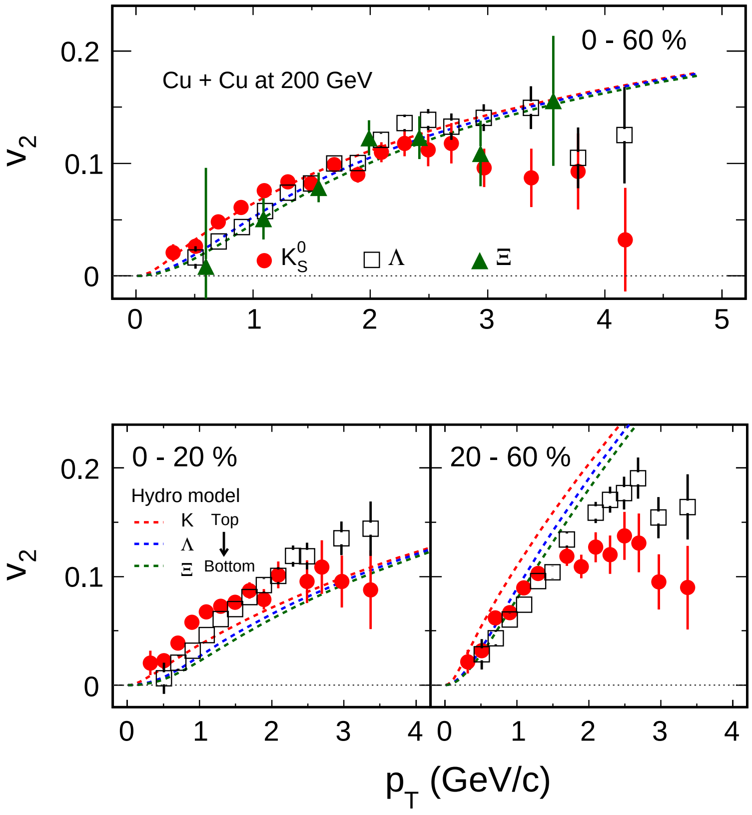

Figure 5.4: v_2 as a function of p_T for K_S^0, Λ and Ξ in $0-60\%$ (top), $0-20\%$ and $20-60\%$ (bottom) Cu+Cu collisions at $\sqrt{s_{NN}} = 200$ GeV. Dashed lines represent ideal hydrodynamical calculation [Huo08a]. From top to bottom, the lines represent the results for K, Λ and Ξ.

5.3 System and Centrality Dependence of v_2

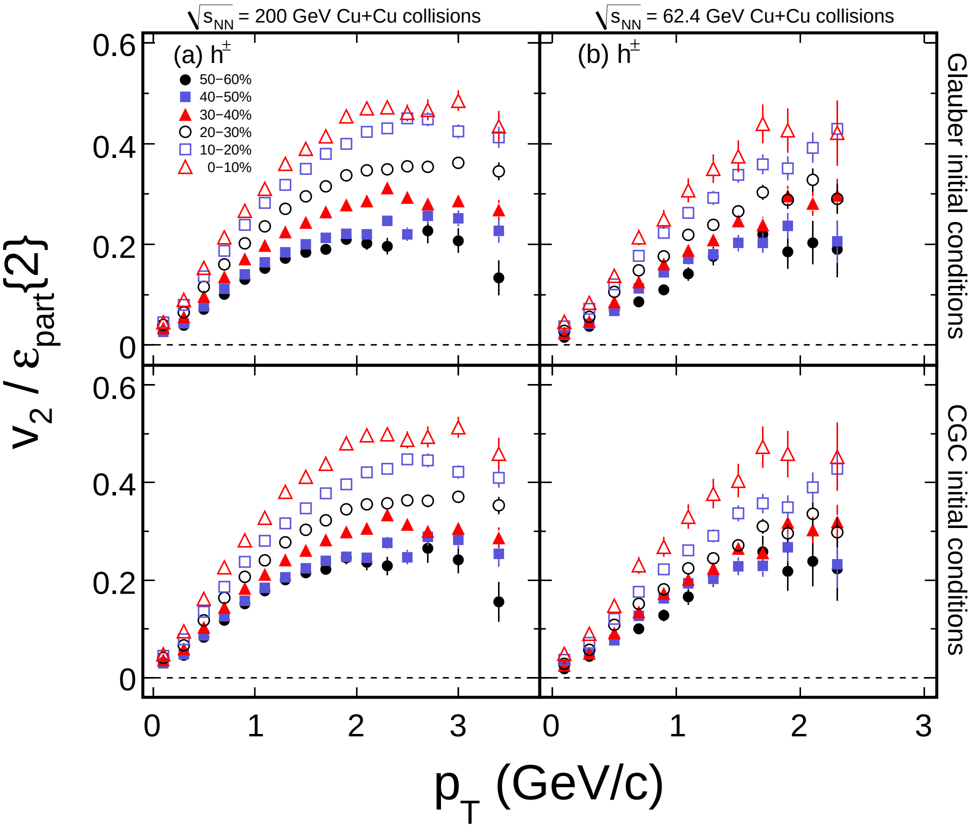

Figure 5.5: Charged hadron v_2 scaled by participant eccentricity as a function of p_T in $\sqrt{s_{NN}}$ = 200 and 62.4 GeV Cu+Cu collisions.

The centrality and system-size dependence of v_2 is related to the physics of the system created in high energy nuclear collisions. In the ideal hydrodynamic limit the centrality dependence of elliptic flow is mostly defined by the elliptic anisotropy of the overlapping region of the colliding nuclei, and in the low-density limit by the product of the elliptic anisotropy and the multiplicity. Thus, the centrality and system-size dependence of elliptic flow should be a good indicator of the degree of equilibration reached in the reaction [Vol00a].

For a study of the centrality dependence of $v_2(p_T)$ in Cu+Cu collisions together with Au+Au collisions, we divide $v_2(p_T)$ by the initial spatial anisotropy, eccentric-

	Centrality	$\varepsilon_{\mathrm{part}}\{2\}$(CGC)	$\varepsilon_{\mathrm{part}}\{2\}$(Glauber)	N_{part}
Au+Au	$0-80\%$	0.338 ± 0.002	0.302 ± 0.004	126 ± 8
	$0-10\%$	0.148 ± 0.001	0.123 ± 0.003	326 ± 6
	$10-40\%$	0.353 ± 0.001	0.296 ± 0.009	173 ± 10
	$40-80\%$	0.554 ± 0.002	0.533 ± 0.018	42 ± 7
Cu+Cu	$0-60\%$	0.336 ± 0.009	0.350 ± 0.008	51 ± 2
	$0-20\%$	0.230 ± 0.010	0.235 ± 0.008	87 ± 2
	$20-60\%$	0.434 ± 0.003	0.468 ± 0.016	34 ± 1
	$0-10\%$	0.187 ± 0.002	0.197 ± 0.002	99 ± 2
	$10-20\%$	0.281 ± 0.002	0.279 ± 0.008	75 ± 2
	$20-30\%$	0.360 ± 0.003	0.369 ± 0.009	54 ± 1
	$30-40\%$	0.428 ± 0.002	0.458 ± 0.017	38 ± 1
	$40-50\%$	0.490 ± 0.002	0.550 ± 0.021	26 ± 1
	$50-60\%$	0.555 ± 0.004	0.643 ± 0.031	17 ± 1

Table 5.1: Participant eccentricity $\varepsilon_{\mathrm{part}}\{2\}$ and number of participants N_{part} from the Monte Carlo Glauber model [Mil03b, Mil07a] and Color Glass Condensate (CGC) model [Dre05a, Dre07a, Dre07b, Dre09a] calculations in Au+Au and Cu+Cu collisions at $\sqrt{s_{NN}} = 200$ GeV. The quoted errors are total statistical and systematic uncertainties added in quadrature.

ity, to remove this geometric effect. Figure 5.5 shows the centrality dependence of $v_2(p_T)/\varepsilon_{\text{part}}\{2\}$ for $h^{\pm}$ in 200 and 62.4 GeV Cu+Cu collisions. For a given centrality bin, $v_2(p_T)/\varepsilon_{\text{part}}\{2\}$ initially increases with p_T and then flattens or falls off at higher p_T. After the geometric effect is removed, the ordering of the distributions as a function of centrality, observed in Fig. 4.5, is reversed: the more central the collision, the higher the $v_2(p_T)/\varepsilon_{\text{part}}\{2\}$. This suggests that the strength of collective motion is larger in more central collisions.

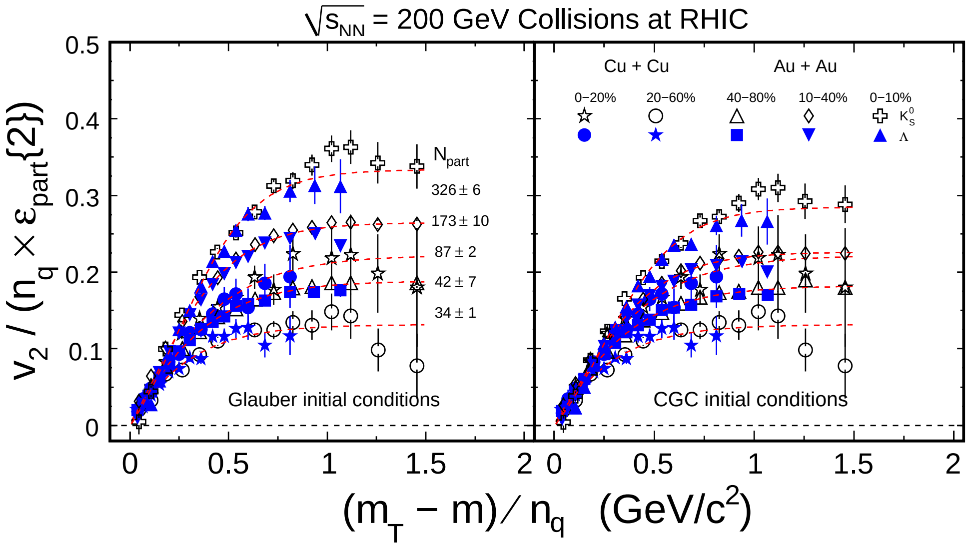

Figure 5.6: Centrality dependence of v_2 scaled by number of quarks and participant eccentricity ($v_2/(n_q{\times}\varepsilon_{\text{part}}\{2\})$) for K^0_S (left) and Λ (right) as a function of $(m_T - m)/n_q$ in $0-10\%$, $10-40\%$ and $40-80\%$ Au+Au collisions (open symbols) [Abe08a] and $0-20\%$ and $20-60\%$ Cu+Cu collisions (solid symbols) at $\sqrt{s_{NN}}$ = 200 GeV. Curves are the results of n_q-scaling fits from Eq. (4.4) normalized by $\varepsilon_{\text{part}}\{2\}$ to combined K^0_S and Λ for five centrality bins. At a given p_T, from top to bottom, the curves show a decreasing trend as a function of N_{part}.

To further study the centrality dependence of strange hadron v_2, we normalized the n_q-scaled values by $\varepsilon_{\text{part}}\{2\}$ and plotted them as a function of $(m_T - m)/n_q$. The centrality dependence of K^0_S and Λ results are shown in Fig. 5.6. The full symbols show from top to bottom the results from $0-20\%$ and $20-60\%$ centrality Cu+Cu collisions. For comparison, the results from 200 GeV Au+Au collisions [Abe08a] are shown by open

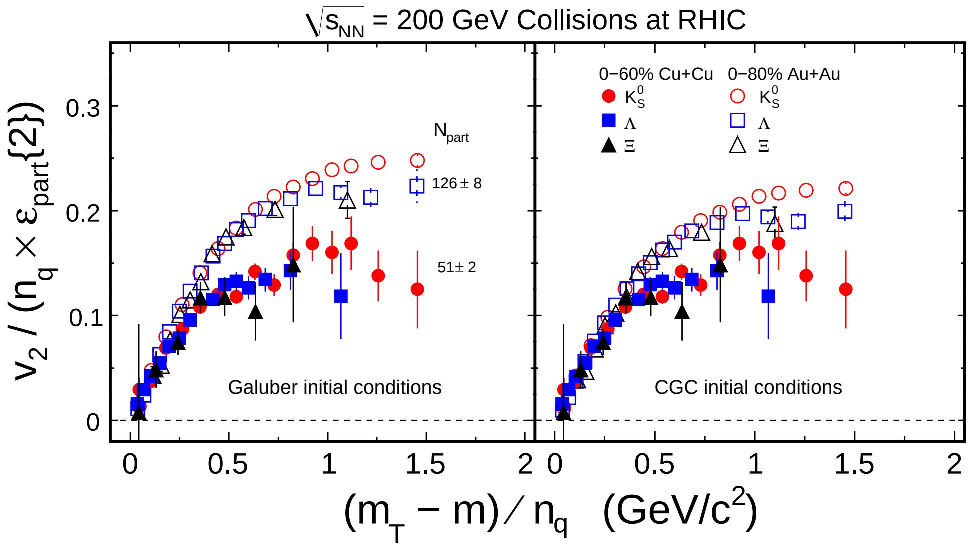

Figure 5.7: Number of quarks and participant eccentricity scaled v_2 ($v_2/(n_q{\times}\varepsilon_{\rm part}\{2\})$) of identified particles as a function of $(m_T - m)/n_q$ in $0-80\%$ Au+Au collisions (open symbols) [Abe08a] and $0-60\%$ Cu+Cu collisions (closed symbols) at $\sqrt{s_{NN}}$ = 200 GeV. Circles, squares and triangles represent the data for K^0_S, Λ and Ξ, respectively.

symbols in Fig. 5.6. The results in Au+Au collisions are slightly different ($\sim 10\%$ larger) from the previous published results [Abe08a], which were calculated directly from the wide centrality bins. From top to bottom, the results are from $0-10\%$, $10-40\%$ and $40-80\%$ centrality bins. Curves represent n_q-scaling fits from Eq. (4.4) normalized by $\varepsilon_{\rm part}\{2\}$ to the combined data of K^0_S and Λ for five centrality bins. For a given centrality, K^0_S and Λ results follow a universal curve, which means partonic collective flow is explicitly seen in the measured scaling with n_q and $\varepsilon_{\rm part}\{2\}$. For a given collision system, the stronger partonic collective flow is apparent as higher scaled v_2 value in more central collisions. To study the system-size dependence of the scaling properties, the results from $0-60\%$ centrality Cu+Cu and $0-80\%$ Au+Au collisions are shown in Fig. 5.7. The stronger collective motion in Au+Au compared to Cu+Cu collisions becomes obvious although the constituent quark degrees of freedom have been taken into account in both systems.

In the ideal hydrodynamic limit where dynamic thermalization is reached, the mean free path is much less than the geometric size of the system. The geometric size of the system and the centrality dependence of flow is totally governed by the initial geometry (eccentricity) [Vol00a]. As there is no universal scaling with the eccentricity among either different collision centralities or different collision system sizes, this indicates that the ideal hydrodynamic limit is not reached in Cu+Cu collisions, presumably because the assumption of thermalization is not attained. In addition, $v_2/(n_q \times \varepsilon_{\rm part}\{2\})$ shows an increasing trend as a function of $N_{\rm part}$ (See Fig. 5.6). Table 5.1 lists the values of eccentricity and $N_{\rm part}$ for the used centrality bins in Au+Au and Cu+Cu collisions. This suggests that the measured v_2 is not only dependent on the initial geometry, but also on $N_{\rm part}$.

5.4 The Ideal Hydrodynamic Limit

It was shown, in [Adl02b, Ada05a], that the measured v_2 scaled by the spatial eccentricity reaches the expected ideal hydrodynamic values but this only happens for the most central collisions. The discrepancy for more peripheral collisions as well as at lower energies and away from mid-rapidity indicates that for these collisions the elliptic flow has significant non-ideal hydrodynamic contributions. Much of this discrepancy could be explained by incorporating viscous contributions of the hadronic phase [Tea01a, Tea00a, Hir06a, Hir05a]. The resulting picture was a perfect liquid for the hot and dense part of the system surrounded by a dissipative hadronic corona. Kovtun, Son and Starinets [Kov04a], showed that conformal field theories with gravity duals have a ratio of viscosity η to entropy density s of $1/4\pi$ (in natural units). They conjectured that this value is a bound for any relativistic thermal field theory (However, Buchel, Mayers and Sinha argued that such bound can be violated in superconformal gauge theories with non-equal central charges $c \neq a$ [Buc08a]). In addition, Teaney [Tea03a] had pointed out that already very small viscosities, of the magnitude of the bound, would lead to a significant reduction in the predicted elliptic flow. Therefore models which take into account these effects find very strong constraints on the the magnitude of η/s when trying to describe the large observed elliptic flow. However, more recently, it was realized that uncertainties in the initial conditions, e.g. the spatial eccentricity [Hir05a], and uncertainties in the EoS [Huo05a] are substantial as well, which opens up the range of possible (larger) values of η/s.

Currently there are two promising approaches to quantify how big the possible discrepancy between data and ideal hydrodynamics. The first approach is to match the data using hydrodynamic models which incorporate viscous corrections [Son08a, Rom08a]. One of the drawbacks of this approach is that η/s is not the only unknown, also the initial conditions and EoS need to be varied. The second approach is a fit of v_2/ε versus particle density based on a parametrization in terms of the Knudsen number [Bha05a, Oll07a]. The Knudsen number K is the mean free path of the constituents divided by the system size. The fit yields K and extrapolating the fit to $K = 0$ yields the ideal hydrodynamic limit of v_2/ε. The latter defines the effective velocity of sound and thus the effective EoS.

In this section, we will present STAR measurements of v_2/ε as a function of particle density in the transverse plane. This observable is considered sensitive to deviations from ideal hydrodynamics. We will compare these observables with transport model calculations and test if they can be understood with a common Knudsen number. Additionally we will test how the conclusions depend on varying the initial conditions.

To quantify this further we fit v_2/ε versus particle density based on the parameterization in terms of the Knudsen number [Bha05a, Oll07a] given by:

$$\begin{aligned} \frac{v_2}{\varepsilon} &= [\frac{v_2}{\varepsilon}]_{\text{hydro}} \frac{1}{1 + K/K_0} \\ &= [\frac{v_2}{\varepsilon}]_{\text{hydro}} \frac{1}{1 + (\sigma c_s \frac{1}{S}\frac{dN}{dy})^{-1}\frac{1}{K_0}} \end{aligned} \tag{5.3}$$

where K is the Knudsen number, and K_0 is a constant which can be determined through transport calculations. Following [Oll07a] we take $K_0 = 0.7 \pm 0.03$. There is a factor of 40 difference S given here and that in [Oll07a] which stems from the different definition and units of S (in STAR, $S = \pi\sqrt{\bar{x^2}\ \bar{y^2}}$, in fm^2 and in [Oll07a], $S = 4\pi\sqrt{\bar{x^2}\ \bar{y^2}}$, in mb). $[\frac{v_2}{\varepsilon}]/[\frac{v_2}{\varepsilon}]_{\text{hydro}}$ and σc_s are free parameters that extracted from fitting the data. The formula has the two desired properties at two extremes: $1 - [\frac{v_2}{\varepsilon}]/[\frac{v_2}{\varepsilon}]_{\text{hydro}} \propto$ K when K is small (ideal hydro limit), and $[\frac{v_2}{\varepsilon}]/[\frac{v_2}{\varepsilon}]_{\text{hydro}} \propto 1/$K when K is large (low density limit). In this approach the hydrodynamic limit of v_2/ε can be only asymptotically approached.

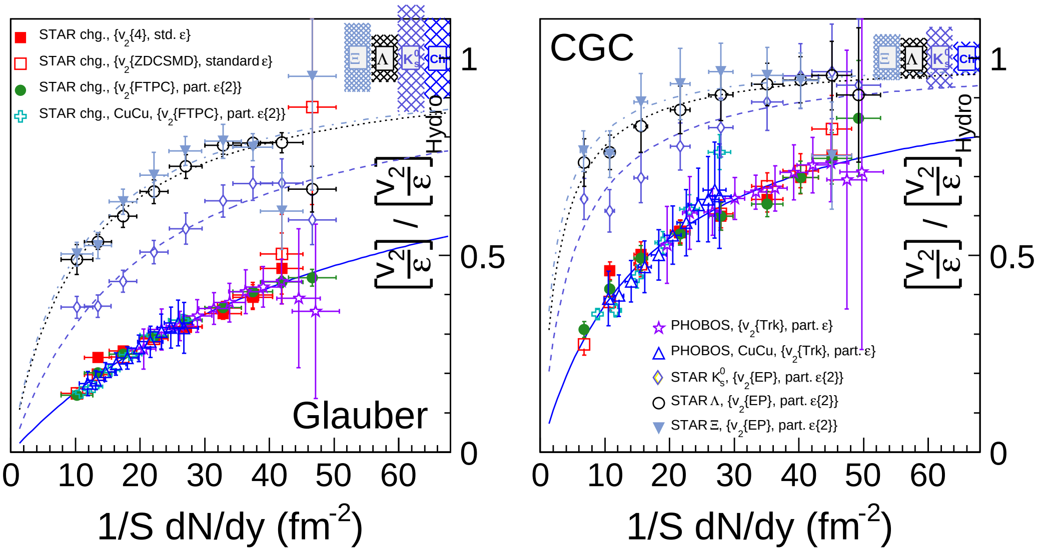

Figure 5.8: v_2/ε scaled by the corresponding hydrodynamic limits obtained from the simultaneous fitting, for Glauber (left) and CGC (right) initial conditions. The hydrodynamic limit is by definition centered at unity, with error represented by the cross-shaded bars.

In Fig. 5.8, $[\frac{v_2}{\varepsilon}]/[\frac{v_2}{\varepsilon}]_{\mathrm{hydro}}$ is plotted as a function of $1/S\ dN/dy$ for various particle species. The v_2 measurements that are sensitive to the participant plane anisotropy are scaled by the participant two particle cumulant eccentricity, and for the v_2 measurements that are sensitive to the reaction plane, by the standard eccentricity [Bha06a, Vol08a]. The participant plane measurements are i) v_2 measured with event plane constructed from Forward Time Projection Chamber (FTPC) ($v_2\{\mathrm{FTPC}\}$), ii) STAR's event plane v_2 ($v_2\{\mathrm{EP}\}$), iii) PHOBOS' track-based v_2 measurement ($v_2\{\mathrm{Trk}\}$) [Bac05b, Bac07a]; and the reaction plane measurements are STAR's four particle cumulant v_2 ($v_2\{4\}$) and v_2 measured by event plane constructed from spectator neutrons ($v_2\{\mathrm{ZDC}-\mathrm{SMD}\}$). Data points are for collisions at $\sqrt{s_{NN}} = 200$ GeV, and by default they are for Au+Au collisions unless otherwise specified by the legends. The left panel is for the case with Glauber as initial condition, and the right panel, CGC. For the Glauber case, S and ε are calculated from a Monte Carlo Glauber with cross section of 42 mb. For the CGC case, they are based on Monte Carlo fKLN calculations [Oll07a]. dN/dy is taken from STAR's publication [Abe09a], and dN/dy used for PHOBOS data points is obtained by projecting STAR's measurements with PHOBOS total cross sections. For charged particles, the fit is applied simultaneously to corresponding data sets (lowest group in the plot) with the additional constraint that σc_s is the same for individual data sets. The curves are obtained from the fitting and they represent the relative fraction to the fitted hydro limit, $\left[\frac{v_2}{\varepsilon}\right] / \left[\frac{v_2}{\varepsilon}\right]_{\rm hydro}$. The more saturation in the shape, the closer to the fitted hydro limit. A stronger saturation in shape is observed in CGC case if compared to that in Glauber case. That is understood as, going from peripheral to central collisions, CGC predicts a smaller decrease of eccentricity than Glauber does. The plot shows a splitting of $[\frac{v_2}{\varepsilon}]/[\frac{v_2}{\varepsilon}]_{\rm hydro}$ due to particle's mass. The heavier the particle, the more saturation in the shape is observed. Such mass hierarchy is not a built-in feature in the model [Bha05a, Oll07a], and it is desirable to see if other models can explain it.

The extracted σc_s is not meaningful for massive particles because in the transport model [Bha05a, Oll07a] that motivated this fit, $K_0 = 0.7$ is obtained with massless particles and is not applicable for massive particles. In the following, we quote numbers only for charged particles (mostly pions). To check if the procedure is robust, the fit is repeated with additional two formula.

$$\frac{v_2}{\varepsilon} = [\frac{v_2}{\varepsilon}]_{\rm hydro}\frac{2}{\pi}{\rm atan}(\frac{1}{K/K_0}) \tag{5.4}$$

$$\frac{v_2}{\varepsilon} = [\frac{v_2}{\varepsilon}]_{\rm hydro}\frac{1}{2}(1 - e^{-\frac{1}{K/K_0}} + e^{-K/K_0}) \tag{5.5}$$

In central collisions, for both Glauber case and CGC case, $[\frac{v_2}{\varepsilon}]/[\frac{v_2}{\varepsilon}]_{\rm hydro}$ obtained with different fit formula are consistent with each other within ~20% in absolute value, and the extracted σc_s, ~30% in relative value. Systematical errors from v_2, ε, S and dN/dy have been decomposed into correlated and uncorrelated parts, for the latter, a special procedure [Pdg08a] is carried out so that it can be included, together with uncorrelated error, in the final error extracted from the fitting. In most v_2 values used in this analysis, the correlations not related to reaction plane (nonflow) has been effectively suppressed, either by η gap between particles used to reconstruct the event plane and particles used to study the flow, or by measuring multi-particle cumulants v_2. However, it is still possible that there is additional systematical error that comes from remaining nonflow in v_2 measurements that are based on two particle correlations. Its magnitude is estimated by comparing σc_s obtained from fitting STAR's $v_2\{\text{FTPC}\}$ and PHOBOS' $v_2\{\text{Trk}\}$, to that obtained with fitting STAR's $v_2\{\text{EP}\}$ for charged particles with corrections [Pos09a] made with following assumptions: 1.) v_2 fluctuations are originated from initial Glauber or CGC eccentricity fluctuations, 2.) azimuthal correlations in p+p collisions are all due to nonflow, 3.) nonflow in Au+Au collisions is equivalent to that in p+p collisions scaled by $2/N_{\text{part}}$, where N_{part} is the number of participant nucleons. From the fitted curve, for central Au+Au collisions, $[\frac{v_2}{\varepsilon}]/[\frac{v_2}{\varepsilon}]_{\text{hydro}}$ is $0.46 \pm 0.05(\text{fit})^{+0.23}_{-0}(\text{formula}) + 0.05(\text{nonflow})$ and $0.75 \pm 0.03(\text{fit})^{+0.14}_{-0.06}(\text{formula}) - 0.07(\text{nonflow})$, for Glauber case and CGC case, respectively. The fitted σc_s is $1.03 \pm 0.38(\text{fit})^{+0.31}_{-0}(\text{formula}) + 0.20(\text{nonflow})$ mb and $3.41 \pm 0.69(\text{fit})^{+0}_{-0.96}(\text{formula}) - 1.12(\text{nonflow})$ mb, for Glauber case and CGC case, respectively. For both initial conditions, there still might be considerable room for flow to increase before the system saturates at hydrodynamic limits.

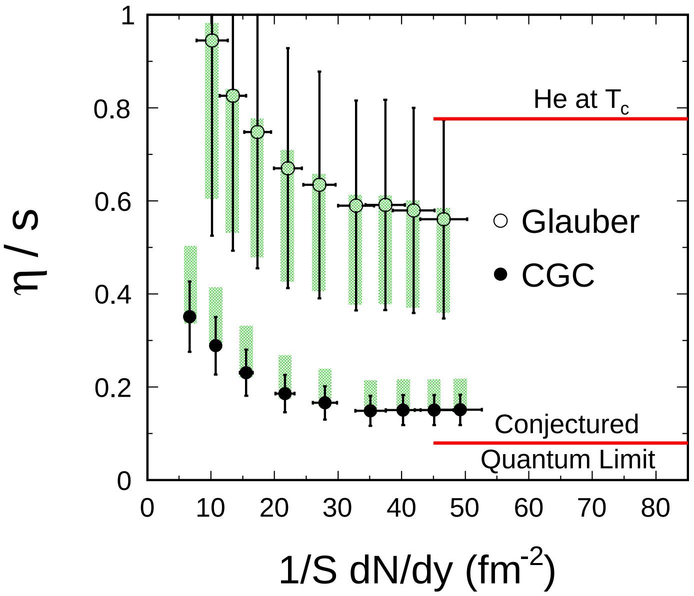

Figure 5.9: η/s as a function of $1/S\ dN/dy$ for collisions at $\sqrt{s_{NN}}$ =200 GeV. The conjectured quantum limit, as well as η/s for He at T_c is also plotted for comparison.

Following [Tea03a], the viscosity for a classical gas of massless particles with isotropic differential cross sections is $\eta = 1.264T/\sigma$ [Kox76a]. It is arguable to apply the formula to strongly interacting dense matter, however, in practice the viscosity recovered from this procedure agrees well with that obtained from viscous hydrodynamic calculations. [Sne09a]. Taking the entropy density for a classical ultrarelativistic gas as $s = 4n$, with n the particle density, then η/s can be calculated as $\eta/s = 0.316\frac{T}{\sigma n} = 0.316\frac{T}{\sigma c_s}\frac{S\bar{R}}{dN/dy}$, where σc_s is from fitting v_2/ε mentioned above, and $\bar{R} \equiv \frac{1}{\sqrt{1/\langle x^2\rangle + 1/\langle y^2\rangle}}$ is obtained from Glauber(CGC) calculations. The temperature T is obtained from fitting STAR's π m_T slope [Abe09a]. In Fig. 5.9, η/s is plotted as a function of $1/S\ dN/dy$ for Glauber and CGC initial conditions. The symmetrical and asymmetrical error from σc_s has been propagated into the errors of η/s accordingly. The difference of T obtained from fitting STAR [Abe09a] and PHENIX's [Adl04a] π m_T spectra has been included in the systematical error. η/s for Glauber initial condition is 7.05 ± 2.68(sym. error)$^{+0.28}_{-2.55}$(asym. error) times of the conjectured quantum limit, and for CGC, 1.9 ± 0.41(sym. error)$^{+0.83}_{-0.08}$(asym. error) times. Both lower than η/s for He at T_c. The extracted η/s is different than that in [Oll07a] because the $1/S\ dN/dy$ used in [Oll07a] is solely from model calculations while we used dN/dy from measurements. η/s for CGC initial condition is smaller than that for Glauber initial condition, because with CGC initial condition, a stronger saturation is seen in the shape of v_2/ε vs. $1/S\ dN/dy$, which gives a larger σc_s. This does not necessarily contradict to the conclusion arrived from viscous hydro calculations [Son08a, Rom08a], in which the Equation of State is chosen to be the same for the two initial conditions. For $1/S\ dN/dy > 15$, η/s is consistent with a constant, as one expected from transport model [Oll07a]. Note that the extracted η/s is an effective quantity which includes viscous effects over different phases, including a hadronic phase for which the expected viscous effect is larger than that of the QGP phase.

In summary, we have presented v_2 scaled by initial eccentricities as a function of $1/S\ dN/dy$, we see more saturation for heavy particles. Our measurements for charged particles are compared to transport model calculations. It is found that the the system has reached $0.46^{+0.24}_{-0.07}$ and $0.75^{+0.14}_{-0.10}$ of the value at which it is supposed to saturate (ideal hydrodynamic limit), indicating that there still might be considerable amount of room for flow to increase. We report the σc_s for Glauber initial condition as 1.78 ± 0.66(fit)$^{+0.53}_{-0}$(formula)$+0.35$(nonflow) mb, and 5.90 ± 1.2(fit)$^{+0}_{-1.67}$(formula)-1.94(nonflow) mb for CGC initial condition. We calculated η/s as a function of $1/S\ dN/dy$ for collisions at 200 GeV. For $1/S\ dN/dy$ that corresponds to central Au+Au collisions at 200 GeV, it is $7.05 \pm 2.68(\text{sym. error})^{+0.28}_{-2.55}(\text{asym. error})$ and $1.9 \pm 0.41(\text{sym. error})^{+0.83}_{-0.08}(\text{asym. error})$ times the conjectured quantum limit, for Glauber and CGC initial condition respectively.

CHAPTER 6

Summary and Outlook

In this thesis, we analyze the data collected with the STAR detector from $\sqrt{s_{NN}} =$ 62.4 and 200 GeV Cu+Cu collisions during the fifth RHIC run in 2005 and $\sqrt{s_{NN}} =$ 9.2 and 200 GeV Au+Au collisions during the seventh run in 2007. We present results on elliptic flow v_2 of charged hadrons and identified particles in the midrapidity region $|\eta| < 1.0$. Significant reduction in systematic uncertainty of the measurement due to non-flow effects has been achieved by correlating particles at midrapidity, $|\eta| < 1.0$, with those at forward rapidity, $2.5 < |\eta| < 4.0$. As a part of the systematic study, we also present azimuthal correlations in p+p collisions at $\sqrt{s_{NN}} =$ 200 GeV, which are used for estimating the error from non-flow effects.

We study the system size dependence of elliptic flow by comparing the results from Cu+Cu collisions with previously results [Abe08a] from Au+Au collisions at $\sqrt{s_{NN}} =$ 200 GeV. We observe that $v_2(p_T)$ of strange hadrons has similar scaling properties as was first observed in Au+Au collisions, i.e.: (i) at low transverse momenta, $p_T < 2$ GeV/c, v_2 scales with transverse kinetic energy, $m_T - m$, and (ii) at intermediate p_T, $2 < p_T < 5$ GeV/c, it scales with the number of constituent quarks (NQ).

We systematically discuss the NQ scaling at RHIC and find it holds in the intermediate p_T region, $2 < p_T < 5$ GeV/c, for all systems and beam energies studied here. In particularly, the multi-strange hadrons Ω and ϕ show nearly the same elliptic flow as the protons and pions. This provides fairly convincing evidence that the majority of the elliptic flow develops during the partonic process. Thus, it indicates the partonic collectivity has been built up at RHIC.

A comparison between data and ideal hydrodynamic calculations has been made in Au+Au and Cu+Cu collisions at $\sqrt{s_{NN}} = 200$ GeV collisions. We find that ideal hydrodynamic calculations fail to reproduce the centrality dependence of $v_2(p_T)$.

It is found that the $1/S\ dN/dy$ dependence of v_2/ε can be described well by transport models with finite Knudsen numbers, even for central collisions. The result indicates that the system has reached $0.46^{+0.24}_{-0.07}$ and $0.75^{+0.14}_{-0.10}$ of ideal hydrodynamic limits, using Glauber and Color Glass Condensate (CGC) initial condition, respectively. Constrains on the product of the cross section and the speed of sound are provided, η/s is estimated.

The upgrade program of STAR detectors are under progress to expand the detection capabilities and physics program. TOF upgrade which has been finished successfully in 2009 improves the ability of particle identification. With the incoming Heavy Flavor Tracker (HFT) [Wie06a], direct reconstruction of heavy quark contained hadrons, such as J/ψ, D mesons, will be possible. The measurement of the elliptic flow of heavy quark contained hadrons down to very low p_T values can shed light on the thermalization issue in the heavy ion collisions. The sizable flow of heavy quarks (c quark) can be regarded as evidence of frequent rescatterings of light quarks (u, d, s quarks). Measurements of the elliptic flow on the heavy quark contained hadrons will get information on the thermalization issue for light quarks. Systematic study of heavy quark contained hadrons will help us to understand the properties of the hot and matter created in heavy ion collisions and determine the Equation of State finally.

As the NQ scaling of v_2 indicates the hot and dense matter created in the heavy ion collisions is dominated the partonic degrees of freedom, thus the beam energy dependence of the NQ scaling of v_2 should be a powerful tool to search for the QCD phase boundary in the future Beam Energy Scan program at RHIC. When scan from high to low beam energy, the violation of the NQ scaling for identified hadrons, especially for the multi-strange hadron, such as ϕ or Ω, will signal a system where hadronic degrees of freedom dominant.

References

[Abe03a] J. Abele et al. *Nucl. Instru. Methd A*, **499** 692, 2003.

[Abe07a] B. I. Abelev et al. (STAR Collaboration), *Phys. Rev. C* **75**, 054906 (2007).

[Abe08a] B. I. Abelev et al. (STAR Collaboration), *Phys. Rev. C* **77**, 054901 (2008).

[Abe09a] B. I. Abelev et al. (STAR collaboration), *Phys. Rev. C* **79**, 034909 (2009).

[Abe10a] B. I. Abelev et al. (STAR collaboration), *Phys. Rev. C* **81**, 024911 (2010).

[Ack01a] K. H. Ackermann et al. *Phys. Rev. Lett.*, **86** 402, 2001.

[Ack03a] K. Ackermann et al. *Nucl. Instru. Methd A*, **499** 624, 2003.

[Ack03b] K. Ackermann et al. *Nucl. Instru. Methd A*, **499** 709, 2003.

[Ada03a] M. Adamczyk et al. *Nucl. Instru. Methd A*, **499** 437, 2003.

[Ada03b] J. Adams et al. *Phys. Rev. Lett*, **91** 072304, 2003.

[Ada04a] J. Adams et al. *Phys. Rev. Lett.*, **92** 182301, 2004.

[Ada04b] J. Adams et al. (STAR Collaboration), *Phys. Rev. Lett.* **93**, 252301 (2004).

[Ada04c] J. Adams et al. *Phys. Rev. Lett.*, **92** 052302, 2004.

[Ada05a] J. Adams et al. (STAR Collaboration), *Nucl. Phys. A*, **757**, 102, 2005.

[Ada05b] J. Adams et al. *Phys. Rev. Lett.*, **95** 122301, 2005.

[Ada05c] J. Adams et al. (STAR Collaboration), *Phys. Rev. C* **72**, 014904 (2005).

[Ada05d] J. Adams et al. *Phys. Lett. B*, **612** 181, 2005.

[Ada06a] A. Adare et al. *nucl-ex/0608033*

[Adc03a] K. Adcox et al. *Nucl. Instru. Methd A*, **499** 469, 2003.

[Adl02a] C. Adler et al. *Phys. Rev. Lett.*, **89** 202301, 2002.

[Adl02b] C. Adler et al. (STAR Collaboration), *Phys. Rev. C* **66**, 034904 (2002).

[Adl03a] C. Adler et al. *Phys. Rev. Lett.*, **90** 082302, 2003.

[Adl04a] S. S. Adler et al. (PHENIX collaboration), *Phys. Rev. C* **69**, 034909 (2004).

[Agg03a] M. M. Aggarwal et al. *Nucl. Instr. Method A*, **499** 751, 2003.

[All03a] C. E. Allgower et al. *Nucl. Instr. Method A*, **499** 740, 2003.

[Alt03a] C. Alt et al. (NA49 Collaboration), *Phys. Rev. C* **68**, 034903 (2003).

[Alv06a] B. Alver et al. (PHOBOS Collaboration), *nucl-ex/0610037*

[Alv08a] B. Alver et al. (PHOBOS Collaboration), *Phys. Rev. C* **77**, 014906 (2008).

[And99a] C. Anderlik et al. *Phys. Rev. C*, **59** 3309, 1999.

[And03a] M. Anderson et al. *Nucl. Instr. Method A*, **499** 659, 2003.

[Arn03a] L. Arnold et al. *Nucl. Instr. Method A*, **499** 652, 2003.

[Bac03a] B. B. Back et al. *Nucl. Instr. Methd A*, **499** 603, 2003.

[Bac05a] B. B. Back et al. *Nucl. Phys. A*, **757** 28, 2005.

[Bac05b] B. B. Back et al. (PHOBOS collaboration), *Phys. Rev. C* **72**, 051901(R) (2005).

[Bac07a] B. B. Back et al. (PHOBOS collaboration), *Phys. Rev. Lett.* **98**, 242302 (2007).

[Bai07a] Y. Bai, *Ph.D. thesis*, 2007

[Bar97a] J. Barrette et al. (E877 Collaboration), *Phys. Rev. C* **56**, 3254 (1997).

[Bar04a] O. Barannikova et al. *nucl-ex/0403014*.

[Bas99a] S. A. Bass, M. Gyulassy, H. Stöcker, W. Greiner. *J. Phys. G*, **25** R1, 1999.

[Bas99b] S. A. Bass et al., *Phys. Rev. C* **60**, 021902 (1999).

[Bas00a] S. A. Bass, A. Dumitru. *Phys. Rev. C*, **61** 064909, 2000.

[Bed03a] M. Beddo et al. *Nucl. Instr. Methd A*, **499** 725, 2003.

[Bei03a] F. S. Beiser et al. *Nucl. Instr. Methd A*, **499** 762, 2003.

[Bel03a] R. Bellwied, et al. *Nucl. Instr. Method A*, **499** 636, 2003.

[Ber03a] F. Bergsma, et al. *Nucl. Instr. Method A*, **499** 629, 2003.

[Bet02a] S. Bethke. *Nucl. Phys. Proc. Suppl.*, **121**:74-81, 2003.

[Bha03a] R. S. Bhalerao, N. Borghini, J.-Y. Ollitrault. *Nucl. Phys. A*, **727** 373, 2003.

[Bha05a] R. Bhalerao et al., *Phys. Lett. B* **627** 49 (2005).

[Bha06a] R. Bhalerao and J-Y. Ollitrault, *Phys. Lett. B* **614**, 260 (2006).

[Bia81a] S. F. Biagi et al., *Nucl. Phys. B* **186**, 1 (1981).

[Ble99a] M. Bleicher et al. *J. Phys. G*, **25** 1859, 1999.

[Ble02a] M. Bleicher, H. Stöcker. *Phys. Lett. B*, **526** 309, 2002.

[Bon03a] B. Bonner et al. *Nucl. Instru. Method A*, **508** 181, 2003.

[Bor01a] N. Borghini, P. M. Dinh, J.-Y. Ollitrault. *Phys. Rev. C*, **63** 054906, 2001.

[Bra95a] P. Braun-Munzinger, J. Stachel, J. Wessels and N. Xu. *Phys. Lett. B*, **344** 43, 1995.

[Bra99a] P. Braun-Munzinger, I. Heppe, J. Stachel. *Phys. Lett. B*, **465** 15, 1995.

[Bra03a] P. Braun-Munzinger, K. Redlich, J. Stachel, in Quark Gluon Plasma 3, eds.

[Bra04a] E. L. Bratkovskaya et al. *Phys. Rev. C*, **69** 054907, 2004.

[Bre69a] M. Breidenbach et al. *Phys. Rev. Lett*, **23** 935, 1969.

[Buc08a] A. Buchel, R. Myers and A. Sinha, *arXiv:0812.2521.*

[Bur04a] G. Burau, J. Bleibel, C. Fuchs, A. Faessler, L. V. Bravina, E. E. Zabrodin. *Phys. Rev. C*, **71** 054905, 2005.

[Che03a] Y. Cheng et al., *Phys. Rev. C* **68**, 034910 (2003).

[Coo74a] F. Cooper and G. Frye. *Phys. Rev. D*, **10** 186, 1974.

[Dre05a] H. J Dresher et al., *Phys. Rev. C* **74**, 044905 (2006).

[Dre07a] H. J Dresher and Y. Nara, *Phys. Rev. C* **76**, 041903 (2007).

[Dre07b] H. J Dresher and Y. Nara, *Phys. Rev. C* **75**, 034905 (2007).

[Dre09a] H. J Dresher and Y. Nara, *Phys. Rev. C* **79**, 064904 (2009).

[Dks03a] G. Dissertori, I. Knowles, and M. Schmelling. *Quantum Chromodynamics - High Energy Experiments and Theory.* Oxford Universidy Press, 2003.

[Don04a] X. Dong et al., *Phys. Lett. B*, **597** 328 (2004).

[Dum99a] A. Dumitru et al. *Phys. Lett. B*, **460** 411, 1999.

[Fri03a] R. J. Fries et al., *Phys. Rev. Lett.* **90**, 202303 (2003).

[Fri04a] R. J. Fries. *J. Phys. G*, **31** S379, 2005.

[Gel64a] M. Gell-Mann. *Phys. Letters*, **8** 214, 1964.

[Gre03a] V. Greco, C. M. Ko, P. Levai. *Phys. Rev. Lett.*, **90** 202302, 2003.

[Hec98a] H. van Hecke, H. Sorge, and N. Xu, *Phys. Rev. Lett.* **81**, 5764 (1998).

[Hir05a] T. Hirano et al., *Phys. Lett. B* **636** (2006) 299.

[Hir05b] T. Hirano. *nucl-th/0510005*

[Hir06a] T. Hirano and M. Gyulassy, *Nucl. Phys. A* **769** (2006) 71.

[Hua88a] K. Huang. *Statistical Mechanics*, John Wiley and Sons, 1988.

[Hun98a] C. M. Hung, E. V. Shuryak. *Phys. Rev. C*, **57** 1891, 1998.

[Huo01a] P. Huovinen, P. F. Kolb, U. Heinz, P. V. Ruuskanen and S. A. Voloshin. *Phys. Lett. B*, **503** 58, 2001.

[Huo03a] P. Huovinen. *private communication*, 2003.

[Huo05a] P. Huovinen. *Nucl. Phys. A*, **761** 296, 2005.

[Huo06a] P. Huovinen and P.V. Ruuskanen, *Ann. Rev. Nucl. Part. Sci.* **56**, 163 (2006).

[Huo06b] P. Huovinen, *private communication*, 2006.

[Huo08a] P. Huovinen, *private communication*, 2008.

[Hwa03a] R. C. Hwa, X. N. Wang. *World Scientific, Singapore*, 2003.

[Hwa03b] R. C. Hwa and C. B. Yang, *Phys. Rev. C* **67**, 064902 (2003).

[Hwa04a] R. C. Hwa and C.B. Yang. *Phys. Rev. C*, **70** 024904, 2004.

[Iss06a] M. Issah and A. Taranenko for the PHENIX Collaboration, *nucl-ex/0604011*

[Kar02a] F. Karsch. *Nucl. Phys. A*, **698** 199, 2002.

[Kol03a] P. F. Kolb and U. Heinz. *nuch-th/0305084*.

[Kov04a] P. Kovtun, D. Son and A. Starinets, *Phys. Rev. Lett.* **94** (2005) 111601.

[Kox76a] A.J. Kox, S.R. de Groot and W. A. van Leeuwen, *Phys. A* **84** 155 (1976).

[Leb02a] A. Lebedev. *Nucl. Instru. Method A*, **478** 163, 2002.

[Lin02a] Z. W. Lin and C. M. Ko. *Phys. Rev. Lett.*, **89** 202302, 2002.

[Mag99a] V. K. Magas et al. *Heavy Ion Phys.*, **9** 193, 1999.

[Mar98a] S. Margetis. *STAR Note 0367*, 1998.

[Mat87a] T. Matsui, *Nucl. Phys. A* **461**, 27 (1987).

[Mat03a] H. S. Matis et al. *Nucl. Instru. Method A*, **499** 802, 2003.

[Mcl01a] L. McLerran, *hep-ph/0104285*

[Mil03a] M. Miller. *PhD thesis*, Yale University, 2003.

[Mil03b] M. Miller and R. Snellings, *nucl-ex/0312008*

[Mil07a] M. Miller et al., *Ann. Rev. Nucl. Part. Sci.* **57**, 205 (2007).

[Mil07b] M. Miller et al. *nucl-ex/0701025*

[Mol03a] D. Molnar and S. A. Voloshin, *Phys. Rev. Lett.* **91**, 092301 (2003).

[Mul72a] R. A. Muller, *Phys. Lett.* **38B**, 123 (1972).

[Non05a] C. Nonaka and S. A. Bass. *nucl-th/0510038*

[Old04a] M. Oldenburg et al. *J. Phys. G*, **31** S437, 2004.

[Old05a] M. Oldenburg et al. *nucl-ex/0510026*

[Oll92a] J.-Y. Ollitrault. *Phys. Rev. D*, **46** 229, 1992.

[Oll93a] J.-Y. Ollitrault. *Phys. Rev. D*, **48** 1132, 1993.

[Oll07a] H. Drescher et al., *Phys. Rev. C* **76** 024905 (2007).

[Pdg08a] Section 5.2.1, Particle Data Group, *Review of Particle Physics* (2008).

[Pos98a] A. M. Poskanzer and S. A. Voloshin, *Phys. Rev. C*, **58** 1671, 1998.

[Pos09a] A. M. Poskanzer, S. A. Voloshin and J-Y. Ollitrault, *Phys. Rev. C* **80**, 014904 (2009).

[Rei04a] W. Reisdorf and H. G. Ritter. *Ann. Rev. Nucl. Part. Sci.*, **47** 663, 1997.

[Rom08a] M. Luzum and P. Romatschke, *Phys. Rev. C* **78**, 034915 (2008).

[Rut11a] E. Rutherford. *Phil. Mag*, **21** 669, 1911

[Rut14a] E. Rutherford. *Phil. Mag*, **27** 488, 1914

[Sat00a] H. Satz. *Rept. Prog. Phys.*, **63** 1511, 2000.

[Sch93a] E. Schnedermann, J. Sollfrank, and U. Heinz. *Phys. Rev. C*, **48** 2462, (1993).

[Sel08a] I. Selyuzhenkov and S. Voloshin, *Phys. Rev. C*, **77**, 034904 (2008).

[Sho85a] A. Shor, *Phys. Rev. Lett.* **54**, 1122 (1985).

[Sne09a] R. Snellings et al., arXiv:0908.0430 (2009).

[Son08a] H. Song and U. Heinz, *Phys. Rev. C* **78**, 024902 (2008)

[Sor95a] H. Sorge. *Phys. Rev. C*, **52** 3291, 1995.

[Sor97a] H. Sorge. *Phys. Lett. B*, **402** 251, 1997.

[Sor97b] H. Sorge. *Phys. Rev. Lett.*, **78** 2309, 1997.

[Sto81a] H. Stöcker, M. Gyulassy, J. Boguta. *Phys. Lett. B*, **103** 269, 1981.

[Sto86a] H. Stöcker and W. Greiner. *Phys. Rept.*, **137** 277, 1986.

[Tea00a] D. Teaney, J. Lauret and E. Shuryak, *Phys. Rev. Lett.* **86** (2001) 4783.

[Tea01a] D. Teaney, J. Lauret and E. Shuryak, *nucl-th/0110037*

[Tea03a] D. Teaney, *Phys. Rev. C* **68** (2003) 034913.

[Tho897] J. J. Thomas. *Phil. Mag.*, **44** 293, 1897.

[Tho02a] J. H. Thomas. *Nucl. Instru. Method A*, **478** 166, 2002.

[Vol96a] S. Voloshin and Y. Zhang. *Z. Phys. C*, **70** 665, 1996.

[Vol98a] A. M. Poskanzer and S. A. Voloshin. *Phys. Rev. C*, **58** 1671, 1998.

[Vol00a] S. A. Voloshin and A. M. Poskanzer, *Phys. Lett. B* **474**, 27 (2000).

[Vol02a] D. Molnar, S. Voloshin. *Phys. Rev. Lett.*, **91** 092301, 2003.

[Vol06a] S. A. Voloshin, *nucl-th/0606022*

[Vol07a] S. A. Voloshin. *arXiv: nucl-ex/0701038*, 2007.

[Vol08a] S. A. Voloshin et al., *Phys. Lett. B* **659**, 537 (2008).

[Wan92a] X. N. Wang, M. Gyulassy. *Phys. Rev. Lett.*, **68** 1480, 1992.

[Wan97a] X. N. Wang, *Phys. Rep.* **280**, 287 (1997).

[Wan98a] X. N. Wang. *Phys. Rev. C*, **58** 2321, 1998.

[Wan05a] X. N. Wang. *Nucl. Phys. A*, **750** 98, 2005.

[Wil74] K. G. Wilson. *Phys. Rev. D*, **10** 2455, 1974.

[Wie06a] H. Wieman et al. *Technical Report*, 2006.

[Xu02a] N. Xu, M. Kaneta. *Nucl. Phys. A*, **698** 306c, 2002.

[Xu04a] N. Xu. *Prog. Part. Nucl. Phys.*, **53** 165, 2004.

[Zwe64a] G. Zweig. *CERN preprints Th.*, 401 and 412, 1964.

Presentations and publication List

Presentations

1. A Monte Carlo Study on the Expansion of Hadronic Gas in Relativistic Heavy Ion Collisions (oral)

   The Seventh Meeting of the High energy Physics Divisions of the Chinese Physical Society, Guilin, China, 2006.

2. Partonic collectivity at RHIC (oral)

   Third Joint Meeting of the Nuclear Physics Divisions of the American Physical Society and The Physical Society of Japan, Hawaii, USA, 2009.

3. Can we measure the viscosity from the system size dependence of v_2 (oral)

   Joint CATHIE/TECHQM Workshop, Brookhaven National Laboratory, USA, 2009.

4. Flow results from STAR at RHIC

   Heavy Ion Tea seminar, Lawrence Berkeley National Laboratory, USA, 2010.

Proceedings

1. K_S^0 and Λ elliptic flow from 200 GeV Cu+Cu collisions, Shusu Shi for the STAR collaboration,

   20th International Conference on Ultra-Relativistic Nucleus Nucleus Collisions (Quark Matter 2008).

2. Strange hadron elliptic flow from 200 GeV Cu+Cu collisions, Shusu Shi for the STAR collaboration,

   Proc. 24th winter workshop on nuclear dynamics, 2008.

3. Event anisotropy v_2 at STAR, Shusu Shi for the STAR collaboration,

   21th International Conference on Ultra-Relativistic Nucleus Nucleus Collisions (Quark Matter 2009).

Publication list

1. A Monte-Carlo study on the multiplicity dependence of event- by- event transverse momentum fluctuation in relativistic heavy ion collision,

   Shusu Shi, and Jiaxin Du, *Huazhong Normal University Journal of Postgraduates* **13**, 144-146 (2006).

2. A Monte Carlo study on the expansion of hadronic gas in relativistic heavy-ion collisions,

   Shusu Shi, and Lianshou Liu, *High Energy Physics and Nuclear Physics* **31**, 56-58 (2007).

3. The inversion-asymmetry of particle emission source in relativistic heavy-ion collisions,

   Shusu Shi, Jiaxin Du and Lianshou Liu, *Eur. Phys. J. A* **33**, 53-56 (2007).

4. Strange hadron elliptic flow from 200 GeV Cu + Cu collisions,

   Shusu Shi, EP Systema, Budapest, ISBN **978 963 86934 3 3**, 43-48, 2008.

5. Event anisotropy v_2 at STAR,

   Shusu Shi, *Nucl. Phys. A* **830**, 187-190 (2009).

STAR Publications as principal author:

6. Identified particle production, azimuthal anisotropy, and interferometry measurements in Au+Au collisions at $\sqrt{s_{NN}} = 9.2$ GeV,

   B.I. Abelev, et al., STAR collaboration, *Phys. Rev. C* **81**, 024911 (2010).

7. Charged and strange hadron elliptic flow in Cu+Cu collisions at $\sqrt{s_{NN}} = 62.4$ and 200 GeV,

   B.I. Abelev, et al., STAR collaboration, *Phys. Rev. C* **81**, 044902 (2010).

8. Anisotropic flow at RHIC and the deviation from the ideal hydrodynamic limit,

   B.I. Abelev, et al., STAR collaboration, STAR internal review, target journal: *Phys. Rev. Lett.*

9. Breaking of number of constituent quark scaling at high transverse momentum for Au+Au Collisions at $\sqrt{s_{NN}} = 200$ GeV,

   B.I. Abelev, et al., STAR collaboration, STAR internal review, target journal: *Phys. Rev. C.*

10. Measurement of elliptic ow for multistrange hadrons in Au+Au collisions at $\sqrt{s_{NN}}$ = 200 GeV,

    B.I. Abelev, et al., STAR collaboration, STAR internal review, target journal: *Phys. Rev. Lett.*

STAR Publications:

11. Hadronic resonance production in d+Au collisions at $\sqrt{s_{NN}}$ =200 GeV measured at the BNL Relativistic Heavy Ion Collider,

    B.I. Abelev, et al., STAR collaboration, *Phys. Rev. C* **78**, 044906 (2008).

12. Spin alignment measurements of the $K^{*0}(892)$ and $\phi(1020)$ vector mesons in heavy ion collisions at $\sqrt{s_{NN}} = 200$ GeV,

    B.I. Abelev, et al., STAR collaboration. *Phys. Rev. C* **77**, 061902 (2008).

13. Centrality dependence of charged hadron and strange hadron elliptic flow from $\sqrt{s_{NN}} = 200$ GeV Au+Au collisions,

    B.I. Abelev, et al., STAR collaboration. *Phys. Rev. C* **77**, 054901 (2008).

14. Indications of Conical Emission of Charged Hadrons at the BNL Relativistic Heavy Ion Collider,

B.I. Abelev, et al., STAR collaboration, *Phys. Rev. Lett.* **102**, 052302 (2009).

15. Charge Independent(CI) and Charge Dependent(CD) correlations vs. Centrality from $\Delta\phi\Delta\eta$ Charged Pairs in Minimum Bias Au+Au Collisions at $\sqrt{s_{NN}} = 200$ GeV,

    B.I. Abelev, et al., STAR collaboration, arXiv:0806.0513. Submitted to *Phys. Rev. C*.

16. System-Size Independence of Directed Flow Measured at the BNL Relativistic Heavy-Ion Collider,

    B.I. Abelev, et al., STAR collaboration, *Phys. Rev. Lett.* **101**, 252301 (2008)

17. Beam-energy and system-size dependence of dynamical net charge fluctuations,

    B.I. Abelev, et al., STAR collaboration, *Phys. Rev. C* **79**, 024906 (2009)

18. Systematic measurements of identified particle spectra in pp, d+Au, and Au+Au collisions at the STAR detector,

    B.I. Abelev, et al., STAR collaboration, *Phys. Rev. C* **79**, 034909 (2009)

19. Measurements of ϕ meson production in relativistic heavy-ion collisions at the BNL Relativistic Heavy Ion Collider (RHIC),

    B.I. Abelev, et al., STAR collaboration， *Phys. Rev. C* **79**, 064903 (2009)

20. Energy and system size dependence of ϕ meson production in Cu+Cu and Au+Au collisions,

    B.I. Abelev, et al., STAR collaboration, *Phys. Lett. B.* **673**, 183 (2009)

21. Observation of Two-Source Interference in the Photoproduction Reaction AuAu $\rightarrow$ AuAuρ^0,

    B.I. Abelev, et al., STAR collaboration, *Phys. Rev. Lett.* **102**, 112301 (2009)

22. Measurement of D^* mesons in jets from p+p collisions at $\sqrt{s_{NN}}$ =200 GeV,

    B.I. Abelev, et al., STAR collaboration, *Phys. Rev. D* **79**, 112006 (2009)

23. K/π Fluctuations at Relativistic Energies,

    B.I. Abelev, et al., STAR collaboration, *Phys. Rev. Lett.* **103**, 092301 (2009)

24. Pion interferometry in Au+Au and Cu+Cu collisions at $\sqrt{s_{NN}} = 62.4$ and 200 GeV,

    B.I. Abelev, et al., STAR collaboration, *Phys. Rev. C* **80**, 024905 (2009)

25. J/Ψ production at high transverse momentum in p+p and Cu+Cu collisions at $\sqrt{s_{NN}} = 200$ GeV,

    B.I. Abelev, et al., STAR collaboration, *Phys. Rev. C* **80**, 041902(R) (2009)

26. System size dependence of associated yields in hadron-triggered jets,

    B.I. Abelev, et al., STAR collaboration, *Phys. Lett. B* **683** (2010) 123

27. Growth of Long Range Forward-Backward Multiplicity Correlations with Centrality in Au+Au Collisions at $\sqrt{s_{NN}} = 200$ GeV,

    B.I. Abelev, et al., STAR collaboration, *Phys. Rev. Lett.* **103**, 172301 (2009)

28. Center of mass energy and system-size dependence of photon production at forward rapidity at RHIC,

    B.I. Abelev, et al., STAR collaboration, *Nucl. Phys. A* **832** (2009) 134

29. Neutral pion production in Au+Au collisions at $\sqrt{s_{NN}} = 200$ GeV,

    B.I. Abelev, et al., STAR collaboration, *Phys. Rev. C* **80**, (2009) 044905

30. Long range rapidity correlations and jet production in high energy nuclear collisions,

    B.I. Abelev, et al., STAR collaboration, *Phys. Rev. C* **80** (2009) 064912

31. Yields and elliptic flow of $d(\overline{d})$ and $^3He(\overline{^3He})$ in Au+Au collisions at $\sqrt{s_{NN}} = 200$ GeV,

    B.I. Abelev, et al., STAR collaboration, arXiv:0909.0566v1, submitted to *Phys. Lett. B*

32. Azimuthal Charged-Particle Correlations and Possible Local Strong Parity Violation,

    B.I. Abelev, et al., STAR collaboration, *Phys. Rev. Lett.* **103** (2009) 251601

33. Observation of charge-dependent azimuthal correlations and possible local strong parity violation in heavy ion collisions,

    B.I. Abelev, et al., STAR collaboration, arXiv:0909.1717v1, submitted to *Phys. Rev. C.*

34. Longitudinal Spin Transfer to Lambda and Anti-Lambda Hyperons in Polarized Proton-Proton Collisions at $\sqrt{s_{NN}} = 200$ GeV,

    B.I. Abelev, et al., STAR collaboration, *Phys. Rev. D* **80** (2009) 111102

35. Observation of an Antimatter Hypernucleus,

    B.I. Abelev, et al., STAR collaboration, arXiv:1003.2030v1, accepted by *Science.*

36. Longitudinal double-spin asymmetry and cross section for inclusive neutral pion production at midrapidity in polarized proton collisions at $\sqrt{s_{NN}} = 200$ GeV,

    B.I. Abelev, et al., STAR collaboration, *Phys. Rev. D* **80** (2009) 111108

37. Identified high p_T spectra in Cu+Cu collisions at $\sqrt{s_{NN}} = 200$ GeV,

    B.I. Abelev, et al., STAR collaboration, arXiv:0911.3130v1, submitted to *Phys. Rev. C.*

38. Observation of $\pi^+\pi^-\pi^+\pi^-$ Photoproduction in Ultra Peripheral Heavy Ion Collisions at STAR,

    B.I. Abelev, et al., STAR collaboration, arXiv: 0912.0604v1, submitted to *Phys. Rev. C.*

39. Studying Parton Energy Loss in Heavy-Ion Collisions via Direct Photon and Charged-Particle Azimuthal Correlations,

    B.I. Abelev, et al., STAR collaboration, arXiv: 0912.1871v1, submitted to *Phys. Rev. Lett.*

40. Inclusive π^0, η, and direct photon production in p+p and d+Au collisions at $\sqrt{s_{NN}}$ = 200 GeV,

    B.I. Abelev, et al., STAR collaboration, arXiv: 0912.3838v1, submitted to *Phys. Rev. C.*

41. Upsilon cross section in p+p collisions at $\sqrt{s_{NN}} = 200$ GeV,

    B.I. Abelev, et al., STAR collaboration, arXiv: 1001.2745v1, submitted to *Phys. Rev. C.*

42. Three-particle coincidence of the long range pseudorapidity correlation in high energy nucleus-nucleus collisions,

    B.I. Abelev, et al., STAR collaboration, arXiv:0912.3977v2, submitted to *Phys. Rev. Lett.*

43. Longitudinal scaling property of the charge balance function in Au+Au collisions at $\sqrt{s_{NN}} = 200$ GeV,

    B.I. Abelev, et al., STAR collaboration, arXiv:1002.1641v1, submitted to *Phys. Lett. B.*

Acknowledgements

Many thanks to all people who help me to complete this thesis!

I would like to thank Prof. Lianshou Liu for introducing me into high energy physics in 2005 and constant supporting me over the following years. Without his help and encouragement I can not make this step. Prof. Liu passed away in December last year, but he will always live in my heart.

I would like to thank my supervisor Prof. Feng Liu and Prof. Nu Xu. With Feng's guide and support, I got the great opportunity to take part in the data analysis. Nu provided me a chance to do data analysis on the most exciting experiment facility in the world and chose this nice topic for me. He is always so kind and patient in guiding me, both on the work and life. I thank Nu for his guidance and fruitful discussions on many aspects of my research in the last three years. I greatly benefited from his profound and broad understanding of physics.

I would like to thank Art Poskanzer, Paul Sorensen, Aihong Tang and Sergei Voloshin for valuable assistance in flow analysis.

Thanks to Dr. Xin Dong and Dr. Lijuan Ruan, they gave me lots of help on the work and life when I stayed at USA. Thanks to Dr. Yan Lu and Dr. Hiroshi Masui for the valuable discussions and helps on the topic of this thesis.

Thanks to everyone of the LBNL-RNC group for the help and happiness they bring me. Thanks to every member of the STAR collaboration and the RHIC operation group.

Thanks to Dr. Jinhui Chen, Fu Jin, Na Li, Xuan Li, Xiaofeng Luo, Hao Qiu, Dr. Xinghua Shi, Dr. Xiangming Sun, Dr. Zebo Tang, Dr. Yichun Xu, Xiaoping Zhang, Dr. Yifei Zhang and Yi Zhou for many helpful discussions and joyful time we had together at BNL.

Thank all the professors, staffs and classmates in IOPP.

I would like to thank Prof. Hongfang Chen, Prof. Shan Jin, Prof. Feng Liu, Prof. Yugang Ma, Dr. Aihong Tang and Prof. Nu Xu for acting as the members of my dissertation committee.

Finally, I would like to thank my family. Without their sacrifice and support, I won't be here.